Geophysics-based soil mapping for improved modelling of spatial variability in crop growth and yield

Von der Fakultät Bau- und Umweltingenieurwissenschaften der
Universität Stuttgart zur Erlangung der Würde eines
Doktor-Ingenieurs (Dr.-Ing.) genehmigte Abhandlung

Vorgelegt von

Cosimo Brogi

aus Montevarchi

Hauptberichter:	Prof. Dr. Johan Alexander Huisman
Mitberichter:	Prof. Dr. Sarah Garré
Mitberichter:	Prof. Dr. Naftali Lazarovitch

Tag der mündlichen Prüfung: 08.11.2019

Institut für Wasser- und Umweltsystemmodellierung (IWS)
der Universität Stuttgart

2019

Eigenständigkeitserklärung

Hiermit erkläre ich, dass diese Arbeit nur meine Originalarbeit umfasst und dass ich die vorliegende Dissertation " Geophysics-based soil mapping for improved modelling of spatial variability in crop growth and yield" unabhängig geschrieben habe. Alle anderen verwendeten Quellen und Materialien wurden im Text entsprechend anerkannt.

Declaration of independent work

I hereby declare that this thesis comprises only my original work and that I have independently written the present dissertation “Geophysics-based soil mapping for improved modelling of spatial variability in crop growth and yield”. Due acknowledgement has been made in the text to all the other works and materials that were used.

Stuttgart

_____

Cosimo Brogi

Acknowledgements

This research presented in this thesis was supported by the Deutsche Forschungsgemeinschaft through the Transregional Collaborative Research Center TR32 – Patterns in Soil-Vegetation-Atmosphere Systems: Monitoring, Modeling and Data Assimilation. In addition, support was received through the "Terrestrial ENvironmental Observatories" (TERENO), and "Advanced Remote Sensing—Ground-Truth Demo and Test Facilities" (ACROSS) initiatives of the Helmholtz association.

Firstly, I would like to thank my supervisor Prof. Dr. Johan Alexander Huisman for his continuous guidance, patience, and knowledge in the subject matter over the past years and for an active supervision while leaving a certain degree of autonomy where appropriate. In these years, I understood that certain characteristics of the supervisor will be passed on their PhD students. For this reason, I am grateful that I have had the chance to closely work with Prof. Dr. Huisman. Secondly, I would like to thank Dr. Lutz Weihermüller and Dr. Michael Herbst for their essential feedback on my work and their needed help in different phases of my PhD. It was a pleasure working in such a stimulating environment with extremely knowledgeable people.

I also want to thank Dr. Stefan Pätzold, Prof. Dr. Jan van der Kruk, Dr. Christian von Hebel, Dr. Carsten Montzka, and Dr. Anne Klosterhalfen for their precious help in various phases of this work. Another mention goes to my colleagues and flat-mates Igor dal Bo and Manuela Kaufmann for the open discussions, suggestions, and constructive criticism that we exchanged on a day-to-day basis in the past years. I also want to thank the members of my doctoral committee for having spent their time in evaluating my work. My sincere thanks also go to Prof. Ty Ferré for the open discussions in early 2016 that sparked the development of the methodology of my first paper.

I also thank Marius Schmidt for his valuable help with managing the contacts with the land owners. I also want to thank: i) Elizabeth Verweij, Zhen Zhou, Dr. Tao Liu, Philipp Pohlig, Maximillian Kanig, Luka Kurnjek, Xihe Tan, and Dr. Hui Wang for their help in the geophysical campaign, ii) Michael Lesch, Prakash Satenahalli, Liza de Quadros, and Dr. Magdalena Landl for their support during the analysis of the soil samples, iii) Tim Reichenau for providing in situ LAI measurements, and iv) Prof. Francois Jonard for the drone images.

I also want to thank my colleagues and friends of the IBG-3 Agrosphere institute and of the TR32 project as they enriched my working and out-of-work life in many ways. I also want to thank Prof. Dr. Harry Vereecken and Prof. Dr. Jan Vanderborght for maintaining such a highly professional environment and for their support in this work. Within the IBG-3 institute, I also want to thank: i) Rainer Harms for managing the institute vehicles in a remarkably professional way and for always making a pen available in the car document bags, ii) Gaby Pillert and Sandy Schnober for their patience with the bureaucratic aspects of the life of a PhD student, iii) Thomas Schuster for ensuring the life-time of my hardware during my PhD, iv) Horst Hardelauf for his patience with my repetitive problems in using the terminal server, v) Dr. Anja Klotzsche for the marvelous time in the swamps of Cuxhaven, vi) Miriam Zörner for her invaluable help with the language barrier on many occasions, and, in general, all the other members of the institute.

I want to thank all the past and present PhD students of the IBG-3. Among them, I want to mention my office mates Yu Yi and Mai Trung Wei, and Amirpasha Mozaffari, Dr. Michael Stockinger, Dr. Roland and Dorina Baatz, Shirin Moradi, Inge Wiekenkamp, Emil Shahnazaryan, Jessica Schmäck, Maria Quade, Patrizia Ney, Sean McGovern, Daniela Castro Herrera, Helena Jordà Guerra, Anneli Karlsson, and Jannis Jakobi for the time spent working or having fun together. I thank Prof. Dr. Piero Lorenzo Fantozzi from the University of Siena for many reasons, too many for this list, Prof. Dr. Pierluigi Pieruccini, Dr. Filippo Bonciani, Prof. Dr. Paolo Conti, and my old colleagues of the JRC in Ispra for having spurred me to pursue a doctoral degree, Prof. Roberto Sacchini because he was very patient with a lazy middle school student, and Prof. Dr. Marco Meccheri.

Last but not least, I want to thank my friends and family in Italy, the new member of my family, Petre za jej cennú pomoc a pretože bez nej by som to tak ďaleko nedotiahol, e infine la mi' Mamma e il mi' Babbo.

Abstract

Water shortage is one of the predominant factors that can directly or indirectly cause a reduction in crop yield and thus poses a severe threat to sustainable crop production. It is therefore critical to improve the sustainability of current agricultural management practices and develop new strategies that will allow the establishment of more sustainable agricultural production systems that can meet present and future food demand. The use of agro-ecosystem models to simulate crop growth for given environmental conditions, and the use of detailed information on soil heterogeneity beyond the field scale are among the most promising tools for achieving this goal. Soil properties are a key control for water and nutrient availability and are therefore co-responsible for yield gaps and harvest failures. A detailed representation of the spatial variability of soil is consequently essential for establishing relevant spatially distributed agro-ecosystem simulations of crop performance in response to water stress. Unfortunately, a detailed soil representation is costly to obtain, and generally cannot be substituted by the use of existing general-purpose soil maps that lack the necessary level of detail. Recently, improvements in digital soil mapping have been made using non-invasive geophysical methods such as electromagnetic induction (EMI) that provide fast and cost-effective mapping of relevant soil information. It is however still challenging to derive information relevant for agricultural management from large geophysical datasets and their added value for agricultural applications has not been fully investigated yet, especially for the analysis of patterns in crop performance. This thesis aims at investigating and quantifying the added value of detailed soil information obtained using large-scale geophysical mapping for the simulation and prediction of the spatial variability of crop growth and yield obtained with agro-ecosystem modelling.

In a first step, a detailed EMI survey with a 2.5 m spacing between measurement lines was performed for a 1 x 1 km area consisting of 51 adjacent agricultural fields where previous studies reported a clear connection between soil properties and crop performance. In total, nine apparent electrical conductivity (ECa) maps were obtained with a depth of investigation ranging between 0 to 2.7 m. Based on the combination of these ECa maps and available soil maps, an a priori interpretation was performed and four sub-areas with characteristic sediments and ECa were identified. This was followed by a division of the ECa maps into areas with similar soil properties using a supervised classification methodology. Soil profile descriptions up to a depth of 2 m were obtained at 100 sampling locations and 552 samples

were analyzed for textural characteristics. The combination of the classified map and ground truth data resulted in a 1m resolution geophysics-based soil map divided into eighteen soil units with soil profile and texture information. These eighteen soil units showed statistically significant differences when their characteristics were compared using a two-tailed t-test and corresponded well with patterns in crop performance obtained from satellite imagery.

In a second step, this geophysics-based soil map was used as input for agro-ecosystem simulations of the growth of multiple crops. Soil hydraulic parameters were calculated from texture and bulk density by using the pedotransfer function (PTF) from Rawls and Brakensiek (1985). Simulations of soil water content dynamics performed with the agro-ecosystem model AgroC were compared with soil water content measured at two different locations. The resulting root mean square error (RMSE) between measured and simulated water content was 0.032 and 0.056 cm^3 cm^{-3} for the two sites. These RMSE values were lower than that of these obtained using the more widely used ROSETTTA PTF. The AgroC model was then used to simulate the growth of corn, potato, sugar beet, winter rapeseed, winter barley, and winter wheat in the 1 x 1 km study area. It was found that the simulated leaf area index (LAI) was affected by the magnitude of simulated water stress, which was a function of both the crop type and soil characteristics. Simulations of LAI were generally consistent with the observed LAI_{NDVI} obtained from RapidEye satellite images. Finally, maps of simulated productivity at harvest were produced for corn, sugar beet, winter barley, and winter wheat and the results matched well with actual harvest data and literature values.

In a third step, the agro-ecosystem simulations obtained using the geophysics-based soil map were compared with simulations obtained using two general-purpose soil maps. In these two maps, quantitative percentages of the grain size distribution were calculated by using the USDA soil texture triangle since these two maps were provided with a qualitative subdivision in textural classes only. The soil texture of the upper horizons was found to be rather similar in the three soil maps, which was not the case for the description of the underlying coarse horizons and the location of the boundaries between the four sub-areas in which the study area was divided. Subsequently, the growth of corn, sugar beet, winter barley, winter rapeseed, and winter wheat was simulated with AgroC using inputs from all three maps. A comparison between simulated LAI and observed LAI_{NDVI} consistently showed that lower RMSE and higher model efficiency (ME) and coefficient of determination (R^2) were obtained using the geophysics-based soil map. The added value of the geophysics-based soil map was rather

subtle for winter crops and for periods with limited water stress. On the contrary, the geophysics-based soil map resulted in improved LAI predictions for summer crops and for periods with a strong reduction in crop performance. A more detailed comparison of the simulation results for sugar beet showed that the geophysics-based soil map provided better results due to more accurate descriptions of i) the depth to coarse sediments, ii) the soil texture of the soil above the coarse sediments, and iii) the subdivision of the four sub-areas. Furthermore, the simulated productivity of sugar beet at harvest matched with the actual harvest only with the use of inputs from the geophysics-based soil map.

In conclusion, the novel EMI data processing approach described in this thesis provided a reliable and cost-effective tool to obtain high-resolution soil maps that are beneficial for precision agriculture. The geophysics-based soil map obtained through this approach allowed accurate agro-ecosystem simulations for multiple crops in a large area where water stress is strongly influenced by soil characteristics. Overall, it was found that a geophysics-based soil map represents an added value in terms of providing long-term support to agricultural management as it is able to provide crucial information on the spatial distribution of water stress and crop performance under present and future scenarios. The presented methodology might provide the foundation for future research aimed at obtaining detailed soil information in agricultural areas well beyond the scale that was investigated in this thesis and at improving management practices such as the optimization of irrigation and crop rotation for given climatic conditions.

Zusammenfassung

Wasserknappheit ist einer der dominierenden Faktoren, der direkt oder indirekt zu einer Verringerung des Ernteertrags führen kann und somit eine ernsthafte Bedrohung für eine nachhaltige Pflanzenproduktion darstellt. Daher ist es von entscheidender Bedeutung, die derzeitigen landwirtschaftlichen Bewirtschaftungspraktiken zu verbessern und neue Strategien zu entwickeln, die es ermöglichen, nachhaltigere landwirtschaftliche Produktionssysteme zu etablieren, die die gegenwärtige und zukünftige Nachfrage nach Lebensmitteln decken können. Der Einsatz von Agrar-Ökosystemmodellen zur Simulation des Pflanzenwachstums unter gegebenen Umweltbedingungen und die Verwendung detaillierter Informationen zur Bodenheterogenität über die Feldskala hinaus gehören zu den vielversprechendsten Instrumenten zur Erreichung dieses Ziels. Die Bodeneigenschaften bestimmen die Wasser- und Nährstoffverfügbarkeit und sind somit mitverantwortlich für Ertragslücken und Ernteausfälle. Eine detaillierte Darstellung der räumlichen Variabilität des Bodens ist daher unerlässlich, um relevante räumlich verteilte Agrar-Ökosystemsimulationen der Ertragsleistung als Reaktion auf Wasserstress zu erstellen. Leider ist eine detaillierte Charakterisierung der Bodeneigenschaften kostspielig und zeitintensiv und kann in der Regel nicht durch die Verwendung vorhandener universeller (grobskaliger) Bodenkarten ersetzt werden. In jüngster Zeit wurden Verbesserungen bei der digitalen Bodenkartierung vorgenommen, wobei nicht-invasive geophysikalische Methoden wie elektromagnetische Induktion (EMI) genutzt werden, um eine schnelle und kostengünstige Kartierung relevanter Bodeninformationen zu ermöglichen. Jedoch ist es nach wie vor schwierig aus großen geophysikalischen Datensätzen relevante Informationen für die landwirtschaftliche Praxis abzuleiten. Auch ist dessen Mehrwert für landwirtschaftliche Anwendungen noch nicht vollständig untersucht, insbesondere für die Analyse von Mustern in der Ertragsleistung. Diese Studie zielt daher auf die Untersuchung und Quantifizierung des Mehrwerts detaillierter Bodeninformationen ab, die mit Hilfe groß angelegter geophysikalischer Kartierungen für die Simulation und Vorhersage der räumlichen Variabilität von Pflanzenwachstum und Ertrag durch Agrar-Ökosystemsimulationen gewonnen wurden.

In einem ersten Schritt wurde eine detaillierte EMI-Kartierung mit einem Abstand von 2,5 m zwischen den Messlinien für ein 1 x 1 km großes Gebiet mit insgesamt 51 landwirtschaftlichen Schlägen durchgeführt, wobei frühere Studien einen deutlichen

Zusammenhang zwischen Bodeneigenschaften und Ertragsleistung zeigten. Insgesamt wurden neun Karten der scheinbaren elektrischen Leitfähigkeit (ECa) mit einer Erkundungstiefe zwischen 0 und 2,7 m erstellt. Basierend auf der Kombination dieser ECa-Karten und verfügbaren Bodenkarten wurde eine a- priori Interpretation durchgeführt und vier Teilflächen mit charakteristischen Böden und charakteristischer ECa identifiziert. Es folgte eine weitere Aufteilung der ECa-Karten in Gebiete mit ähnlichen Bodeneigenschaften unter Verwendung einer überwachten Klassifikation. An 100 Probenahmestellen wurden Bodenprofilbeschreibungen bis zu einer Tiefe von maximal 2 m aufgenommen und 552 Proben wurde hinsichtlich der Bodentextur analysiert. Die Kombination der Bodenklassifikation und der Bodenbeprobung führte zu einer geophysikalisch basierten Bodenkarte mit einer Auflösung von 1 m, die in achtzehn Bodeneinheiten mit Bodenprofil- und Texturinformationen unterteilt ist. Diese achtzehn Bodeneinheiten zeigten statistisch signifikante Unterschiede (zweiseitiger t-Test) und korrelierten gut mit Pflanzenmustern aus Satellitenbildaufnahmen.

In einem zweiten Schritt wurde diese geophysikalisch basierte Bodenkarte als Input für Agrar-Ökosystemsimulationen für 6 landwirtschaftliche Kulturen verwendet. Die hydraulischen Bodenparameter wurden aus Textur und Lagerungsdichte mit Hilfe der Pedotransferfunktion (PTF) von Rawls und Brakensiek (1985) berechnet. Simulationen der Dynamik des Bodenwassergehalts, die mit dem Agrar-Ökosystemmodell AgroC durchgeführt wurden, wurden mit dem an zwei verschiedenen Orten gemessenen Bodenwassergehalt verglichen. Der resultierende mittlere Quadratwurzelfehler (RMSE) zwischen gemessenem und simuliertem Wassergehalt betrug 0,032 und 0,056 cm^3 cm^{-3} für die beiden Standorte. Diese RMSE-Werte waren niedriger als die, die mit den etablierten ROSETTTA PTFs erzielt wurden. Mit dem AgroC-Modell wurde in einem weiteren Schritt das Wachstum von Mais, Kartoffeln, Zuckerrüben, Winterraps, Wintergerste und Winterweizen im 1 x 1 km großen Untersuchungsgebiet simuliert. Es wurde festgestellt, dass der simulierte Blattflächenindex (LAI) vom simulierten Wasserstresses beeinflusst wurde, der sowohl von der Kulturart als auch von den Bodeneigenschaften abhängt. Die Simulationen des Blattflächenindex (LAI) waren im Allgemeinen konsistent mit den beobachteten LAI_{NDVI}, die aus RapidEye-Satellitendaten abgeleitet wurden. Schließlich wurden Karten der simulierten Ernteproduktivität für Mais, Zuckerrüben, Wintergerste und Winterweizen erstellt, deren Ergebnisse gut mit gemessenen Erträgen und Literaturwerten übereinstimmen.

In einem dritten Schritt wurden die mit der geophysikalisch basierten Bodenkarte erstellten Agrar-Ökosystemsimulationen mit Simulationen auf Basis von zwei universellen Bodenkarten verglichen. In diesen beiden Karten wurden die Anteile der Korngrößenverteilung unter Verwendung des USDA-Bodentexturdreiecks abgeleitet, da diese beiden Karten nur Informationen zu Texturklassen bereit stellen. Die Bodentextur der oberen Horizonte erwies sich in den drei Bodenkarten als recht ähnlich, was aber für die Unterbodenhorizonte und die Lage der Horizontgrenzen zwischen den vier Teilbereichen, in die das Untersuchungsgebiet unterteilt war, nicht der Fall war. Anschließend wurde das Wachstum von Mais, Zuckerrüben, Wintergerste, Winterraps und Winterweizen mit AgroC anhand von Inputs aus allen drei Karten simuliert. Ein Vergleich zwischen simuliertem LAI und beobachtetem LAI_{NDVI} zeigte, dass ein niedrigerer RMSE und ein höhere Modelleffizienz (ME) sowie ein höheres Bestimmtheitsmaß (R^2) unter Verwendung der geophysikalischen Bodenkarte erreicht wurden. Der Mehrwert der geophysikalisch basierten Bodenkarte war für Winterkulturen und für Zeiträume mit begrenztem Wasserstress eher niedrig. Die geophysikalisch basierte Bodenkarte führte aber zu verbesserten LAI-Vorhersagen für Sommerkulturen und für Perioden mit stark verminderter Ernteleistung. Ein detaillierterer Vergleich der Simulationsergebnisse für Zuckerrüben zeigte, dass die geophysikalisch basierte Bodenkarte aufgrund genauerer Beschreibungen von i) der Tiefe bis zu Schottersedimenten, ii) der Bodentextur des Bodens über den Schottersedimenten und iii) der Unterteilung der vier Teilbereiche bessere Ergebnisse lieferte. Darüber hinaus stimmen die simulierten Erträge der Zuckerrübe mit den tatsächlichen Erträgen nur bei der Verwendung der geophysikalisch basierten Bodenkarte überein.

Zusammenfassend lässt sich feststellen, dass der in dieser Arbeit beschriebene neuartige EMI-basierte Kartierungsansatz ein zuverlässiges und kostengünstiges Werkzeug zur Gewinnung hochauflösender Bodenkarten ist, der für die Präzisionslandwirtschaft von Vorteil sein wird. Die so gewonnene geophysikalisch basierte Karte ermöglichte genaue Agrar-Ökosystemsimulationen für mehrere Nutzpflanzen in einem großen Gebiet, in dem der Wasserstress stark von den Bodeneigenschaften beeinflusst wird. Es wurde festgestellt, dass eine geophysikalisch basierte Bodenkarte einen Mehrwert für die langfristige Unterstützung der landwirtschaftlichen Bewirtschaftung darstellt, da sie in der Lage ist, entscheidende Informationen über das räumliche Muster von Wasserstress und Ertrag unter aktuellen und zukünftigen Szenarien zu liefern. Die vorgestellte Methodik könnte die Grundlage für zukünftige Forschungsarbeiten bilden, die darauf abzielen, detaillierte Bodeninformationen in

landwirtschaftlichen Gebieten zu erhalten, die weit über das in dieser Studie bereits untersuchte Maß hinausgehen, und die in der Lage sind Managementpraktiken, wie z.B. die Optimierung der Bewässerung und der Fruchtfolge für bestimmte klimatische Bedingungen, besser anzupassen.

Contents

List of figures

List of tables

Tables in supplementary material

List of abbreviations

ATV	All-terrain vehicle
BD	Bulk density
CEC	Cation exchange capacity
DEM	Digital elevation model
DGPS	Differential global positioning system
DOI	Depth of investigation
ECa	Apparent electrical conductivity
EMI	Electromagnetic induction
ERT	Electrical resistivity tomography
FVC	Fractional vegetation cover
GIS	Geographic information system
GPR	ground penetrating radar
GPS	Global positioning system
HCP	Horizontal coplanar
LAI	Leaf area index
ME	Model efficiency
NDVI	Normalized difference vegetation index
NEE	Net ecosystem exchange
PTF	Pedotransfer Function
RGB	Red, green, blue
RMSE	Root mean square error
R2	Coefficient of determination
TNR	True negative ratio
TPR	True positive ratio
VCP	Vertical coplanar

Chapter 1

Introduction

In recent years, significant improvements have been made in data acquisition, data management, and modelling to support more productive and sustainable agriculture, which is vital to meet present food security challenges (Antle et al., 2017). Reductions in crop performance can be directly or indirectly attributed to a number of factors, such as insufficient nutrient availability, inadequate crop and soil management practices, adverse weather conditions, occurrence of pests and diseases, and water shortage (Baret et al., 2007; Foley et al., 2011; Sánchez, 2010; Slingo et al., 2005). Worldwide, agriculture is the largest consumer of freshwater (Brauman et al., 2013) with most crops being produced using water that comes exclusively from precipitation (Rosegrant et al., 2009). Water is not only essential in agriculture, but also is a vital component of the environment significantly impacting ecosystem and human health, nature conservation, sustainable development, industry, and economic growth (Chartzoulakis and Bertaki, 2015). At the same time, the rapidly growing world population combined with increasing irrigation practices, industrial developments, and climate change have been affecting the quantity and quality of the available water (Chartzoulakis and Bertaki, 2015). Within this context, drought stress caused by below-average precipitation is considered to be a severe threat for sustainable crop production in the coming decades (Anjum et al., 2011). It will therefore be essential to produce more food per unit of water (Brauman et al., 2013).

A crop can reach its yield potential when grown with adequate water and nutrient supply in the absence of additional stress factors, such as pests, diseases, and weeds (Evans and Fischer, 1999). The yield potential is the highest yield that a given crop can reach in a given area, and it depends on crop density, solar radiation, temperature, and atmospheric CO_2 concentration (Evans, 1996; van Ittersum et al., 2003). However, a crop rarely achieves its yield potential

(van Ittersum et al., 2013). Yield often is reduced by insufficient water and/or nutrient supply resulting in the so-called water-limited or nutrient-limited yield potential (van Ittersum et al., 2003). Pests, diseases, and competition with weeds can further reduce the water/nutrient-limited yield potential down to the actual yield achieved by a farmer on a given field (Cassman et al., 2003). The difference between the actual and potential yield represents a yield gap that can be reduced with adequate agricultural management of water, nutrients, and pests (Cassman et al., 2003). Unfortunately, the occurrence of yield gaps caused by water scarcity cannot always be foreseen and prevented, especially in regions where irrigation is typically not used (Ceglar et al., 2016; Ward and Hohmann, 1988). The exact response of crops to drought also is highly variable, and depends on crop type (Prasad et al., 2008). In general, crops respond to drought stress with a decrease of leaf production, a reduction in leaf area index (LAI), an increase in senescence rate, followed by a reduction of the yield (Baret et al., 2007). The actual crop growth and yield are influenced by additional factors, such as the amount and timing of precipitation, soil physical properties, and soil horizon distribution because all these factors have an effect on the plant-available soil water (Krüger et al., 2013; Lück et al., 2009). Therefore, understanding the spatial variability of water stress and crop yield is essential (Wong and Asseng, 2006). Unfortunately, our ability to predict within-field variability of crop stress and the resulting reduction in crop growth is still rather limited (Batchelor et al., 2002). One important reason for this is that detailed high-resolution information on the soil characteristics required to successfully predict crop growth (Boenecke et al., 2018) is typically not available.

Local differences in shallow soil properties (~1-2 m max depth), such as soil horizon thickness and texture, are known to influence soil water movement and retention as well as nutrient availability and root growth. Over the last decades, great efforts in soil surveying have resulted in the production of a variety of commonly available thematic maps that provide information on soil characteristics (e.g., geological, soil, and yield potential maps). Nevertheless, these general-purpose maps are not always suited to actual farming applications (Della Chiesa et al., 2019). For example, they are often insufficiently detailed to be used in precision agriculture (Robert, 1993) or to support the identification and management of within-field differences in crop performance (Franzen et al., 2002; Nawar et al., 2017; Robert, 1993). The inadequate reproduction of this site-specific soil heterogeneity can be explained by the sparse and time-consuming point-scale direct soil sampling methodology on which these thematic maps are based (Gebbers and Adamchuk, 2010; Heuvelink and Webster, 2001). As a

result, soils are discretized in relatively large polygons that are not provided with a quantitative description of soil texture and layering (Krüger et al., 2013). Therefore, a more accurate spatial description of soil properties is frequently needed to predict spatial variability of crop growth (Krüger et al., 2013). This need is a key driver for the increasing demand for reliable high-resolution soil maps at scales larger than the field-scale.

Geophysical tools have shown great potential to support precision agriculture and agro-ecological modelling as they allow a non-invasive investigation of the subsurface. This potential has also been realized in the broader field of hydrology, which resulted in the emergence of the interdisciplinary field of hydrogeophysics in the past two decades (Binley et al., 2015). It has been shown that hydrogeophysical methods provide a suitable alternative to direct sampling (Robinson et al., 2008). The most widely used hydrogeophysical methods to investigate the shallow soil are sensitive to the soil electrical properties, such as ground penetrating radar (GPR), electromagnetic induction (EMI), and electrical resistivity tomography (ERT). These methods have often been used to estimate water content, soil textural properties, mineralization, porosity, or residual pore water content (Rubin and Hubbard, 2005) and are capable of producing catchment-scale datasets that are often useful in hydrological studies (Robinson et al., 2008). Nevertheless, few studies used geophysical measurements in agricultural applications. In addition, much hydrogeophysical research has so far been directed at plot- and field-scale experiments (Binley et al., 2015). However, EMI methods are well suited for vehicle-towed platforms that can be easily attached to all-terrain vehicles (ATV) or tractors (André et al., 2012; Sudduth et al., 2001), thus considerably increasing the feasible survey-scale well beyond that of a single plot or field.

1.1. Electromagnetic induction (EMI)

EMI is a highly mobile geophysical tool that is particularly promising for the characterization of spatial variability in soil properties (Robinson et al., 2012; van Dam, 2012). EMI measures the apparent electrical conductivity (ECa) of the ground, which can be related to soil properties, such as water content, pore water conductivity, soil porosity, and soil texture (Corwin and Lesch, 2003; Sheets and Hendrickx, 1995). Some EMI instruments, for example the EM38 and its variants EM38DD and EM38Mk2 (Geonics Limited, Mississauga, Ontario, Canada) or the Profiler EMP-400 (Geophysical Survey Systems, Inc., Salem, Massachusetts, USA), have been widely used to map soil characteristics even if the vertical resolution that they provide is rather limited. For EMI instruments, the depth of investigation (DOI) depends

on the distance between the transmitter coil and the receiver coil as well as on the coil orientation (McNeill, 1980). Since the above mentioned instruments are provided with only one or two coil separations or orientations, they can measure a maximum of two or four DOIs in two separate passages. Nevertheless, a considerable number of studies have used these EMI instruments to map key soil characteristics within an agricultural context. Among others, they were used by André et al. (2012) to highlight anthropogenic soil compaction in a vineyard in South France and by De Benedetto et al. (2013) to delineate areas that require different water management. Machado et al. (2015) used these EMI instruments to determine cation exchange capacity (CEC) of an agricultural field, and Yao et al. (2016) used them to map the spatial distribution of soil salinity of a coastal agricultural area and related this to crop yield. Other studies used these EMI instruments to identify variations in soil texture and layering. For example, Kelley et al. (2017) mapped soil texture of irrigated fields and Mertens et al. (2008) mapped the depth of loess layers above coarse sediments and found a clear relation between soil depth and crop yield.

Despite these promising results, EMI methods have primarily been considered as a qualitative mapping tool (Binley et al., 2015). One of the main reasons for this is the low vertical resolution of the soil characteristics obtained with the afore-mentioned EMI instruments. Recently, new EMI instruments with multiple coil separations and orientations provide improved vertical resolution (Doolittle and Brevik, 2014). Even if such multi-coil systems have not been widely used for soil characterization yet (von Hebel et al., 2014), their added value has been shown in some studies. For example, Saey et al. (2009) showed that the improved vertical resolution of the four-coil DUALEM-21S (DUALEM, Milton, ON, Canada) system allowed to obtain maps of the depth to clay-rich horizons without the need for ground truth sampling, which was essential when using the simpler EM38DD system. Similarly, the DUALEM-21S EMI system was successfully used to reconstruct the depth of a coarse substrate by De Smedt et al. (2011). A second multi-coil instrument that became recently available is the DUALEM-421S (DUALEM, Milton, ON, Canada), which provides six simultaneous ECa readings. A series of recent studies with this device have focused on soil salinity (Huang et al., 2017a; Stockmann et al., 2017; Zare et al., 2016). However, the DUALEM-421S system was also used by Huang et al. (2017b) to perform time-lapse measurements and monitor soil water content dynamics, and Monteiro Santos et al. (2010) used this system for discerning changes in soil properties with depth. A further multi-coil EMI instrument that was successfully used within an agricultural context is the three-coil CMD

MiniExplorer (GF Instruments, Brno, Czech Republic). For example, Jadoon et al. (2015) used this system to characterize patterns in the distribution of soil salinity in a drip irrigation system, and Stadler et al. (2015) and Rudolph et al. (2015) used this instrument to quantitatively link ECa maps, soil characteristics, and crop growth and performance during periods of water stress. Recently, von Hebel et al. (2018) combined the CMD MiniExplorer with an additional six-coil CMD MiniExplorer Special Edition to investigate soil-plant interactions by comparing EMI data with measures of crop performance obtained from airborne hyperspectral data.

Despite the potential of EMI instruments for the characterization of large-scale areas, most studies were confined to the plot- or field-scale (<10 ha). Only a few studies have also used EMI measurements for soil characterization at scales larger than the field-scale (> 10 ha). Generally, very large areas of tens of km^2 can be investigated with EMI by performing point-scale measurements at selected locations followed by an interpolation to larger areas using information from other proximal or remote sensing techniques. Such a point-scale approach combined with Landsat-TM images was used by Ding and Yu (2014) to assess soil salinity over a large area of approximately 10000 km^2, whereas Zare et al. (2016) used EMI in combination with airborne gamma-ray spectrometry to identify soil landscape units in a 270 km^2 area. However, very few studies performed high-resolution EMI surveys beyond the field scale. The study of Frederiksen et al. (2017) is one of the few examples where high-resolution EMI measurements were acquired for an area of 1000 ha using a spacing of approximately 20 m between EMI lines. This general lack of large-scale studies can be explained by the fact that EMI measurements are usually performed in a limited time window to minimize temporal variations in dynamic soil characteristics within the EMI survey (e.g., water content and soil temperature) (Frederiksen et al., 2017). However, this might not always be feasible, especially in complex agricultural areas characterized by multiple fields with different crops and variable harvest times.

A further disadvantage of EMI measurements is that the spatial variation in ECa is often difficult to interpret in terms of a single soil property. In the absence of direct correlations between EMI measurements and a single soil property, a range of studies have used clustering or classification of EMI data to identify zones with similar soils. These zones are of particular interest in agriculture, especially in precision agriculture where within-field site-specific agricultural management is used to optimize crop productivity (van Schilfgaarde, 1999).

Clustering of ECa maps has been widely used to identify proper management zones that can be treated homogeneously within precision agricultural applications. These management zones often corresponded well with historical yield maps as the properties that contribute to high conductivity readings (such as low sand content and high clay and moisture content) are usually the same that characterize fertile soils (King et al., 2005). Many of these zonation studies relied on a combination of ECa maps and historical yield maps (e.g., Taylor et al., 2003; Galambošová et al. 2014) or on the combination of EMI and direct soil sampling (e.g., Oldoni and Bassoi, 2016).

Other studies also considered proximal and remote sensing techniques in addition to ECa maps to identify management zones as commonly used EMI sensors can fail to distinguish between contrasting soils under certain circumstances (Castrignano et al., 2012). For example, Jing et al. (2017) and Huang et al. (2014) combined EMI with gamma-ray spectrometry and Castrignano et al. (2012) added digital elevation data recorded with a real-time kinematic GPS to these two sensors. Furthermore, EMI was combined with GPR and remotely sensed imagery by De Benedetto et al. (2013) and Ciampalini et al. (2015) combined EMI with airborne hyperspectral images. In most cases, the combination of different sensors provided improved results. However, the best combination of sensors likely depends on site-specific requirements (Castrignano et al., 2012) and it must be considered that the benefits provided by the additional information may not outweigh the additional measurement costs (Taylor et al., 2010). A commonality of the abovementioned studies was the focus on the field-scale and the use of a single or a limited number of EMI configurations only. Overall, the applicability and utility of clustering EMI data to identify areas with similar soil properties have not yet been demonstrated for large-scale multi-configuration EMI data sets consisting of EMI measurements taken at different times and for a range of investigation depths.

1.2. Crop modelling for agricultural applications

As previously mentioned, a number of factors can reduce crop yield (Evans and Fischer, 1999). The adverse effects of low water and nutrient availability can be mitigated by agricultural management, as it is the case for the prevention and control of pests and diseases. It is therefore vital to quantify both the negative effects of water and nutrient shortage on crop yield as well as the positive effect of management actions to mitigate these shortages (i.e., irrigation and fertilizer applications). An effective method to quantify the influence of water availability on crop growth is the use of process-oriented crop growth models (Batchelor et

al., 2002). These models allow the simulation of the temporal interaction of water stress and crop development with a high temporal resolution. Therefore, they can be used to provide yield predictions for various environments and meteorological conditions (van Ittersum et al., 2003) and have the potential to answer a variety of questions relevant for research, management, and policy (Boote et al., 1996)

Common crop-specific models to simulate crop growth for given environmental conditions are ORYZA2000 for rice (Bouman, 2001), APSIM-wheat (McCown et al., 1996), CROP-Soybean (Hoogenboom et al., 1994), CWRES-Maize (Jones and Kiniry, 1986) and CERES-Wheat (Ritchie, 1985), amongst many others. Popular multi-crop models with modules that account for water and nutrient limitations and the effects of pests, diseases and weeds are LINTUL (Spitters and Schapendonk, 1990) and SUCROS (Spitters et al., 1989). Other widespread multi-crop models are Aquacrop (Steduto et al., 2009), Cropsyst (Stockle et al., 1994), APSIM (McCown et al., 1996), ARIDCROP (van Keulen, 1975), and WOFOST (Van Diepen et al., 1989). Crop growth models are also included in broader decision support systems such as DSSAT (Jones et al., 2003), which is provided with a template crop module that simulates certain crop varieties but can be set to implement additional crop models such as the CERES models to increase the variety of crops that can be simulated. DSSAT was also successfully coupled to HYDRUS-1D to obtain accurate simulation of vertical soil water dynamics (Shelia et al., 2018). A further example of coupling multiple models is the agro-ecosystem model AgroC which is a one-dimensional model that couples SUCROS with SOILCO2 (Šimůnek and Suarez, 1993) for simulating water, heat and CO_2 fluxes and RothC (Coleman and Jenkinson, 1996) for simulating soil organic carbon turnover (Klosterhalfen et al., 2017).

Crop models are sometimes used as a tool for decision-making in agricultural management since they have been demonstrated to adequately simulate crop growth (Boote et al., 1996). Therefore, crop models can potentially help farmers in increasing their profit by identifying factors that can be controlled and managed (Paz, 2000). Such models require inputs for management practices (such as crop variety, plant population and row spacing, fertilizers and irrigation applications) and environmental conditions (such as soil type, temperature, precipitation, humidity, and solar radiation). Crop development is simulated from these inputs with model-specific time steps and is generally influenced by water and nitrogen stress, growth stage, and photosynthetic activity (Paz, 2000). Some crop growth models have been

successfully applied to simulate the spatial variability of yield (Batchelor and Paz, 1998) produced by variations in soil moisture availability (Paz et al., 1998). Examples of further applications of crop models include the simulation of the yield gap for corn in a cool climate due to abiotic stress (Žydelis et al., 2018), the optimization of nitrogen fertilizer prescription (Paz et al., 1999), and the validation of management zones obtained by classifying normalized difference vegetation index (NDVI) maps obtained from satellite remote sensing (Basso et al., 2001).

Crop models are also used at scales larger than farm scale (van Ittersum et al., 2003) as they can be used to simulate growth, development, and yield of a certain crop on a presumed homogeneous unit which can be either a field plot, a large cropped field, a regional catchment, or a pixel with variable size. For example, Chipanshi et al. (1999) used the CERES-wheat model to simulate crop growth for three major soil types distributed over a large area of 20000 km^2 and obtained reasonably accurate yield estimates. Furthermore, Liu et al. (2007) combined the EPIC crop model with a geographic information system (GIS) to simulate yield for a 10-year period using actual water and nutrient supply with a resolution of 30 arc-minutes (~50 x 50 km at the equator) with a global coverage.

Despite these large-scale applications, it must not be overlooked that a process-oriented crop growth model typically relies on a one-dimensional description of water flow in the soil column (Vereecken et al., 2016) in which a detailed description of the soil profile characteristics, including soil hydraulic properties, is key to obtain meaningful yield predictions (Boenecke et al., 2018). This is a major challenge for agro-ecosystem simulations for large areas, since, as previously mentioned, this information is generally obtained from general-purpose maps (Boenecke et al., 2018) that do not adequately represent field-scale soil heterogeneity. Within this context, geophysics-based soil mapping seems a viable strategy to address the need for high-resolution soil information as a range of geophysical properties have been shown to provide useful proxies for soil properties in precision agriculture (Adamchuk et al., 2004; Allred et al., 2008; Gebbers and Lück, 2005; Grisso et al., 2005; Vitharana et al., 2008). In particular, EMI has been used to provide detailed soil information in support of agro-ecosystem modelling. For example, Krüger et al. (2013) used EMI and GPR to characterize site-specific variations in soil properties, and this improved simulations of soil water dynamics and biomass production on a 4.4 ha field. Wong and Asseng (2006) used EMI to map plant-available water content and performed simulations that illustrated how variations

in available water interacted with the amount and timing of precipitation and caused yield variability within a single 70 ha field. Similarly, Boenecke et al. (2018) used EMI mapping as a basis for simulating the spatial variability of soil water content and yield at the farm scale (30 ha). Despite these successful examples, there is a general lack of studies linking soil maps to modelling applications at a scale larger than the single farm (Krüger et al., 2013) and for multiple crops. It is clear that a successful simulation of the spatial variability of water stress and the associated decrease in crop productivity within large and complex agricultural environments could lead to significant improvements in our knowledge of the soil-plant system. Such knowledge could provide a valuable support for the development of long-term strategies for decision-making in agricultural management (Krüger et al., 2013). However, the added value of geophysical data compared to general-purpose soil maps has not been quantified yet for such large and complex areas.

1.4. Objectives and outline

The overall aim of this thesis is to quantify the added value of geophysical mapping alongside point-scale soil sampling to obtain high-resolution information on soil characteristics for the simulation and prediction of the spatial variability of water-limited crop growth and yield. In order to achieve this, the following three sub-objectives have been defined.

The first sub-objective is to develop a geophysics-based digital soil mapping strategy that exploits the strengths of multi-configuration EMI instruments in combination with a limited number of direct point-scale soil samples. In a complex km^2 scale agricultural area, this strategy should have the potential for a relatively cost-effective characterization of the small-scale variability of soil structural properties (e.g., soil layering and texture) that are responsible for yield gaps. It should result in a soil map that successfully reproduces spatial patterns in crop performance determined from independent satellite images.

The second sub-objective is to investigate how field-scale patterns in soil properties obtained using geophysical mapping affect the spatial variability of soil water content dynamics and growth of multiple crops at the km^2 scale by using spatially distributed one-dimensional agro-ecosystem models. For this, the spatio–temporal variations of crop growth and yield will be simulated, and the results will be validated with independent remotely sensed data. To achieve this, an approach will be developed to estimate the necessary soil hydraulic properties from the information of the geophysics-based soil map. This approach should return simulations of

soil water content dynamics that are comparable to measurements from long-term monitoring stations placed at key locations within the investigated area.

The third and final sub-objective is to assess the added value of the geophysics-based soil representation for the modelling of crop growth and yield. For this, the improvement in the correspondence between observed and simulated crop growth and yield that is obtained by using this advanced soil representation will be compared to the use of commonly available soil maps. This comparison should provide insights on the importance of an accurate representation of soil distribution, layering, and texture, and thus on the added value of geophysics-based soil mapping for agricultural applications.

To address these objectives, the thesis is organized as follows. After this introductory Chapter 1, a description of the study area is provided in Chapter 2. Here, the climatic, geological, and morphological characteristics of the study area are presented and the motivations behind the selection of the site are provided. A characterization of the land use and agricultural setting is then provided and this is followed by a description of the meteorological and ancillary data acquisition.

In Chapter 3, EMI measurements combined with soil sampling are used to map the soil characteristics of the area described in Chapter 2. First, a description of the measurement methodology is given. Then, an interpretation of the main geomorphological features based on the acquired multi-configuration EMI measurements and additional commonly available soil maps is provided. Next, a supervised classification methodology is developed to subdivide the geophysical maps into areas with similar soil properties. The resulting classified EMI map is then combined with direct soil sampling to produce a high-resolution soil map divided into management zones with typical soil properties. Finally, the correspondence of the soil units with patterns in crop performance obtained from remote sensing is evaluated.

Chapter 4 starts with a description of the agro-ecosystem model AgroC. Next, the geophysics-based soil map developed in Chapter 3 is used as input to perform agro-ecosystem simulations for the six common crop types in the study area. The hydraulic parameters are estimated from the information obtained in Chapter 3 by using pedotransfer functions (PTF). The simulations are compared with measured water content at selected locations. Then, the water stress simulated with AgroC and the resulting impact on simulated LAI is compared with LAI_{NDVI}

obtained from satellite images. Simulated productivity at harvest is compared with the actual harvest data or with literature values. Finally, maps of simulated productivity at harvest are shown and their potential is discussed.

In Chapter 5, the agro-ecosystem simulations derived with the geophysics-based soil map discussed in Chapter 4 are compared to simulations based on two general-purpose soil maps. First, a qualitative comparison between the soil descriptions provided by the three maps is provided. Then, the LAI simulated with AgroC by using inputs from the three soil maps is compared with independent LAI_{NDVI} values obtained in Chapter 4. The added value provided by the geophysics-based soil map is discussed first for the simulation of five crop types over the entire study area, and then in more detail for the simulation of sugar beet. Finally, it will be discussed in which conditions the geophysics-based soil characterization provides an added value for the simulation of the spatial variability of crop growth.

The thesis concludes with Chapter 6, which provides the overall conclusions of the thesis and an extensive outlook that illustrates remaining research gaps and needs for further research.

Chapter 2

Study area

This study was conducted in an agricultural area near Selhausen in the Rur Catchment (North-Rhine Westphalia) approximately 40 km west from Cologne, Germany (50°51'56"N, 6°27'03"E). The climate of the study site is characterized by a mean annual precipitation of 715 mm and a mean annual temperature of 10.2°C (Rudolph et al., 2015). The shape of the study area is a square of 1x1 km bearing 12.75° east (Figure 1a). The exact position and orientation were selected to cover a large area while excluding visible anthropogenic artifacts. On the eastern side, a power grid and a power plant bound the study area. On the western side, the study area extends until a railway track that runs N-S from Jülich to Düren. The northern and southern boundaries are a consequence of the previously mentioned considerations and of the square geometry of the study area. The 1 km^2 area is divided into 51 fields ranging in size from 0.5 to 9.6 ha. These fields are cultivated in rotation with winter wheat, winter barley and sugar beet. Occasionally, potato, maize, winter raps, and oats are grown. According to the German cadaster, there are 52 different land owners but the effective number of farmers is lower than twenty because of kinship and lease. Nevertheless, this large number of active farmers leads to a heterogeneous field management.

To obtain geomorphic information, a digital elevation model (DEM) with spatial resolution of 1 m (Scilands-GmBH, 2013) was used. The study area is morphologically divided in two terraces with an altitude that ranges between approximately 101 m for the western lower terrace and 113 m a.s.l for the eastern upper terrace. The two terraces are separated by a slope that ranges from 2% to 10% with a westbound dip and an approximately NNW-SSE strike. This characteristic feature corresponds with the subdivision between two quaternary fluvial

terraces but its origin may also be connected to the tectonic structure of the study area that is characterized by a series of normal step faults striking NNW-SSE, the so called Rurrand-Störung (Walter, 2010). The shape of this slope may have been modified by human activity since the area of the lower Rur has been inhabited and farmed for about the last 7000 years and the topography of the study area is known to have been reshaped to facilitate agriculture. Further anthropogenic activity during WWII might also have shaped the area since the Rur river represented a strategic defense line during the allied invasion of Germany. In this area, the front was stationary from the beginning of the Battle of the Bulge (December 1944) until the end of Operation Grenade (February 1945) with massive bombing runs on the city of Düren and on the nearby defensive structures, some of which were located within the study area (USAAF, 1944).

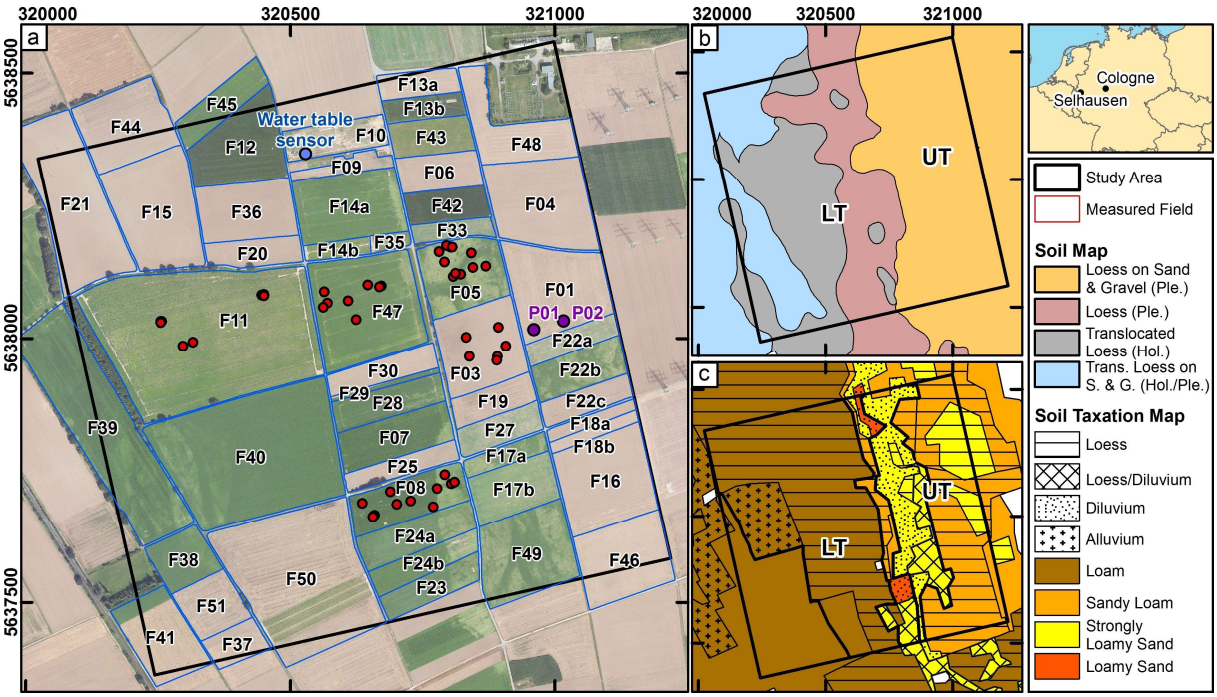

Figure 1: a) Satellite image of the study area (ESRI, 2015) with the investigated fields and respective codes, the location of the water table sensor, the soil water content measurement points P01 and P02, and the locations of the in situ LAI measurements (red dots), b) digitized main features of the 1:5000 soil map (sheets 510410 and 510411) with the locations of the upper terrace (UT) and lower terrace (LT), c) digitized Soil Taxation Map (NRW, 1960) sheets 510410 and 510411.

The shallow geology of the study area is divided in two main geological features consisting of quaternary sediments of the upper and lower terrace. According to the 1:5000 soil map (Figure 1b), the upper terrace consists of Pleistocene sand and gravel sediments associated with the Rhine/Meuse river system (Röhrig, 1996). This terrace is characterized by a system

of subsurface channels eroded in the sand and gravel sediments, which was subsequently buried by aeolian sediments of variable thickness (Klostermann, 1992; Patzold et al., 2008; Vandenberghe and van Overmeeren, 1999). The lower terrace consists of Pleistocene loess sediments and translocated loess sediments from the Holocene (Figure 1b). Similar to the upper terrace, part of the translocated loess of the lower terrace is deposited on Pleistocene/Holocene sand and gravel sediments (Röhrig, 1996). The dominant reference soil groups in the area are Cambisols, Luvisols, Planosols, and Stagnosols (WRB, 2015).

2.1. Influence of soil heterogeneity on crop performance

Previous research in this area showed that crop performance during periods of drought is strongly influenced by soil heterogeneity at the field scale and beyond (Rudolph et al., 2015; Simmer et al., 2015; Stadler et al., 2015). Generally, a reduction in performance of sugar beet, corn, and cereals in the shape of a variety of narrow and undulated channels (Rudolph et al., 2015) can be observed in satellite images and in field observations (Rudolph et al., 2015; Stadler et al., 2015; von Hebel et al., 2018). These patterns are visible in different years and at different scales. For example, field-scale patterns in crop performance of sugar beet and corn are shown in two recent drone photos from a drought period in summer 2018 (Figure 2a-b).

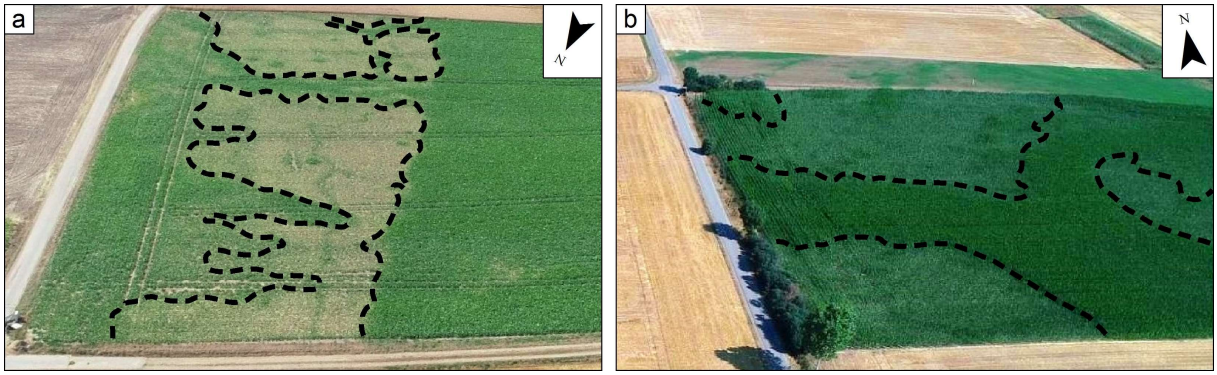

Figure 2: Drone photos of patterns in crop performance at the 22nd of July 2018 for a) sugar beet in fields F-08 and F-24a, and b) corn in field F-05 (courtesy of Prof. Dr. F. Jonard).

At a larger-scale, patterns in crop performance of sugar beet are locally found within the study area as shown in a satellite image from a drought period in summer 2015 (Figure 1a). By analyzing the large-scale patterns presented in Figure 1a, the fields with visible patterns in crop performance of sugar beet can be divided into three groups. First, some fields that are entirely located within the upper terrace (fields F05, F17a, F22b, and F49 in Figure 1a) show patterns that are associated with sand and gravel channels that are buried in aeolian sediments.

Second, some fields that are located at the boundary between the two terraces (fields F07, F14a, F23, F24a-b, and F47 in Figure 1a) show a reduction of crop performance in the part of the field that is located in the upper terrace (Rudolph et al., 2015). Finally, some fields of the lower terrace (fields F39 and F40 in Figure 1a) show patterns in crop performance that appear similar to those found in the upper terrace. Although the lower terrace has not been intensively investigated yet, the satellite image suggests that a connection between subsurface structures and crop performance is also present in the lower terrace.

Figure 1c shows a digitization of the soil taxation map (NRW, 1960) of the study area (sheet 510410 in the west and 510411 in the east). This map shows the yield potential of the agricultural land at a scale of 1:5000 and provides soil profile information up to a depth of 2.0 meter. In this map, the upper terrace is characterized by a strong heterogeneity in soil type and origin with a general north-south orientation. The upper terrace is composed of sandy loam of aeolian origin in the eastern part whereas the western part near to the slope that divides the two terraces is composed of strongly loamy sand of aeolian and alluvial origin (Figure 1c). In contrast, the lower terrace is entirely composed of loamy sediments that are generally of aeolian origin and locally of alluvial origin. Within the lower terrace, a large area in the South-West is not provided with genesis data. In general, this map represents the most detailed available soil information for the selected study area. However, it appears that it is not capable of representing the complexity of the subsurface for this particular study area. This is evident from a comparison with the observed patterns in crop performance shown in Figure 1a. The lack of detail in the soil taxation map is mainly due to the low sampling density of one drilling per 40-50 m used during mapping.

2.2. Status of the study area in 2015 and 2016

In this thesis, the analysis of the study area will be focused on crop performance in late 2015 and 2016. For this reason, information on crop type, emergence dates, and harvesting dates was recorded during 2016. The land use map shown in Figure 3 was produced by digitizing field geometries retrieved from satellite images (ESRI, 2015) and by field mapping to record the land use of each field. As shown in Table 1, a small percentage of the area was characterized by bare soil, oat, and grass in late 2015 and in 2016 (4.4% of the total area). In these cases, no further data were collected. Corn, potato, sugar beet, winter barley, winter rapeseed, and winter wheat were grown on larger areas (Table 1). For these crops, the emergence and harvesting dates were recorded. It has to be noted that various emergence and

harvest dates were recorded in separate fields for the same crop. However, these differences were rather small (e.g., within 3-10 days for emergence and within 1-5 days for harvest dates). Therefore, it was assumed that each crop type was characterized by a maximum of two different emergence dates and by a single harvesting date. The resulting emergence and harvest dates for each crop are given in Table 1 together with the total area.

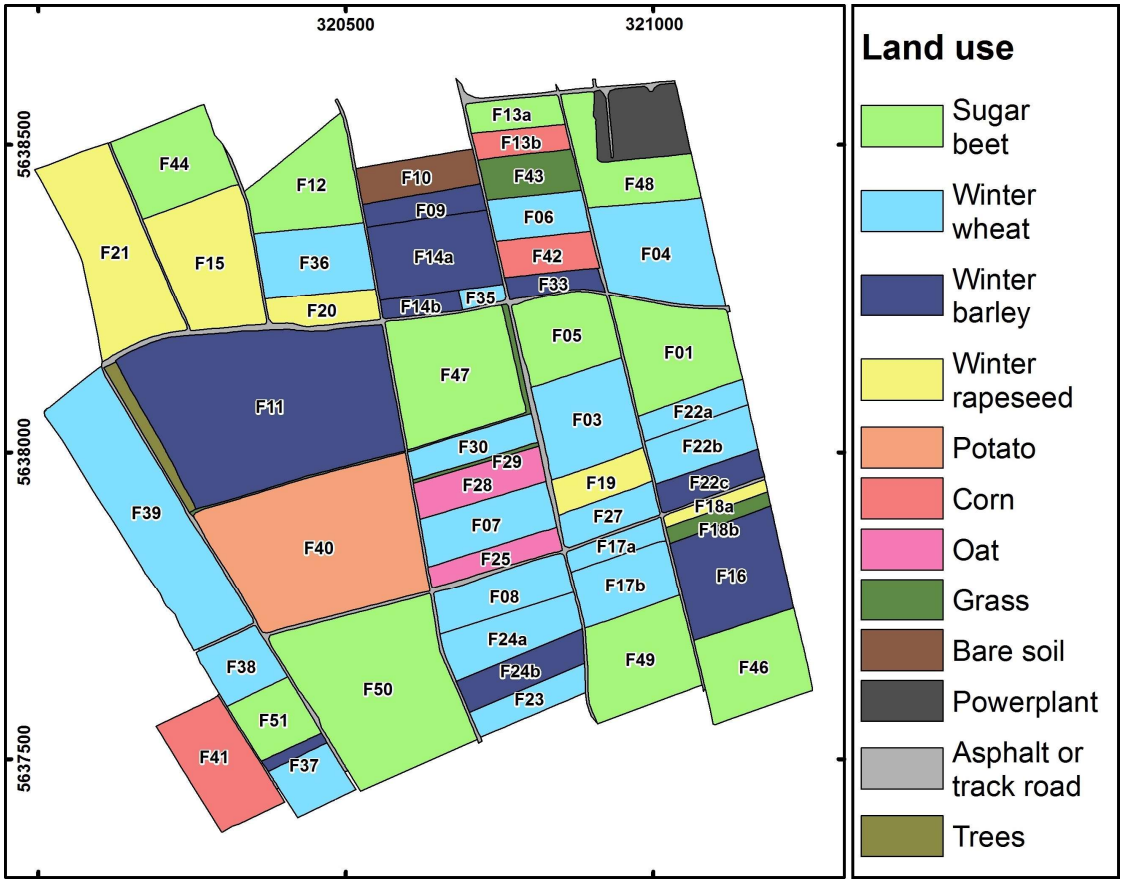

Figure 3: Crops and land use types of the study area in 2016.

Within the study area, a 2.3 ha field cropped with sugar beet field F01) and a 9.5 ha field cropped with barley (field F11) were investigated in more detail (see Figure 1). In both fields, the productivity at harvest in 2016 was provided by the respective field owners. Sugar beet was grown in field F01 and the wet weight of harvested beet roots was 61.4 tons per ha (t ha^{-1}). This weight was reduced by 76.8% to obtain the dry weight of harvested storage organs (FAO, 1999), which thus was 14.25 t ha^{-1} for field F01. Winter barley was grown in field F11 in 2016. Here, the productivity at harvest of barley grains was 7.90 t ha^{-1} with 13% moisture content (i.e., a dry weight of 6.87 t ha^{-1}). Further data on the average wet weight of sugar beet yield were available for field F11 for different growing seasons. On average, 83.53 t ha^{-1} of

wet beets were harvested in 2011, 2014, and 2017, which corresponds to a dry weight of 19.38 t ha^{-1}.

Table 1: Total area in ha of the crop and land use types that were present in the study area in late 2015 and in 2016 with emergence and harvest dates for those crops that are found on more than three ha in total.

Plant	Area (ha)	Emergence	Harvest
Sugar beet	26.5	02.05.2016	14.11.2016
Winter wheat	26.2	15.11.2015	29.07.2016
Winter barley	18.2	1/10.12.2015	25.07.2016
Winter rapeseed	9.2	1/10.11.2015	20.07.2016
Potato	7.1	15.5.2016	20.10.2016
Corn	3.5	1/10.05.2016	20.10.2016
Oat	2.1	NA	NA
Bare soil	1.1	NA	NA
Grass	1.0	NA	NA

2.3. Meteorological and ancillary data

The study area is part of the Terrestrial Environmental Observatories (TERENO) network (Bogena et al., 2018; Schmidt et al., 2012; Simmer et al., 2015). Several meteorological and ancillary measurements are being performed in one field located approximately in the center of the study area (field F11 in Figure 1). Here, continuous measurements of the following meteorological parameters were performed in 2015 and 2016: air temperature and relative humidity (HMP45C sensor, Vaisala Inc., Helsinki, Finland), precipitation (RM-52203 tipping bucket rain gauge, R.M. Young Company, Traverse City, USA), soil temperature at a depth of 0.5 cm (TCAV temperature thermocouple probe, Campbell Scientific, Inc., Logan, UT, USA), global radiation (NR01 net radiometer sensor, Hukseflux Thermal Sensors, Delft, Netherlands), wind speed (CSAT3 three dimensional sonic anemometer, Campbell Scientific, Inc., Logan, UT, USA), and air pressure (LI7500 open-path infrared gas analyzer, LI-COR Inc., Lincoln, NE, USA).

In the upper terrace, two locations were selected within field F01 (P01 and P02 in Figure 1) to monitor volumetric soil water content from 28th of April 2016 to 18th of October 2016. At each location, two SMT-100 soil water content sensors (Truebner GmbH, Neustadt, Germany) were installed at three depths (10 cm, 20 cm, and 50 cm). These sensors were calibrated to provide soil dielectric permittivity before installation (Bogena et al., 2017) and the volumetric soil water content was obtained using the equation of Topp et al. (1980).

Chapter 3

Large-scale soil mapping using multi-configuration EMI and supervised image classification

In this chapter*, it will be shown how electromagnetic induction (EMI) measurements combined with soil sampling can be used to map soil characteristics. First, a detailed geophysical survey that was performed in the study area in 2016 will be described. Then, it will be shown how an interpretation of the main geomorphological features of the study area was performed by using geophysical measurements and commonly available soil maps. This interpretation allowed a subdivision of the study area in four sub-areas with characteristic sediments and EMI response. In a following step, it will be described how a supervised classification methodology was used to subdivide the maps that were obtained from geophysical data into areas with similar soil properties. Soil profile descriptions to a depth of 2 m were obtained at 100 sampling locations and it will be shown that the combination of the classified EMI map with ground truth data resulted in a 1 m resolution soil map with eighteen units with typical soil profiles and texture information. Finally, it will be shown that this high-resolution geophysics-based soil map corresponded well with patterns in crop performance obtained from satellite imagery.

* This chapter is adapted from a journal article published as:
Brogi, C., Huisman, J. A., Pätzold, S., von Hebel, C., Weihermüller, L., Kaufmann, M. S., van der Kruk, J., Vereecken, H., (2019): Large-scale soil mapping using multi-configuration EMI and supervised image classification. *Geoderma* 335, 133-148, doi:10.1016/j.geoderma.2018.08.001.

3.1. Materials and methods

3.1.1. Electromagnetic induction (EMI) measurements

Frequency domain EMI systems generate a fixed frequency alternating current through a transmitter coil, which generates the primary magnetic field. This primary magnetic field induces eddy currents in the electrically conductive subsurface, which in turn generate a secondary magnetic field. The ratio between the secondary and primary magnetic field is related to the apparent electrical conductivity (ECa) and, to a lesser degree, to the apparent magnetic permeability over a certain depth range that depends on the source-receiver coil distance and orientation (Keller and Frischknecht, 1966; Ward and Hohmann, 1988).

3.1.1.1. EMI instrumentation

Measurements were performed by simultaneously using two EMI instruments: i) the CMD MiniExplorer (ME) with three receiver coils and coil separations of 32, 71, and 118 cm oriented in vertical coplanar configuration (VCP) and ii) a custom-made CMD MiniExplorer Special Edition (SE) with six receiver coils and coil separations of 35, 50, 71, 97, 135, and 180 cm (GF instruments, Brno, Czech Republic) oriented in horizontal coplanar configuration (HCP) to collect data using both VCP and HCP configurations at the same time (Table 2).

Table 2: EMI instrument configurations, coil separations, depth of investigation (DOI) and frequency for the CMD Mini Explorer and the CMD Mini Explorer Special Edition.

EMI instrument	Receivers	Orientation	Separation [cm]	DOI [cm]	Frequency [kHz]
Mini Explorer	3	VCP	32	0-24	30.00
		VCP	71	0-53	
		VCP	118	0-89	
Mini Explorer Special Edition	6	HCP	35	0-52	25.17
		HCP	50	0-75	
		HCP	71	0-107	
		HCP	97	0-146	
		HCP	135	0-203	
		HCP	180	0-270	

Figure 4 shows the depth-specific sensitivity of all EMI measurements in VCP and HCP orientation to the subsurface electrical conductivity distribution (McNeill, 1980). The VCP orientation is most sensitive to the shallow subsurface and becomes less sensitive with

increasing depth, while the HCP orientation is less sensitive to the shallow subsurface and the sensitivity peaks at a depth of around 0.4 times the coil separation (McNeill, 1980). As a rule of thumb, the depth of investigation (DOI) for VCP is approximately 0.75 times the coil separation (s) and the DOI for HCP is approximately 1.5 times the coil separation. This result in DOI's ranging from 0-24 to 0-270 cm for our measurements set-up.

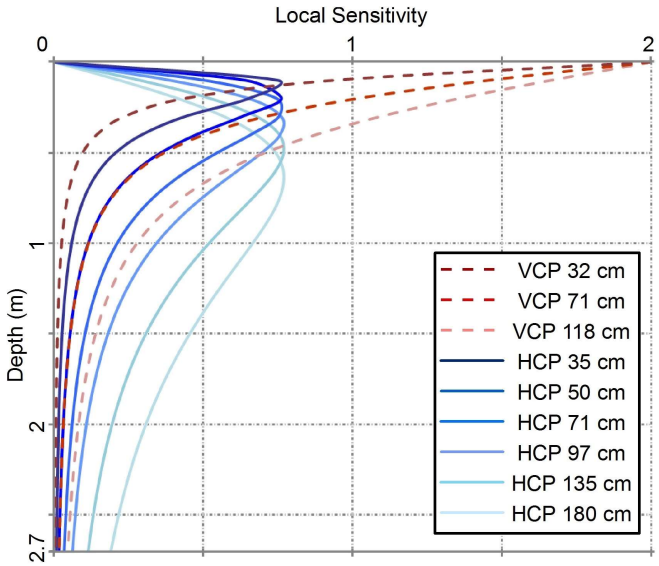

Figure 4: Local sensitivity function for the nine coil separations in the VCP and HCP loop orientation with the separations that are shown in Table 2.

3.1.1.2. EMI survey

The EMI measurements on the 51 agricultural fields (102 ha) shown in Figure 1a were performed between April and December 2016 within a few days after harvest of the different crops. For each field, a standardized measurement protocol based on best practice EMI measurements was followed (European Committee for Standardization, 2011). The EMI instruments were mounted on two plastic sleds that were separated by 1.5 m. A quad-bike ATV was used to pull the sleds while keeping a distance of 4 m from the first sled (Figure 5). The driving speed ranged from 5 to 7 km h^{-1}. The sampling frequency was 5 Hz, which resulted in an in-line resolution of approximately 0.3 m with a track spacing of 2.0 to 2.5 m. The EMI measurements were made in the direction of ploughing to avoid possible effects of terrain roughness on the EMI measurements.

A single frequency GPS (NovAtel inc., Calgary, Canada (see Rudolph et al., 2018)) was used to provide spatial position during the measurements from April to October 2016 (a total of 76 ha). A TRX centerpoint DGPS system (Trimble inc., Sunnyvale, USA) with higher accuracy

was used from November to December 2016 for a total of 21 ha. Despite the difference in accuracy between the single frequency GPS system (meter accuracy) and a DGPS system (cm accuracy), the measurements obtained with the two GPS systems were considered equally reliable for the purpose of this work. Each field was measured continuously and the first line of EMI measurements was repeated at the end of each field survey to verify that no unexpected shifts in the measured ECa occurred. In general, the difference in ECa values measured at the start and at the end of each survey was negligible.

Figure 5: Example of the EMI measurement setup. The ATV is used to pull the CMD MiniExplorer (first plastic sled) and the CMD MiniExplorer Special Edition (second plastic sled). A GPS/DGPS unit that is connected to the EMI device is positioned on top of each sled.

3.1.1.3 Data filtering and interpolation

The CMD MiniExplorer and the CMD MiniExplorer Special Edition have been factory-calibrated using the supplied handle (i.e., a crutch). Therefore, it is not necessary to perform in-field zeroing. Both devices also internally compensate for temperature changes during a survey with a stability of 0.1 mS m^{-1} per °C (GF_Instruments, 2011). Nevertheless, negative ECa values were measured as already observed in previous studies (Rudolph et al., 2015; von Hebel et al., 2014). Some studies have therefore calibrated the ECa measurements with independent electrical resistivity tomography (ERT) data (Lavoué et al., 2010; Shanahan et al., 2015) in order to obtain quantitative EMI data that allow inversion (Mester et al., 2011; von Hebel et al., 2014). Alternatively, calibration can be achieved using a metal sphere or by measuring at multiple elevations (Tan et al., 2019; Thiesson et al., 2014). Since repeated calibration is difficult to achieve for the EMI survey presented here, a correction based on a

linear regression between EMI measurements made with the sled and the supplied handle for each EMI coil configuration was applied. In this approach, it is assumed that the required calibration of each EMI coil configuration is relatively stable in time.

Since measured ECa values are rarely normally distributed (Minsley et al., 2012), an histogram-filtering technique was applied following von Hebel et al. (2014) to identify and exclude outliers. The filter divides the data into 15 bins. Bins containing <0.5% of the data were removed. Afterwards, neighboring ECa measurements that showed differences larger than 1 mS m^{-1} were removed to avoid unrealistically high lateral ECa variation. In a next step, the filtered data of each coil configuration were interpolated to a regular 1 by 1 m grid using ordinary Kriging with an exponential semivariogram. The individual interpolated surfaces for each coil configuration were merged together in a raster mosaic dataset.

3.1.1.4. Temperature correction

To standardize the EMI data to a reference temperature of 25°C, we performed a correction for soil temperature using the approach of Campbell et al. (1949).

$$EC_a^{25} = f_T EC_a^T, \quad (1)$$

where ECaT is the ECa measured at soil temperature T and f_T is a temperature correction factor given by

$$f_T = 0.4470 + 1.4034e^{-T/26.815} \quad (2)$$

as proposed by Sheets and Hendrickx (1995), corrected by Corwin and Lesch (2005) and used in many time lapse EMI studies (e.g., Robinet et al., 2018). The average soil temperature between 08:00 AM and 08:00 PM at all measurement days was obtained by averaging the measurements from three soil temperature sensors installed in field F10 at a depth of 0.5 m. The minimum soil temperature was measured on the 5th of December (4.7°C when field F50 was measured), while the highest temperature was measured on 15th of September (20.8°C when fields F38 and F39 were measured). It is important to realize that this temperature correction will not be able to overcome all differences in mean ECa between fields, since EMI data were acquired in different seasons and after different agricultural management (e.g., type of crop, timing of fertilization).

3.1.2. Classification of ECa maps

A flowchart of the classification methodology including aspects of preprocessing as well as the selection of sampling locations for ground truth data is shown in Figure 6. The following analyses were performed using ArcGIS Desktop software. The first step of the classification was to merge the EMI measurements obtained with the six coil separations in the HCP orientation. For this, a raster processing composite band tool (ESRI, 2017) was used to generate a multiband raster dataset, where HCP coils with increasing separation represent the different bands (Figure 7). It was decided not to add the VCP configurations to the multiband image because the stronger sensitivity to shallow layers resulted in higher noise and because the relatively homogeneous ploughing horizon of ~30 cm thickness resulted in relatively constant ECa values within each single field for these configurations. However, the EMI measurements in VCP mode will be used in the following to support the interpretation of the EMI data.

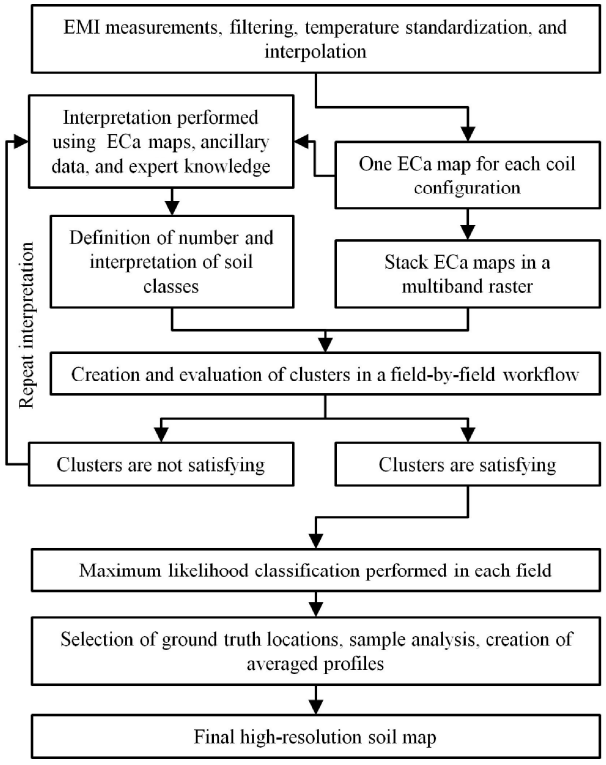

Figure 6: Flowchart of the supervised classification methodology.

To classify the multiband raster data, a supervised classification method was used. In a first step, the number of soil classes and their interpretation need to be defined. For this interpretation, information contained in the nine ECa maps, the soil map, the soil taxation map, as well as expert knowledge from previous studies and field observations were taken

into account. As a result of this interpretation process, the amount and type of soil classes is known for each field.

In a next step, the multiband raster of EMI data was used to classify the survey area field-by-field. This was necessary because EMI data were found to vary between fields due to other factors besides soil properties (see results section of this chapter for a more detailed analysis of this variability). For each field, areas belonging to a specific soil class were identified within the multiband raster data (so-called training areas). This was achieved by visualizing different combinations of EMI coil separations displayed with RGB composite colors (see Figure 7 for one possible example). After the training areas were selected for each soil class, histograms of ECa values for each class and band as well as scatter plots of ECa values for all classes for different combinations of bands were used to evaluate the distribution and separation of the classes in the six-dimensional space of the measured ECa values. When it was not possible to achieve a proper separation of the clusters (e.g. fully overlapping clusters) in all fields using the given number and interpretation of classes, then the interpretation was reviewed and the process was repeated until a proper cluster separation was achieved on all fields.

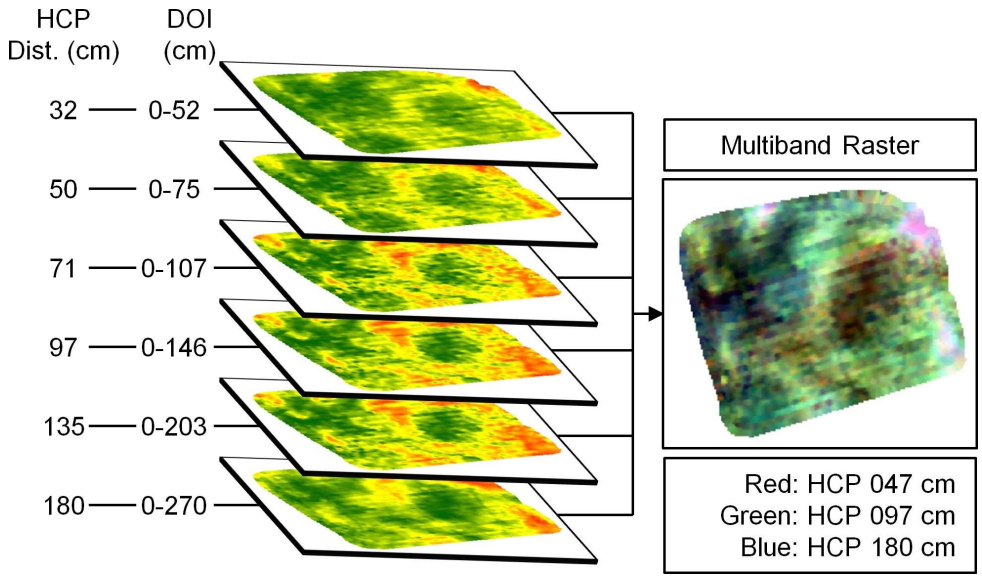

Figure 7: Multiband raster image from the ECa interpolation maps on F05. The 6 bands are the 6 coil distances in HCP configuration of the CMD Mini Explorer Special Edition.

After defining the training areas for a given field, a Maximum Likelihood classification (ESRI, 2017) was used to classify all raster cells of a field. For this, the mean and the covariance matrix of the training areas were calculated (Ball and Hall, 1965; ESRI, 2014;

Richards, 1999). Based on this, the statistical probability that a particular cell belongs to each class was calculated and the cell was assigned to the class with the highest probability. After this classification, a raster map of the field is obtained where every cell is assigned to the most probable class.

After the classification of each field, the results were merged together to obtain one classified map of the whole study area. Next, two filtering procedures were applied to remove small areas characterized by a single or few cells as well as to smooth the boundaries between different classes. First, a majority filter (ESRI, 2017) was used to replace cell values based on the value that occurs most often within the eight neighboring cells. This replacement occurred only when the number of neighboring cells from the same soil class is large enough to be the majority (e.g., 5 out of 8 cells) (ESRI, 2014). Second, a boundary clean filter (ESRI, 2017) relying on an expand-and-shrink method in order to clean the boundaries from ragged edges between different soil classes was used. A sorting based on the size of different zones represented by a single class was applied to facilitate the expansion of large zones over small ones (ESRI, 2014).

3.1.4. Soil sampling for ground truth information

Based on the final map obtained from the classification of EMI data, 100 soil augering locations were selected where soil profile descriptions and soil samples were acquired. The sampling points were distributed amongst all the soil classes and the number of points per soil class was based on the total area of the soil class itself with a minimum of three sampling locations per soil class. For each of the 100 points, a random location within the assigned class was determined. Each location was at least 2.5 m away from the boundary between two soil classes. Also, locations within the same soil class were separated by at least 150 m. In January and February 2017, all locations were visited using a DGPS system (Trimble inc., Sunnyvale, USA) and a Pürckhauer auger was used to sample and describe the soil up to a maximum depth of 2.0 m.

The maximum augering depth at each location varied considerably because of the presence of horizons with high gravel content or strong cementation. For each sampling location, a soil profile description was obtained with information on horizon type, horizon thickness, total depth, and color. To delineate horizons in the field, texture was estimated by feel (“hand texturing”) (Sponagel et al., 2005; Vos et al., 2016). For each horizon, at least one soil sample

was collected. When layers with different texture were identified in a single horizon, multiple samples were collected. All soil samples were stored in a refrigerated room until the gravimetric water content was estimated by drying the sample at a temperature of 105°C for 36 hours. The weight fraction of gravel (> 2 mm) was determined using sieving. Afterwards, the texture of each sample was analyzed with a combined sieving and pipette method using a Sedimat 4-12 apparatus (UGT, Umwelt Geräte Technik GmbH, Münchenberg, Germany).

The soil profiles of all ground truth locations within a single soil class were averaged to obtain a typical soil profile with information on horizon type, depth, texture, and gravimetric water content for that particular class. To compare different soil classes, the soil classes were ordered according to decreasing average ECa. Two tailed *t*-tests were performed between matching horizons of two adjacent soil classes to establish whether there are statistically significant differences. For this statistical analysis, the horizons Ap and AB were considered as a single horizon. The null-hypothesis of equal means in the *t*-test was rejected when the computed *t*-value was higher than the 5 % level of significance (2.5 % in each tail).

3.1.5. Comparison with satellite image

To test the potential of the geophysics-based soil map to identify areas with variable crop growth, a comparison with observed field-scale patterns in crop growth derived from remote sensing was performed. For this, we used a WorldView-2 panchromatic satellite image with 0.5 m resolution provided by DigitalGlobe within ArcGIS Basemap (ESRI, 2015). The image was collected during a drought period in July 2015 (Figure 1a). Here, a set of fields that were cropped with sugar beet in 2015 were analyzed (F05,F07, F08, F17a, F22b, F23, F24, F39, F40 and F49) since sugar beet is known to show visual signs of drought stress in this area (Rudolph et al., 2015). In each of the sugar beet fields, areas with relatively stressed crops (light green) and areas with relatively healthy crops (dark green) were manually digitized on the satellite image.

In order to quantify the correspondence between each class of the geophysics-based soil map and the crop performance derived from the satellite image, the number of cells located on stressed and healthy crops was determined for each class of the soil map for each field. If more than 50% of the cells of a soil class for a particular field were stressed crops, the soil class was assumed to correspond with stressed conditions (and vice versa). The correspondence of each soil class with the satellite image was quantified using the true

positive ratio (TPR), which is the fraction of cells correctly classified as being stressed, and the true negative ratio (TNR), which is the fraction of cells correctly classified as healthy crops. Due to these definitions, TPR and TNR can range from 50 to 100%.

3.2 Results and discussion

3.2.1. Large-scale EMI survey

The ECa maps presented in Figure 8 show that the study area can be divided in four sub-areas (Figure 8c), each with characteristic sediments and ECa values and patterns. This subdivision was performed by comparing the patterns in ECa maps (Figure 8a-f) and their general ECa values (Table 3) with the geometry of the soil map (Figure 8a) and, to a lesser degree, of the soil taxation map (Figure 8b). Here, it is assumed that the soil maps provide reliable information on the type and origin of the sediments, albeit with a low resolution because of the lower density of the ground truth information used to create the maps. Therefore, the joint interpretation of ECa maps (horizontal geometry) and soil maps (type and origin of sediments) results in a more reliable subdivision of the study area. From east to west, the following sub-areas were identified: a buried paleochannel system on the upper terrace (sub-area A in Figure 8c), a transition zone associated with a slope heading N-S (sub-area B in Figure 8c), a relatively homogeneous area in the center (sub-area C in Figure 8c), and a second heterogeneous area in the west (sub-area D in Figure 8c). In the following, the ECa maps from these four sub-areas are discussed in more detail.

Sub-area A was partly studied by Rudolph et al. (2015), and is characterized by relatively low ECa values compared to the rest of the study area (Table 3). The geometry of this sub-area agrees well with the Pleistocene loess deposits on sand and gravel described in the soil map (Figure 1b). Therefore, it is assumed that the entire sub-area A is characterized by paleochannels cut in sandy-gravel material and then filled by finer loess sediments. These paleochannels are characterized by a relatively higher ECa because of the larger thickness of the loess sediments with higher silt and clay content and higher water storage capacity (Rudolph et al., 2015). The average ECa generally increased with DOI for both VCP and HCP coil configurations (Table 3). However, the range of ECa values is relatively small, especially when compared to the rest of the study area. A geomorphological interpretation of the pattern of buried channels indicates that the stream type was an anastomosing fluvial system with multiple channels (Rosgen, 1994).

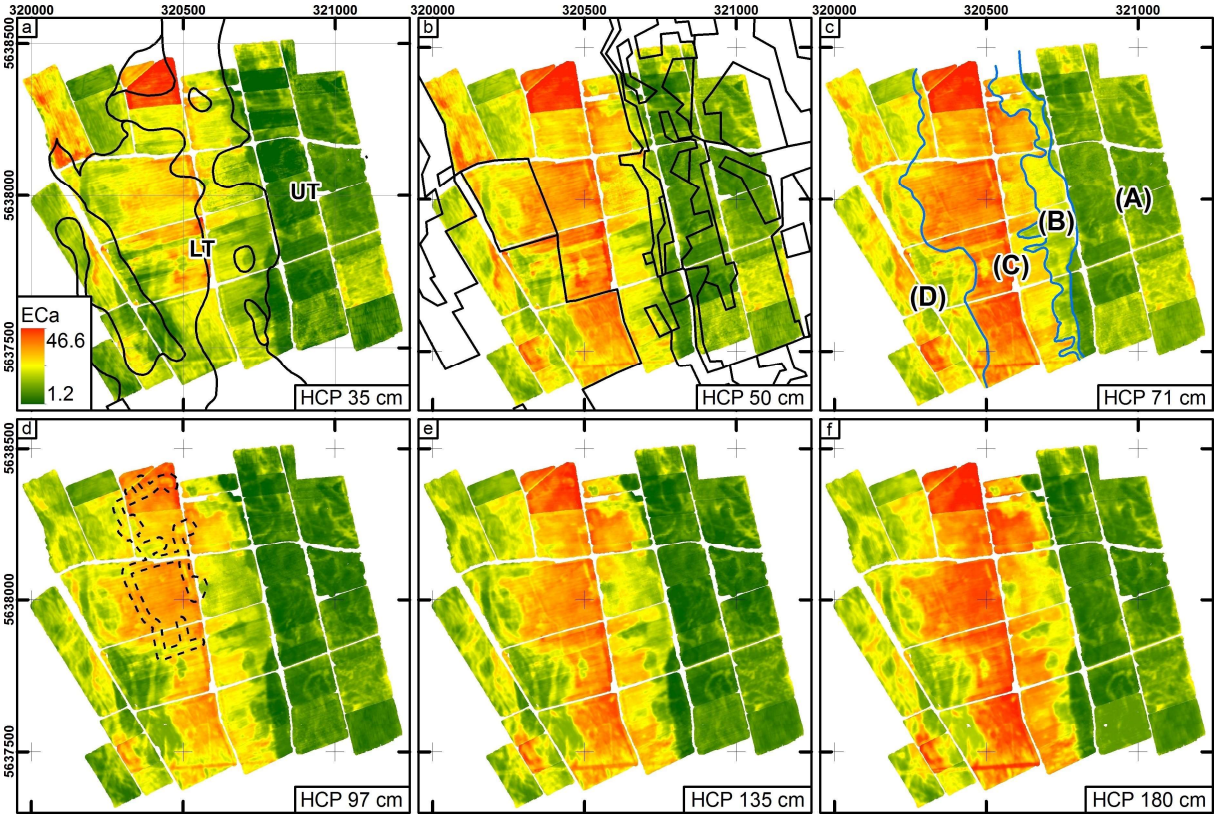

Figure 8: ECa maps of the six HCP configurations: a) HCP 35 cm with lines from the 1:5,000 soil map, b) HCP 50 cm with lines from the soil taxation map, c) HCP 71 cm with subdivision of the study area in four geomorphological sub-areas A, B, C, and D, d) HCP 97 cm with evidence of buried irrigation channels and water ponds (dashed line), e) HCP 118 cm, f) HCP 180 cm.

Table 3: Average (Avg.) and Standard deviation (σ) of the measured ECa values (mS m^{-1}) obtained with the six HCP coil configurations in the four classes of sub-area A.

	Sub-Area D		**Sub-Area C**		**Sub-Area B**		**Sub-Area A**	
Configuration	**Avg.**	**σ**	**Avg.**	**σ**	**Avg.**	**σ**	**Avg.**	**σ**
VCP 32cm	13.6	5.3	16.1	5.8	10.5	6.0	8.7	4.0
VCP 71cm	17.5	4.3	22.0	4.8	15.1	4.0	10.6	3.2
VCP 118cm	18.8	4.0	24.5	4.6	16.6	3.3	11.4	3.1
HCP 35cm	15.6	3.9	18.8	4.2	14.0	2.1	10.7	2.8
HCP 50cm	16.5	3.3	20.6	4.0	14.7	2.2	11.1	2.6
HCP 71cm	16.5	3.0	21.2	3.7	15.0	2.1	10.9	2.2
HCP 97cm	16.2	2.9	21.6	3.1	15.7	1.8	12.2	1.8
HCP 135cm	16.8	3.1	23.1	3.4	17.1	2.1	12.2	1.9
HCP 180cm	17.9	3.2	25.3	3.7	19.4	2.2	13.0	1.9

The transition zone represented by sub-area B coincides with the slope that strikes ~N-S across the study area. The morphology of the area, the soil map description (Pleistocene loess sediments), and the patterns in the ECa maps suggest the presence of Holocene slope deposits

located on Pleistocene loess sediments. In general, the ECa values increase with DOI for both VCP and HCP configurations and they are higher compared to sub-area A (Table 3). The increase of ECa with DOI is most pronounced for the deeper sensing configurations (HCP with 130 cm and 180 cm coil separation). This is probably related to the presence of fine sediments in the deeper layers compared to the shallow surface.

Within sub-area B, the EMI data consistently showed small areas of 1-2 ha with lower ECa compared to the surroundings. The shape of these areas depends on the DOI (see Figure 9a-c for DOIs of 75, 146 and 270 cm respectively) indicating that the presence of shallow structures was associated with the slope that characterizes sub-area B. The shape and the position of different structures along the slope allow a distinction between two regions with different genesis.

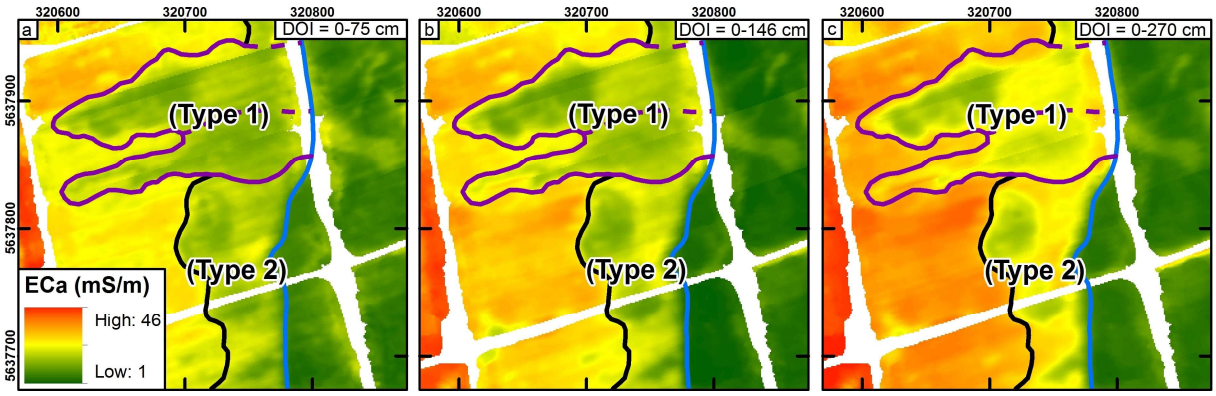

Figure 9: Shallow structures of type 1 and 2 visible along the slope in sub-area B. The interpolated ECa values are shown for a) HCP 49cm, b) HCP 97cm, and c) HCP 180cm.

The first structure (Type 1 in Figure 9a-c) was interpreted as a deposition of coarse material eroded from sub-area A when the channel system was not yet buried under aeolian sediments that led to the formation of small structures that are similar to fluvial fans. To support this interpretation, it was found that these features were adjacent to a paleochannel structure of sub-area A intersecting the boundary with sub-area B, and that the ECa pattern showed an elongated shape with low persistence with depth in their distal or proximal positions. The second structure (Type 2 in Figure 9a-c) was interpreted as a feature resulting from both natural and anthropogenic processes. First, shallow and slow movement has moved material from sub-area A to B. However, the observed feature is also related to recent anthropogenic soil management. It is known that the topography of the study area has been reshaped to facilitate agriculture with mechanized equipment (plowing, sowing and harvesting). In

addition, the area of the lower Ruhr has been inhabited and farmed for about the last 7000 yrs. Thus, soil erosion since the beginning of arable farming has also contributed to relief flattening.

The ECa values in sub-area C also showed a general increase with DOI and were relatively higher when compared to the other three sub-areas (Table 3). This area was previously described as a homogeneous lower terrace using measurements in VCP and HCP configuration with a small offset (Rudolph et al., 2015). The soil taxation map (Figure 1c) describes this area as relatively homogeneous with loamy sediments, while the soil map (Figure 1b) indicates Pleistocene loess and translocated loess. The higher ECa values in sub-area C suggest the presence of soils and sediments with higher clay content.

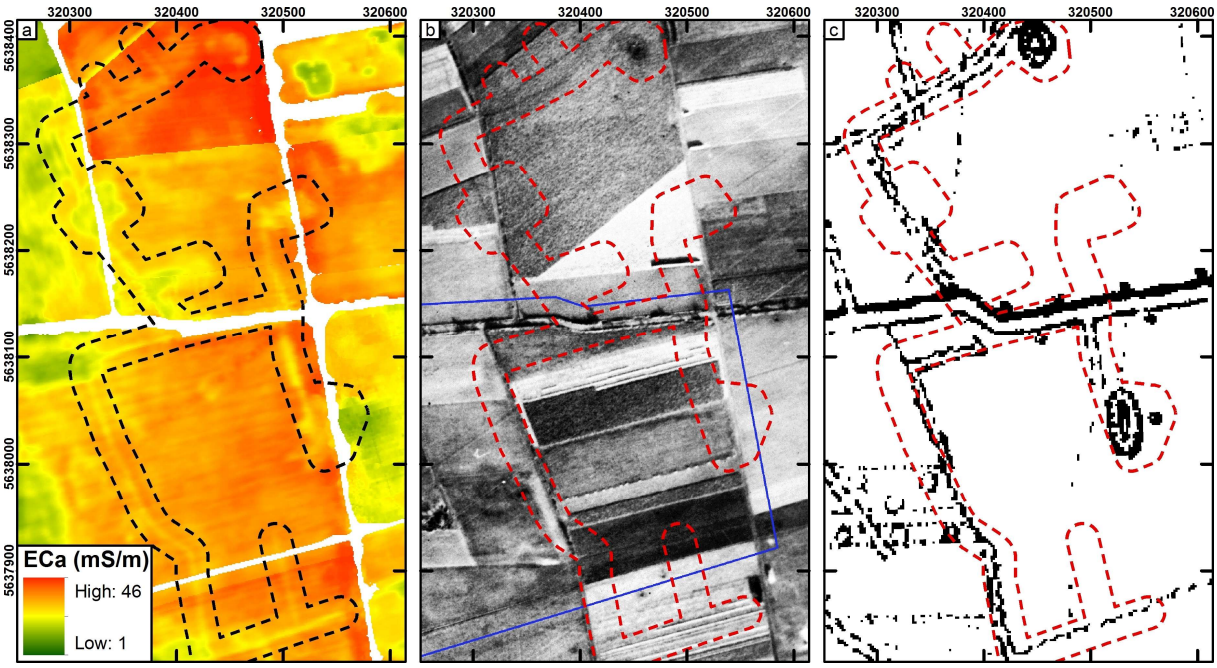

Figure 10: Geometry of anthropogenic features highlighted by a) ECa maps with HCP 97cm configuration compared with b) aerial photo from 19th November 1944 and c) historical map from 1881-1912 (NRW, 2017).

The remains of irrigation channels and water ponds are visible in the ECa maps of this sub-area (Figure 8d), and these features are shown in detail in Figure 10a. The shape of these structures is characterized by straight lines and approximately square polygons with lower ECa values compared to the surroundings. To identify the origin of these shapes, we compared the ECa map in Figure 10a with georeferenced aerial pictures and historical maps shown in Figure 10b and Figure 10c, respectively. From the aerial photo taken in November

1944 (USAAF, 1944), it can be concluded that these features were not related to defensive trench systems from WWII (Figure 10b). Instead, historical maps suggest that these structures were associated with field boundaries, irrigation channels, and water ponds and reservoirs that were active at the end of the 19th century or before (Figure 10c). Similar geometries are also visible in older maps like the Tranchot map from Napoleon times dating back to between 1801 and 1809 (map not shown). The ECa and historical maps do not perfectly match, but this could be expected given the limited precision of the older maps and the transient nature of such local water management structures.

The heterogeneous sub-area D was measured for the first time with EMI in this work. Generally, the average ECa values again increased with DOI both for the VCP and for the HCP coil configurations. The pattern visible in the ECa map (Figure 8) suggests that the subsurface of sub-area D is also characterized by a buried fluvial system and that the paleochannels are again characterized by a relatively higher ECa. However, the different geometry of the buried channels and the higher ECa values suggest a different type of fluvial activity. This is corroborated by the soil map that indicates translocated loess sediments on sand and gravels (Holocene-Pleistocene). Furthermore, the buried channels are straighter and wider compared to sub-area A. Likely, the depositional environment was closer to a braided fluvial system (Rosgen, 1994).

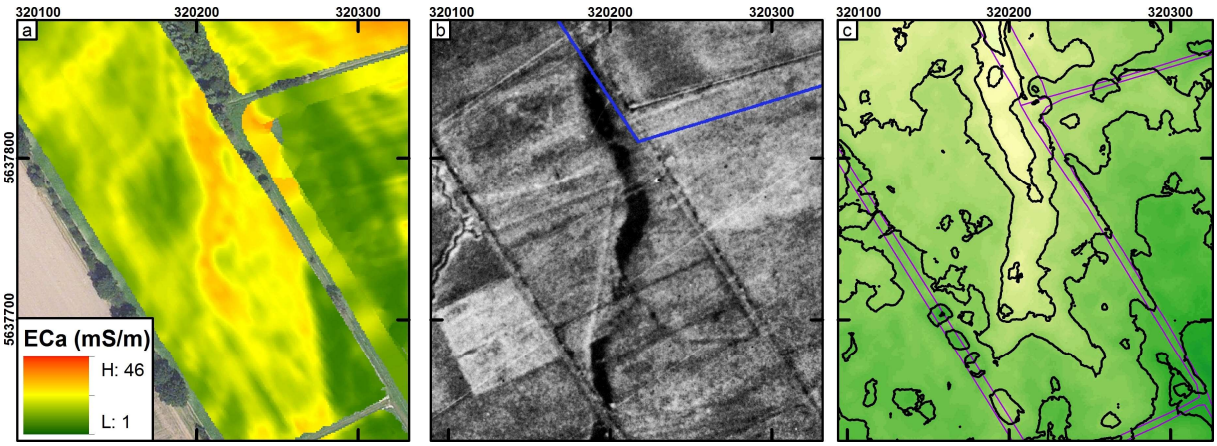

Figure 11: a) ECa maps for HCP 97 cm configuration highlighting a buried structure with a strong EMI response, b) aerial picture from 19th of November 1944 (USAAF, 1944), and c) DEM with 0.5 m spaced contour lines.

In sub-area D, more indications for recent anthropogenic activity have been identified in field F39 (Figure 11) as it is also possible to identify one channel with a strong EMI response

(Figure 11a). When comparing the EMI measurements with aerial photos from 1944 (USAAF, 1944) (Figure 11b), we identified a depression that probably corresponds to the remains of a small brook. The channel has been buried with anthropogenic sediments since 1944. The channel geometry matched with the higher ECa values obtained with EMI, and it was still apparent in the DEM where a topographic depression indicated the old position of the channel (compare Figure 11a-c).

3.2.2. Heterogeneity at the field scale

Besides the large-scale patterns in ECa values, field-scale variability in ECa values is also apparent. For example, fields F08 and field F24a-b were managed differently before the EMI data acquisition that took place on the same day (Figure 12a). Field F08 and field F24a were cropped with wheat by two different farmers, while field F24b was cropped with barley. Therefore, it is assumed that the observed differences in ECa for field F08 and field F24a-b are related to the different management that has resulted in different soil water content or different pore water conductivity at the time of data acquisition. Similarly, Figure 12b shows variations in ECa values between adjacent fields that were not measured at the same time. As in the previous case, part of the observed variation is related to differences in field management. More importantly, there are differences due to the variable amount of precipitation before data acquisition. For example, field F13b was measured in the beginning of the growing season and 53 mm of precipitation occurred in the five weeks before data acquistition. In field F43 and F06, which were measured at the end of the growing season, 44 mm and 29 mm of precipitations were recorded in the previous five weeks, which obviously affects soil water content and thus ECa values.

Although these two examples illustrate that variable management and timing of EMI data acquisition affected the ECa maps, it can be seen that the characteristics of the subsurface in terms of layering and texture are still identifiable, since a range of features that cross the field boundaries are apparent (Figure 12b). Here, it is important to emphasize that the adopted approach for ECa correction (calibration and temperature) was not expected to correct these differences in ECa between fields, since they are likely related to variations in soil water content and pore water conductivity. To overcome this secondary variability in ECa as much as possible, it was required to apply the classification methodology to each field independently.

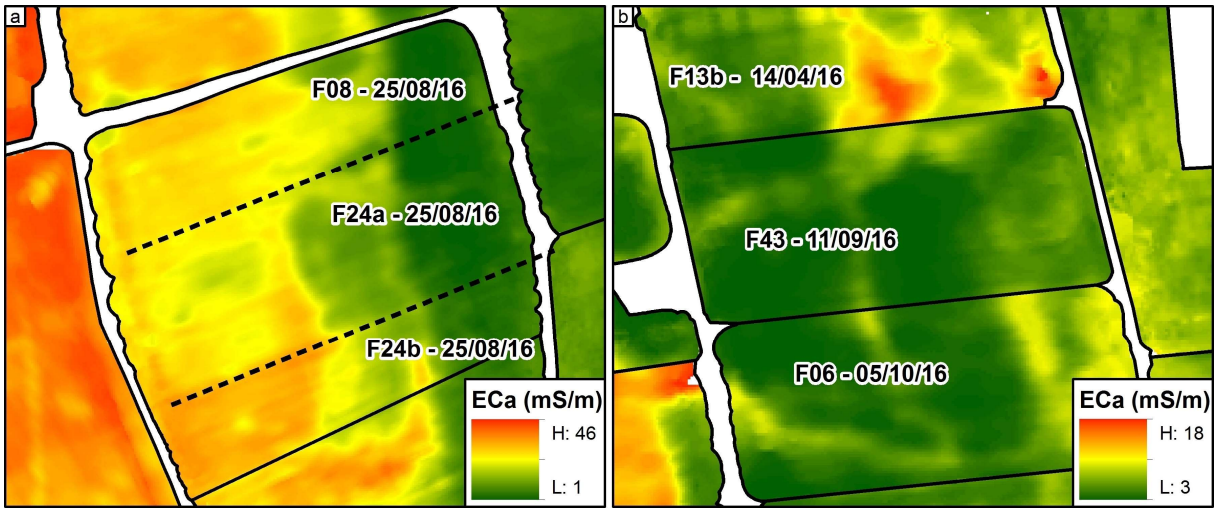

Figure 12: a) Variation in ECa between fields measured within 24h on August the 25th 2016, b) variation in ECa between fields measured at different times (measurement dates given after field abbreviation).

3.2.3. Definition of the classes

After subdividing the study area in four different sub-areas, it was assumed that the soils in each sub-area are different because of the different type and age of the sediments. Further subdivision within each sub-area was performed prior to the classification of each field. In sub-area A, the best distribution and separation of the clusters in the six-dimensional space provided by the EMI data in the multiband raster was achieved by using four soil classes, which are named A1a, A1b, A1c, and A1d in the following. These soil classes showed a general decrease in ECa from class A1a to A1d (Table 4). In sub-area B, an appropriate separation of clusters was obtained using a total of five soil classes divided in two groups: two soil classes representing natural soils (B1a and B1b) and three representing anthropogenic soils (B2a, B2b, and B2c). Generally, ECa was higher in natural soils compared to anthropogenic soils (Table 5). Moreover, ECa decreased from soil class B1a to B1b and from soil class B2a to B2c (Table 5). In sub-area C, a clear subdivision can be made between anthropogenic soils (Figure 8d) and the surrounding natural soils. The anthropogenic soils were divided in buried irrigation channels (class C2a) and buried water ponds (class C2b in Table 6). These soil classes were manually determined in the multiband raster because of their evident geometry (Figure 8d and Figure 10a) and subsequently removed from the multiband image to avoid any influence in the classification process. The remaining area of sub-area C is apparently homogeneous according to the 1:5000 soil map and the soil taxation map (Figure 1b-c). However, the range of ECa (e.g., from 9.2 to 35.1 mS m^{-1} in HCP 35 cm and from 13.8 to 34.2 mS m^{-1} in HCP 180 cm) suggested further subdivision and the use of two soil classes C1a and C1b with different ECa (Table 6). In sub-area D, the best distribution and separation

of clusters was provided by using five soil classes. The four soil classes D1a, D1b, D1c, and D1d represent natural soils, and soil class D2a represents an anthropogenic structure in field F39. The ECa of soil class D2a was highest, then the ECa decreased from soil class D1a to D1d (Table 7).

3.2.4 Classified ECa map

Using these classes, the multiband ECa image of each field was classified. This resulted in a high resolution soil map composed of four sub-areas divided in a total of 18 soil classes. In the following, the results for each sub-area are presented separately to facilitate the description and the understanding of the high resolution geophysics-based soil map obtained by combining the classification results with the ground truth sampling.

3.2.4.1. Classified ECa map of sub-area A

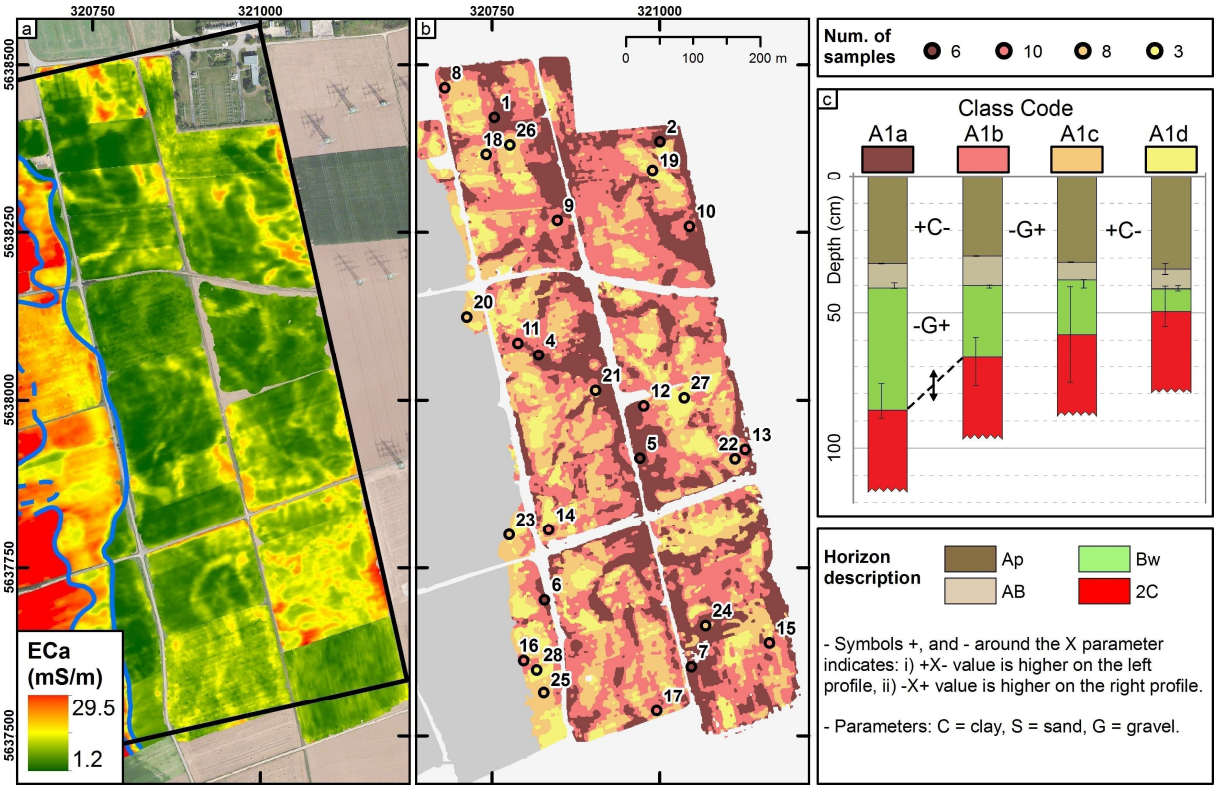

Figure 13: a) ECa map of the HCP 97 cm configuration in sub-area A, b) classified ECa map of sub-area A with the locations of the ground truth points, c) averaged soil profiles for each of the four classes with a description of the statistically significant differences in texture and layers depth between classes A1a-A1b, A1b-A1c, and A1c-A1d. Note that the ECa scale for panel a) differs from the one in Figure 8 to improve visualization.

The results of the supervised classification of sub-area A are shown in Figure 13b while the average soil profiles of each soil class are shown in Figure 13c. The soil profiles of each soil class are richer in fine sediments (clay and silt) in the Ap-AB, and Bw horizons characterized by Aeolian sediments. The deeper horizons consisted of coarser sediments composed of Pleistocene sand and gravels. The average ECa for each configuration decreased from soil class A1a to class A1d (Table 4). This may be due to the decreasing maximum depth of the Bw horizon that consists of finer sediments (Figure 13c). A pairwise *t*-test between neighboring soil classes indicated that this maximum depth was significantly different only between classes A1a and A1b (p = 0.040). However, the textural data showed a significant difference (p = 0.031) in gravel content between the Ap-AB horizon of soil class A1b (16.7 %) and A1c (29.8 %). In addition, the clay content of the AP-AB horizon in class A1c (14.4 %) was significantly higher (p = 0.034) than that of class A1d (12.9 %). These textural characteristics are in agreement with the decreasing average ECa from soil class A1b to A1d. The average texture of all soil profiles for sub-area A-D and the results of all pairwise *t*-tests within each sub-area are provided in the supplementary material S.1.

Table 4: Average (Avg.) and Standard deviation (σ) of the measured ECa values (mS m^{-1}) obtained with the six HCP coil configurations in the four classes of sub-area A.

	A1a		**A1b**		**A1c**		**A1d**	
Configuration	**Avg.**	**σ**	**Avg.**	**σ**	**Avg.**	**σ**	**Avg.**	**σ**
HCP 035	12.5	2.9	10.8	2.3	9.6	2.3	8.3	1.9
HCP 050	12.9	2.5	11.1	2.1	10.0	1.9	8.6	1.5
HCP 071	12.5	2.2	10.9	1.6	10.0	1.6	8.8	1.3
HCP 097	12.7	1.8	11.1	1.3	10.3	1.3	9.4	1.1
HCP 130	12.7	1.8	11.1	1.4	10.3	1.3	9.9	1.2
HCP 180	13.6	1.9	11.8	1.3	11.1	1.3	10.8	1.2

3.2.4.2. Classified ECa map of sub-area B

The results of the supervised classification of sub-area B are shown in Figure 14Figure 14: a) ECa map of the HCP 97 cm configuration in sub-area B, b) classified ECa map of sub-area B with the locations of the ground truth points, c-d) averaged soil profiles for each of the four classes with a description of the statistically significant differences in texture between classes B1a-B1b, B2a-B2b, and B2b-B2c.b and the average soil profiles are shown in Figure 14c-d. Compared to sub-area A, the soil profiles in this sub-area generally have a Bg horizon below the Bw horizon. Moreover, the 2C horizon consisting of coarse sediments that is common in

sub-area A was found only in one of the five soil classes of sub-area B. An Ap-AB horizon was always found on top of each profile.

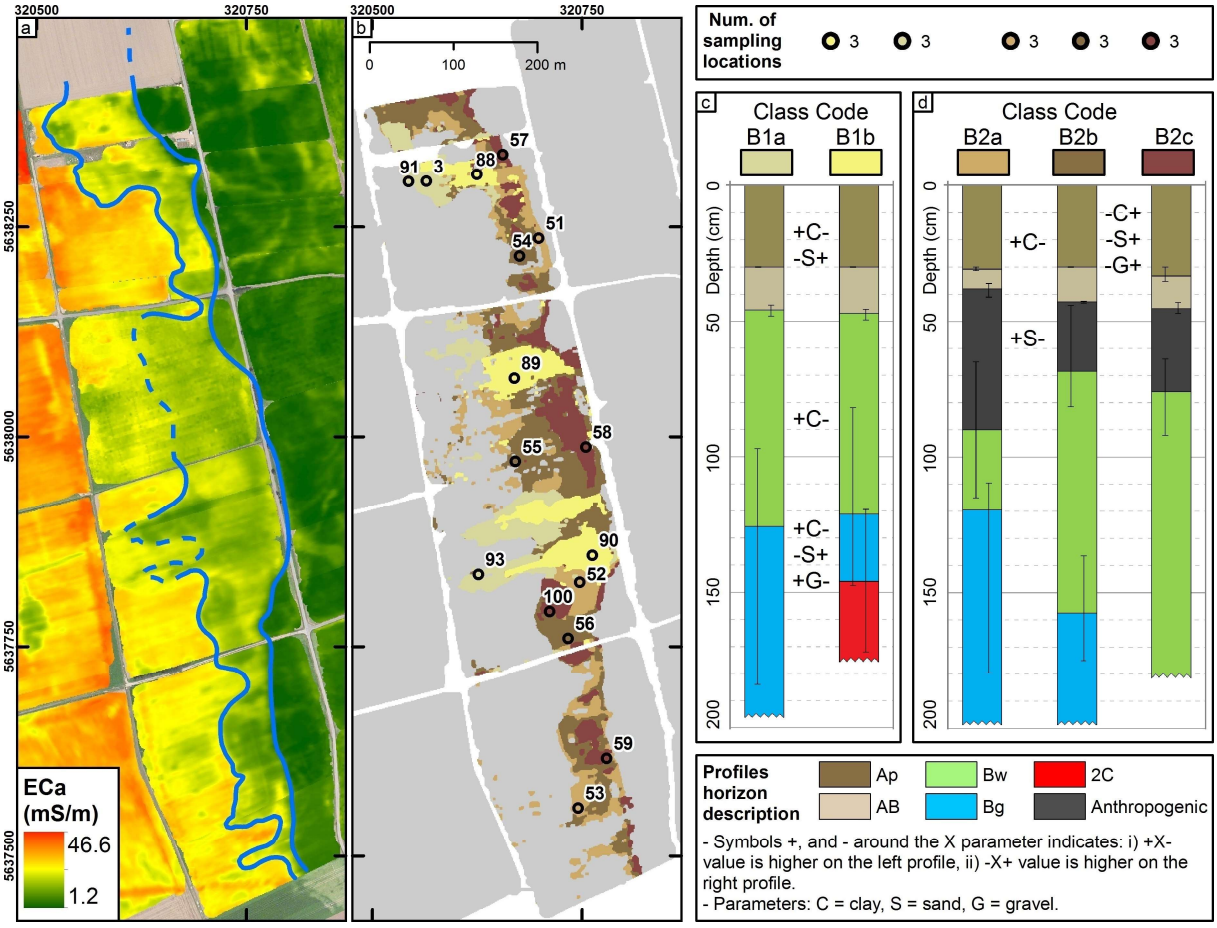

Figure 14: a) ECa map of the HCP 97 cm configuration in sub-area B, b) classified ECa map of sub-area B with the locations of the ground truth points, c-d) averaged soil profiles for each of the four classes with a description of the statistically significant differences in texture between classes B1a-B1b, B2a-B2b, and B2b-B2c.

Table 5 shows that the average ECa is higher in soil class B1a compared to B1b. Together with the presence of the 2C horizon in soil class B1b, this suggests that B1b represents areas in which the 2C horizon, typical of sub-area A, is present below slope deposits. Although there were no significant differences in horizon depth between class B1a and B1b, we did observe significant differences in texture as indicated in Figure 14c. The most evident was the higher clay content of the Ap-AB, Bw, and Bg horizons of class B1a (15.9 %, 17.3 %, and 22.5 % compared to 12.3 %, 16.4 % and 18.1 % with $p = 0.005$, $p = 0.006$, and $p = 0.002$). In addition, the sand content of the Ap-AB and Bg horizons of class B1a was lower than in B1b (15.1%, and 12.8 % compared to 19.2 %, and 17.8 % with $p = 0.002$, and $p = 0.012$). Again, these textural differences are consistent with observed differences in ECa. In contrast with the

decrease in average ECa, the gravel content of the Bg horizon of soil class B1a was significantly higher than that of class B1b (12.8 % compared to 1.6 %, $p = 0.014$). However, we assume that this difference in gravel content is secondary given the aforementioned differences in textural characteristics and layering of these two classes.

Table 5: Average (Avg.) and Standard deviation (σ) of the measured ECa values (mS m^{-1}) obtained with the six HCP coil configurations in the four classes of sub-area B.

	B1b		**B1a**		**B2a**		**B2b**		**B2c**	
Configuration	**Mean**	**σ**	**Mean**	**σ**	**Mean**	**σ**	**Mean**	**σ**	**Mean**	**σ**
HCP 035	16.1	2.0	13.3	1.6	14.7	2.5	14.3	2.5	12.6	2.0
HCP 050	16.9	2.2	14.2	1.9	15.5	2.4	14.9	2.2	13.2	2.1
HCP 071	17.2	1.9	14.6	1.8	15.8	2.1	15.2	2.1	13.4	1.9
HCP 097	17.7	1.6	15.4	1.0	16.6	1.7	15.8	1.7	14.0	1.5
HCP 130	19.4	1.7	17.0	1.3	18.0	2.1	17.3	2.3	15.1	1.9
HCP 180	21.7	1.9	19.5	1.3	20.2	2.2	19.5	2.4	17.0	2.1

Soil classes B2a, B2b, and B2c are characterized by anthropogenic deposits in the first ~70-90 cm of the profile. The profiles of classes B2a and B2b are relatively similar, and no significant differences were found in horizon depth. Again, the texture showed meaningful differences. The clay content of the Ap-AB horizon of class B2a was significantly higher than that of B2b (15.1 % compared to 12.0 %, $p = 0.002$). Even though the anthropogenic horizon of soil class B2b showed a significantly higher sand content (19.7 % compared to 15.1 %, $p = 0.020$), the profile and texture were considered to be consistent with the higher average ECa of class B2a. The profile of soil class B2c is the only one without a Bg horizon. At the same time, the Ap-AB horizon of this class is characterized by a significantly higher gravel content compared to class B2b (24.3 % in class B2c compared to 3.5 %, $p = 0.001$). Furthermore, the sand content of the Ap-AB horizon is significantly higher in soil class B2c (21.7 % compared to 17.1 %, $p = 0.010$). This is in agreement with the lower average ECa in class B2c compared to class B2b and apparently compensates the significantly higher clay content of horizon Ap-AB of class B2c (14.9 % in class B2c compared to 12.0 % in class B2b, $p = 0.006$). Note that each of these anthropogenic soil classes was characterized using only three ground truth sampling locations, so that the provided interpretation should be considered with some caution.

3.2.4.3. Classified ECa map of sub-area C

The results of the supervised classification of sub-area C are shown in Figure 15b and the average profiles of the four soil classes are shown in Figure 15c-d. The profiles in this sub-area are relatively simple. A Bg horizon is consistently present below a Bw horizon and an Ap-AB horizon is always found on top of each profile.

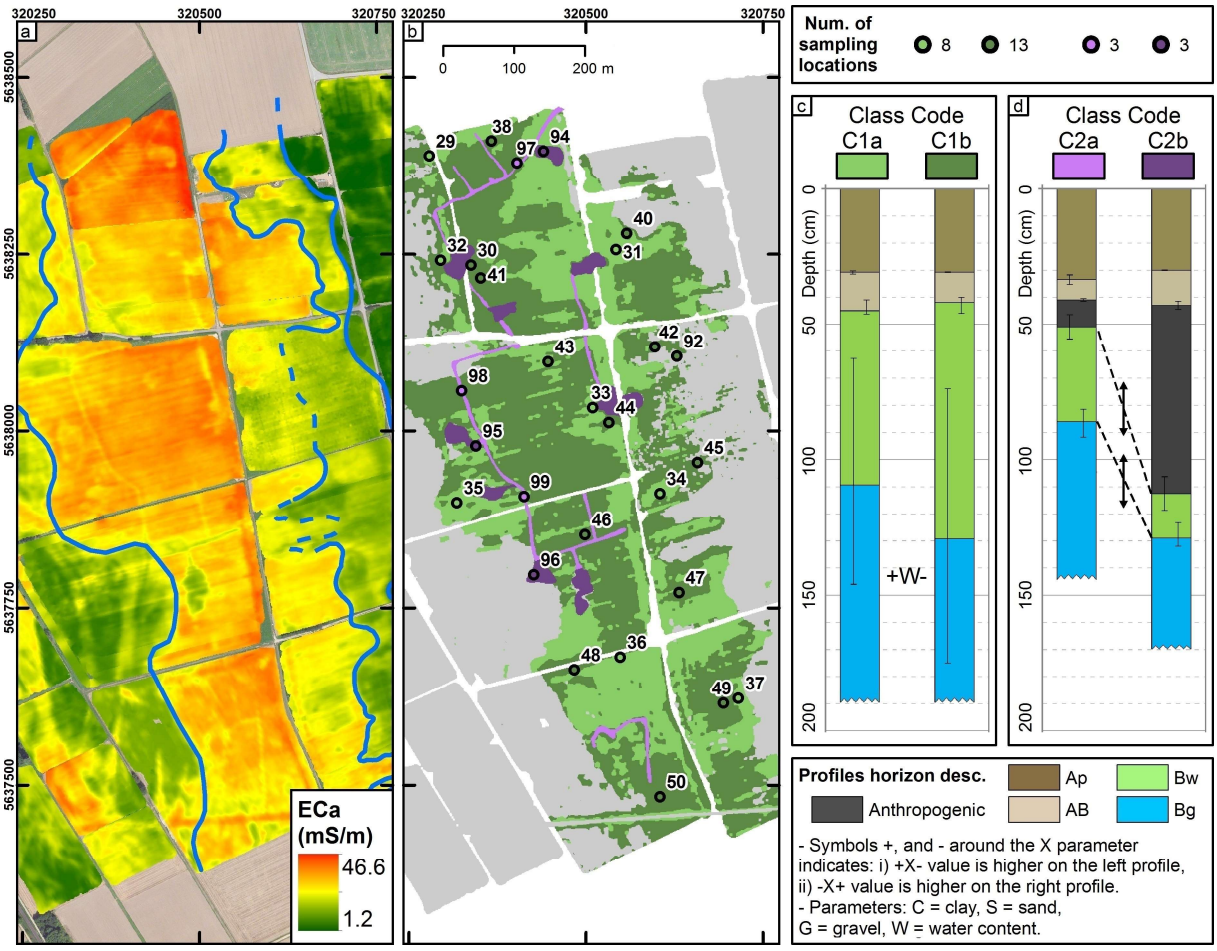

Figure 15: a) ECa map of the HCP 97 cm configuration in sub-area C, b) classified ECa map of sub-area C with the locations of the ground truth points, c-d) averaged soil profiles for each of the four classes with a description of the statistically significant differences in texture and layers depth between classes C1a-C1b and C2a-C2b.

The two soil classes associated with natural deposits (C1a and C1b) did not show significant differences in the horizon depths, and also no significant differences in texture were found. This could be expected considering the subtle differences in ECa between the two classes (Table 6). However, a significant difference in gravimetric water content was found for the Bg horizons. The gravimetric water content was significantly higher in soil class C1a (16.0 % compared to 14.1 %, p = 0.021), which is in agreement with the higher average ECa for this

class, and this may be related to differences in bulk density at depths. Nevertheless, these two classes are considered to be similar and could be merged according to the ground truth information.

Table 6: Average (Avg.) and Standard deviation (σ) of the measured ECa values (mS m^{-1}) obtained with the six HCP coil configurations in the four classes of sub-area C.

	C1a		C1b		C2a		C2b	
Configuration	**Mean**	**σ**	**Mean**	**σ**	**Mean**	**σ**	**Mean**	**σ**
HCP 035	20.0	4.0	18.3	3.8	19.6	4.9	19.0	4.0
HCP 050	22.1	3.8	20.1	3.4	21.5	3.9	19.9	3.7
HCP 071	22.7	3.6	20.8	3.1	21.6	3.3	19.8	3.4
HCP 097	22.9	2.8	21.3	2.7	21.3	2.7	19.9	3.4
HCP 130	24.5	3.1	22.8	2.8	22.8	2.9	20.7	3.2
HCP 180	26.8	3.3	25.2	3.0	25.1	3.3	22.7	4.0

For the anthropogenic soil classes (C2a and C2b), the soil profiles differ in the thickness and thus the maximum depth of the anthropogenic horizon and the depth of the Bg horizon. The anthropogenic horizon extends to 112.5 cm in C2b compared to a mean depth of 51.0 cm in C2a (p = 0.036). In addition, the top of the Bg horizon is 129.0 cm in C2b compared to 86.0 cm in C2a (p = 0.034). This is in agreement with the interpretation of anthropogenic fillings of old irrigation networks (class C2a) and water ponds (class C2b).

3.2.4.4. Classified ECa map of sub-area D

The results of the supervised classification of sub-area D are shown in Figure 16b, while the average profiles of each soil class are shown in Figure 16c and Table 7 provides the average ECa values and the standard deviation for each of the four soil classes. The soil profile of each soil class is characterized by finer sediments in the top horizons (Ap-AB, Bw, and Bg) above a coarser 2C horizon. Another anthropogenic soil class with an Ap-AB horizon over an anthropogenic layer is also present in this sub-area.

The four soil classes D1a-d showed similar horizon types. An Ap-AB horizon was found over Bw and Bg horizons with variable thickness followed by a coarser 2C horizon. Similar to sub-area A, the decrease in depth to the coarse 2C horizon corresponds with a decrease in average ECa going from class D1a to class D1d (Table 7). The difference in depth to the 2C horizon are statistically significant between classes D1b and D1c (122.7 cm in class D1b and 83.3 cm

in class D1c, p = 0.034). This difference was not statistically different between classes D1a and D1b, but the textural analysis revealed a significant difference in gravel content of the Ap-AB horizon (higher in class D1b with 4.3 % compared to 0.9 %, p = 0.044) and in sand content of the Bw horizon (again higher in class D1b with 17.8 % compared to 14.5 %, p = 0.030). The difference in depth was also not statistically significant between soil classes D1c and D1d. However, the clay content of the Ap-AB horizon of soil class D1c was significantly higher than that of class D1d (17.2 % compared to 15.0 %, p = 0.030). These observed differences in texture are in agreement with the decrease in average ECa from class D1a to D1d.

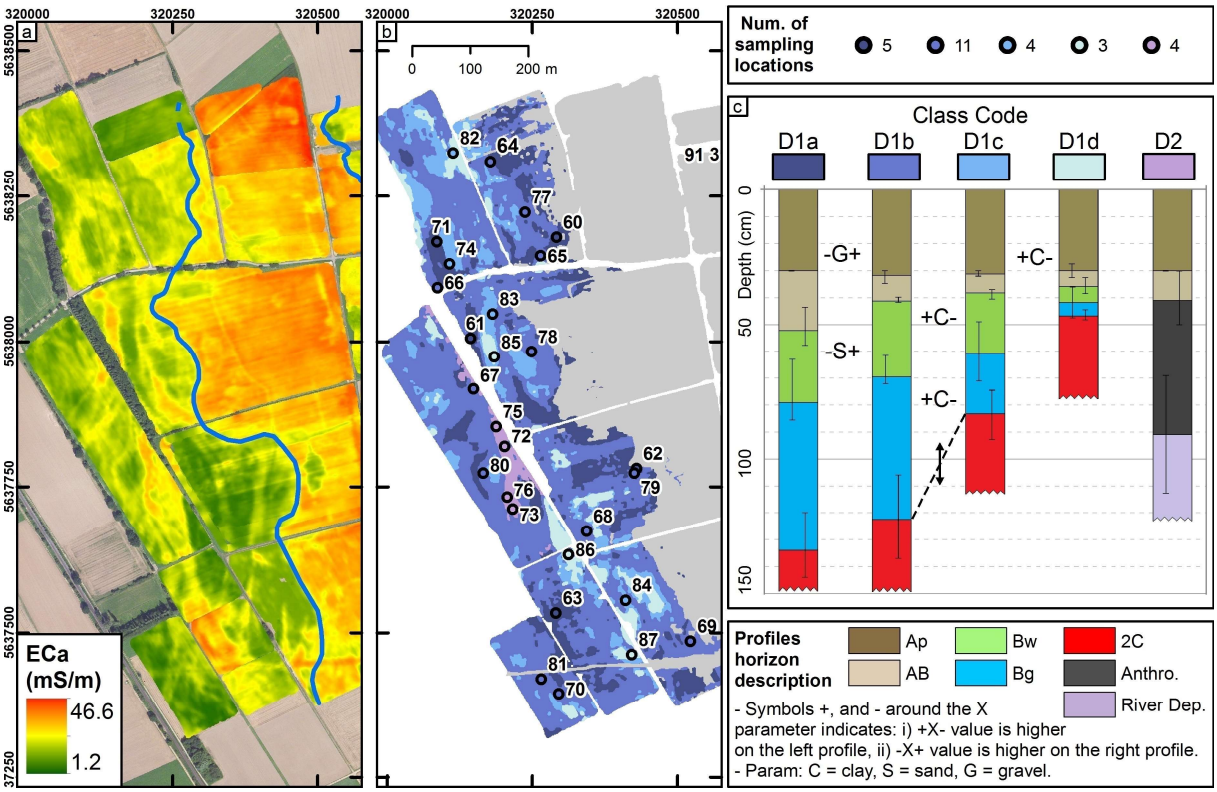

Figure 16: a) ECa map of the HCP 97 cm configuration in sub-area D, b) classified ECa map of sub-area D with the locations of the ground truth points, c) averaged soil profiles for each of the four classes with a description of the statistically significant differences in texture and layers depth between classes D1a-D1b, D1b-D1c, and D1c-D1d.

Soil class D2 showed an anthropogenic horizon over coarser sediments in all four ground truth locations. No other horizon type (e.g., Bw, Bg, or 2C) was found in these four profiles. The coarse horizon at the bottom of the four profiles was different from the 2C horizon of the other classes of sub-area D. This was confirmed by differences in the color of the sediments, the shape of the gravels, and the generally higher clay, and water content compared to the 2C

horizon of the other soil classes. This soil class was interpreted as the remains of a small brook that was recently buried with anthropogenic filling.

Table 7: Average (Avg.) and Standard deviation (σ) of the measured ECa values (mS m^{-1}) obtained with the six HCP coil configurations in the four classes of sub-area D.

	D1a		**D1b**		**D1c**		D1d		D2a	
Configuration	**Mean**	**σ**	**Mean**	**σ**	**Mean**	**σ**	**Mean**	**σ**	**Mean**	**σ**
HCP 035	17.4	3.0	15.7	3.6	12.3	2.1	11.1	2.1	21.0	1.9
HCP 050	18.8	2.8	16.4	2.7	13.5	1.5	13.7	1.3	21.6	1.9
HCP 071	19.0	2.7	16.4	2.4	13.7	1.4	12.6	1.3	20.8	1.4
HCP 097	19.0	2.6	16.2	2.4	13.9	1.6	12.7	1.4	20.3	1.8
HCP 130	19.7	2.8	16.6	2.3	14.0	1.2	13.1	1.4	19.8	1.9
HCP 180	20.8	3.0	17.8	2.5	15.1	1.3	14.5	1.5	20.2	1.9

3.2.5. Comparison with patterns in crop stress

In order to verify the ability of the high-resolution geophysics-based soil map to represent agronomically relevant processes, it was compared to patterns in crop stress in sugar beet obtained from satellite imagery (Figure 17). This comparison focused on approximately one fourth of the study area (25.5 ha) covered with sugar beet and considered fields from all four sub-areas.

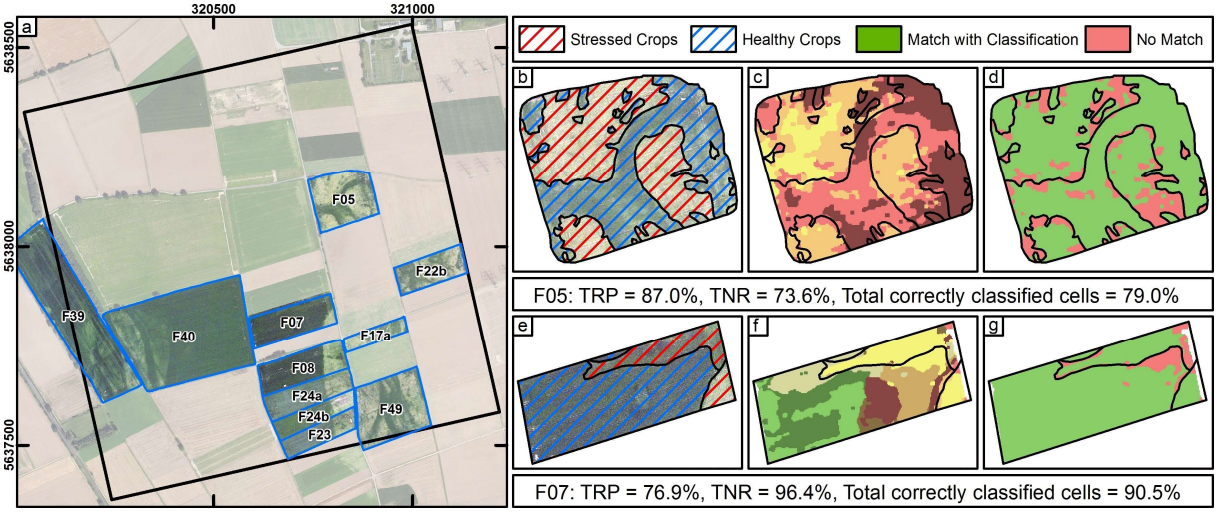

Figure 17: a) Satellite image (ESRI, 2015) of the study area with highlights on the fields cropped with sugar beet, b) digitized patterns in crop stress in F05 (F07 shown in e), c) comparison between classified map and patterns in crop stress on F05 (F07 shown in f), d) correctly classified cells (green) and incorrectly classified one (red) on F05 (F07 shown in g).

Figure 17 shows the patterns in crop stress determined for field F05 (Figure 17b) and field F07 (Figure 17e). It can be seen that these patterns match well with the geophysics-based soil map for both fields (Figure 17c and Figure 17f), and the match is visualized in Figure 17d and Figure 17g, where green cells indicate correctly classified cells and red cells indicate incorrectly classified ones. To quantify the match between the soil map and the patterns in crop stress, the TPR and TNR were first calculated for each class and then aggregated to the field-scale using weighted averaging (Table 8). The TPR represents the percentage of cells that are correctly classified as stressed crops, and ranged from 60.2 to 93.5% for the investigated fields. The weighted average for the study area was 77.9%. The TNR represents the percentage of cells that are correctly classified as healthy crops, and ranged from 62.7 to 97.1% with a weighted average of 89.0% for the study area.

Table 8: True positive ratios (TPR), true negative ratios (TNR), and total percentage of correctly classified cells (TOT) resulting from the comparison with satellite image.

Field or area	TPR (%)	TNR (%)	TOT (%)
F05	87.0	73.6	79.0
F07	76.9	96.4	90.5
F08	93.5	97.1	96.6
F17a	89.6	62.7	70.4
F22b	74.0	77.4	76.2
F23	90.1	95.7	94.5
F24	91.0	96.1	95.2
F39	64.8	92.1	91.0
F40	60.2	89.0	88.1
F49	67.7	75.7	72.5
Sub-area A	80.4	73.6	76.6
Sub-area B	73.1	95.2	92.0
Sub-area C	ND	100.0	100.0
Sub-area D	62.7	84.6	83.3
1 x 1 km	77.9	89.0	87.2

In sub-area A, the TPR is 80.4%, the TNR is 73.6%, and the weighted average is 76.6% (Table 8). The result of the classification in this sub-area is satisfying with a high accuracy in the classification of areas with stressed crops (soil classes A1c-d). In sub-area B, only soil class B1b corresponded to stressed crops and the TPR is 73.1%. All other soil classes corresponded to healthy crops, and the TNR was 95.2%. However, this high TNR is affected by the large area of healthy crops (85%) in this sub-area. Sub-area C is entirely covered with healthy plants. Consequently, it has no TPR and a TNR of 100%. In sub-area D, the TPR is

62.7%, the TNR is 84.6%, and the weighted average is 83.3%. Similar to sub-area B, is mostly covered with healthy crops (~85%, soil classes D1a-c and D2a), resulting in a high TNR. In this sub-area, the relatively poor TPR is most probably connected with the conditions in which field F40 was measured (under heavy rain, the 20th and 21st of October 2016).

Overall, the correspondence between the high-resolution soil map and the satellite image was found to be satisfying, also because the geometry of the areas in which crops are experiencing water stress during drought periods was identified to a reasonable degree.

3.3. Conclusions

In this chapter, multi-configuration EMI measurements acquired over a period of several months were combined with ground truth data to obtain a high-resolution geophysics-based soil map of a 1 x 1 km area. A supervised classification approach commonly used for the interpretation of multi-band remote sensing data was adopted to classify the ECa measurements into areas with similar soil properties. In particular, the study area was first divided in four sub-areas based on geophysical data and on information of available soil maps. In a second step, these four sub-areas were further divided in a total of 18 soil classes using a field-by-field analysis. It is clear that the results of such supervised classification depend to some extent on the interpreter, as is the case for many soil maps. Nevertheless, it was found that this approach was most suited to obtain soil information from the EMI measurements in the presence of additional variation due to variable water content and pore water conductivity. Future research could explore the benefit of advanced unsupervised classification methodologies to obtain a more objective approach. This will be discussed in more detail in Chapter 6.

In a next step, 100 locations where selected to obtain layering information and textural characteristics. The profiles located within each class were averaged to obtain typical soil profiles for each soil class. It was found that there were statistically significant differences between the soil profiles of different classes in terms of layering and texture, and that the observed differences were in agreement with the variation of average ECa between different classes. Finally, the geophysics-based soil map was compared with patterns in crop stress obtained from a satellite image and it was found that areas with stressed crops matched well with particular soil types.

Overall, the high-resolution soil map obtained from a combination of multi-configuration EMI measurements and ground truth data was found to be useful for defining zones that require variable management within precision agriculture applications. For example, this map could be used as input for fertilization and irrigation equipment that are capable of changing rates on individual sprinklers during operation. In addition, this geophysics-based soil map may be useful as input for agro-ecological model applications to predict crop stress as a function of environmental boundary conditions (soil, water availability, crop type). This will be explored in detail in Chapter 4.

Chapter 4

Simulation of spatial variability of crop LAI and yield using agro-ecosystem models and geophysics-based quantitative soil information

In this chapter*, it will be shown that the geophysics-based soil map developed in Chapter 3 allows for precise agro-ecosystem simulations of multiple crops. First, the agro-ecosystem model AgroC that is used within this thesis will be described. Then, it will be described how soil hydraulic parameters were calculated from texture and bulk density provided by the geophysics-based soil map using the pedotransfer function from Rawls and Brakensiek (1985). In order to evaluate the spatially distributed AgroC simulations, simulations of water content will be compared to measured water contents at two different locations in a first step. In a following step, the agro-ecosystem simulations for corn, potato, sugar beet, winter barley, winter rapeseed, and winter wheat will be described. It will be shown that the magnitude of simulated water stress is a function of both the crop type and the soil characteristics. In order to further validate the agro-ecosystem simulations and the impact of simulated water stress on LAI and crop performance, six LAI_{NDVI} maps were produced from RapidEye satellite images. It will be shown that the simulated LAI was generally consistent with the observed LAI_{NDVI},

* This chapter is adapted from a journal article in preparation:
Brogi, C., Huisman, J. A., Herbst, M., Weihermüller, L., Klosterhalfen, A., Montzka, C., Vereecken, H., Simulation of spatial variability of crop LAI and yield using agro-ecosystem models and geophysics-based quantitative soil information

and that the simulated productivity at harvest of four crops matched well with the actual harvest or corresponded to literature values. Finally, maps of simulated productivity at harvest will be presented for the four main crops, and the potential of these maps in practical agricultural applications will be discussed.

4.1. The AgroC model

AgroC is an agro-ecosystem model that couples: i) the SOILCO2 module (Šimůnek and Suarez, 1993; Šimůnek et al., 1996) for simulating vertical water, heat, and CO2 fluxes in a soil column, ii) the RothC module for simulating the turnover of organic carbon (Coleman and Jenkinson, 1996), and iii) the SUCROS module for simulating crop growth and organ-specific dry matter accumulation in crops (Spitters et al., 1989). The AgroC model is described in detail in (Klosterhalfen et al., 2017). In the following, a short overview of the key model components relevant for this work is provided.

The SOILCO2 module solves the one-dimensional Richard's equation that describes water flow in a given soil profile:

$$\frac{\partial \theta_w}{\partial t} = \frac{\partial}{\partial z}\left[K\left(\frac{\partial h}{\partial z} - 1\right)\right] - Q \quad (3)$$

where h (cm) is the pressure head, θ_w (cm^3 cm^{-3}) is the volumetric water content, K (cm h^{-1}) is the hydraulic conductivity, t is time (hours), z is the vertical coordinate (cm), and Q (cm^3 cm^{-3} h^{-1}) is the source/sink term accounting for water uptake by plant roots. The water retention and the unsaturated hydraulic properties as a function of pressure head are described by the Mualem- van Genuchten (Van Genuchten, 1980) model:

$$\theta_w(h) = \theta_r + \frac{\theta_s - \theta_r}{(1+|\alpha h|^n)^m} \quad (4)$$

and

$$K(h) = K_s S_e^{1/2}\left[1 - \left(1 - S_e^{1/m}\right)^m\right]^2 \quad (5)$$

where θ_r and θ_s ($cm^3\ cm^{-3}$) are the residual and saturated water content, respectively, K_s is the saturated hydraulic conductivity ($cm\ h^{-1}$), S_e is the relative saturation (dimensionless), α is the inverse of the air entry pressure (cm^{-1}), n is a dimensionless parameter related to the pore size distribution, and the parameter m is set equal to $1\text{-}1\ n^{-1}$.

In the SUCROS module, potential evapotranspiration of a crop $ET_{p,crop}$ growing under optimal conditions is calculated by multiplying the potential grass reference evapotranspiration with a crop-specific coefficient K_c. Here, the potential grass reference evapotranspiration is calculated from meteorological data using the Penmann-Monteith approach (Allen et al., 1998). The value of the K_c coefficient varies throughout the growing season and is affected by climatic conditions and crop development stage (DVS). Then, $ET_{p,crop}$ is split into potential soil evaporation E_p ($cm\ h^{-1}$) and potential transpiration T_p ($cm\ h^{-1}$) according to the Beer's law:

$$E_p = ET_{p,crop}\exp(-0.6 * LAI) \quad (6)$$

$$T_p = ET_{p,crop} - E_p - E_i \quad (7)$$

where LAI is the leaf area index and E_i ($cm\ h^{-1}$) is the water removed by evaporation of intercepted rainfall calculated using:

$$E_i = (ET_{p,crop} - E_p)\frac{C_i}{S_i} \quad (8)$$

where C_i (cm) is the interception storage at a specific time step and S_i (cm) is the canopy interception storage capacity that is assumed to be proportional to the LAI.

The potential root water uptake S_p ($cm^3\ cm^{-3}\ h^{-1}$) is a function of the potential transpiration T_p over depth z according to relative root density distribution. Actual root water uptake is calculated from the potential root water uptake using:

$$Q(z,h) = \varphi(h)S_p(z) \quad (9)$$

where φ(-) is a root water uptake stress factor that reduces the potential root water uptake in dry and wet soil conditions. This reduction factor is calculated according to (Feddes et al., 1978):

$$\varphi(h)\begin{cases}\frac{h_0-h}{h_0-h_1} & h_0 \le h \le h_1\\ 1 & \text{for} \quad h_1 \le h \le h_2\\ 10^{\frac{h_2-h}{h_3}} & h_2 \le h \le h_3\end{cases} \tag{10}$$

where h_0, h_1, h_2, and h_3 (cm) are prescribed threshold pressure heads. Finally, the actual transpiration is provided by the integration of the actual root water uptake over depth:

$$T_a = \int_0^{L_r} Q(z,h)dz \tag{11}$$

where L_r is the rooting depth (cm). At crop emergence an initial rooting depth is assumed for each crop. Thereafter, rooting depth increases according to temperature until the maximum rooting depth is reached. The root length density distribution with depth was calculated from a dimensionless weighting factor specified for relative rooting depths.

Biomass increase is estimated from the carbon assimilated by the plant. Here, the potential assimilation is scaled by the ratio T_a/T_p to account for water stress. The glucose assimilation rate A_g (kg CH_20 m^{-2} h^{-1}) is equal to 30/44 of the total carbon assimilation rate A (kg CO_2 m^{-2} h^{-1}), which is obtained by integrating the total instantaneous assimilation rate $A_{L,T}$ (kg CO_2 m^{-2} leaf $surface^{-1}$) over the daylight period and the LAI. In a second step, the net growth rate of dry matter (DM) per unit area GWT (kg DM m^{-2} h^{-1}) is calculated using

$$GWT = \frac{A_g - R_m}{ASQR} \tag{12}$$

where ASRQ (kg DM kg^{-1} h^{-1}) is a coefficient that represents the organic-specific conversion efficiency from glucose to dry matter and R_m (kg CH_20 m^{-2} h^{-1}) is the total maintenance respiration demand, which is controlled by plant senescence and temperature. After determining the net growth, a partitioning into the crop organs is used to describe dry matter accumulation in the roots, storage organs, stems, and leaves. This partitioning is crop-specific and is a function of DVS.

During the crop juvenile stage, the development of LAI is driven by temperature. At later stages, the dry matter growth rate of green leaves $GWLV_G^t$ (kg DM m^{-2} soil h^{-1}) at a specific time-step t is limited by the supply of assimilates. Therefore, the green LAI growth rate $GLAI_G^t$ (m^2 leaf m^{-2} soil h^{-1}) is

$$GLAI_G^t = GWLV_G^t * SLA \quad (13)$$

where SLA (m^2 leaf kg^{-1} DM) is the specific leaf area. The leaf area growth rate decreases during the season because of senescence, self-shading, and chilling temperatures. In the model, a dead LAI growth rate is calculated for different crops and is then subtracted from the $GLAI_G^t$ to describe this reduction in the growth rate.

4.2 Materials and methods

4.2.1 Unique soil-crop combinations

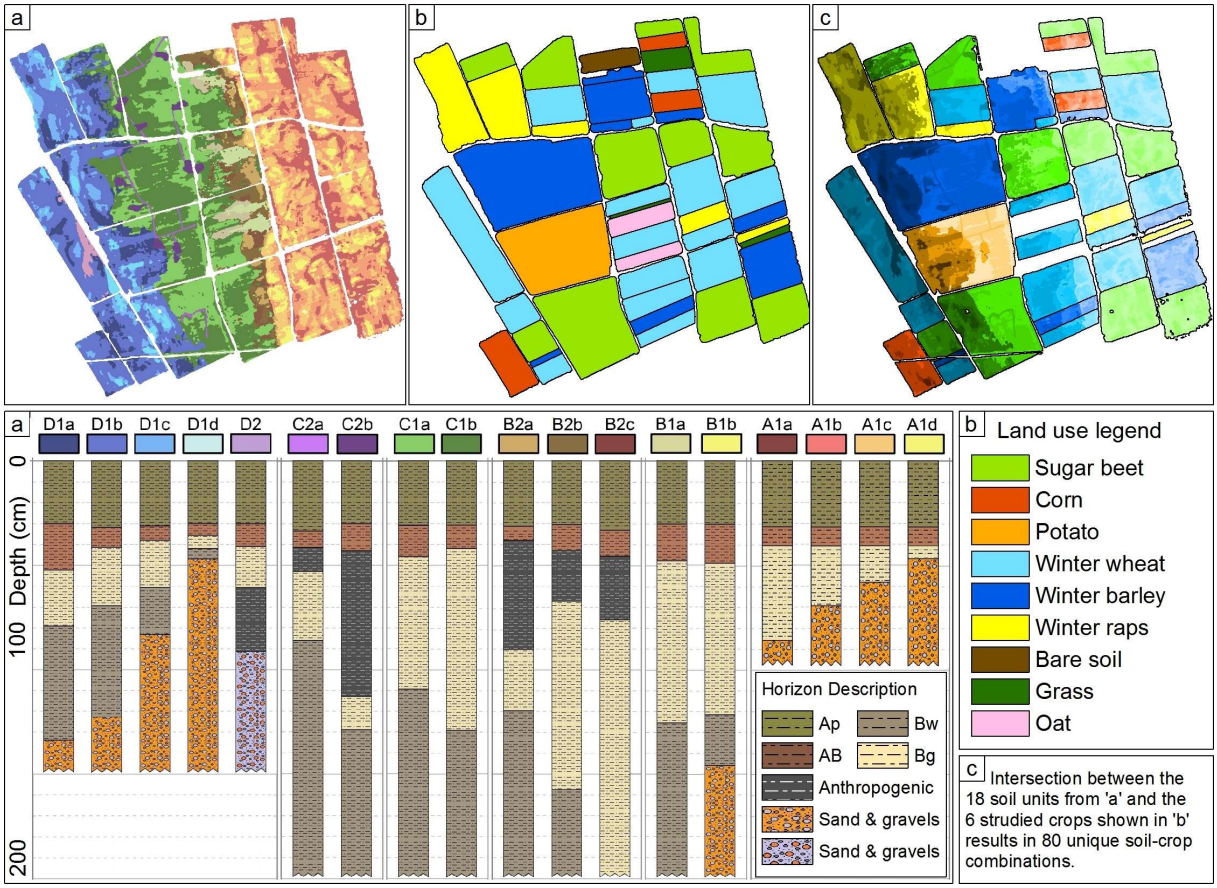

Figure 18: a) Geophysics-based soil map of the study area provided with soil layering description, b) land use of the study area in 2016, and c) map of the 80 unique soil-crop combinations resulting from the intersection of the 18 soil units of the soil map and the six simulated crops.

The land use map shown in Figure 18b was produced by combining the land use described in Chapter 2 (Figure 3) with *in situ* DGPS measurements (Trimble Inc., Sunnyvale, USA). The crops present in 2016 were corn, potato, sugar beet, winter barley, winter rapeseed, and winter wheat. As described in Chapter 2, a small percentage of the area was covered with bare soil, oat, and grass. Due to the small size of these fields, it was decided to exclude them from analysis. In a next step, the geophysics-based soil map (Figure 18a) and the land use map were intersected. This resulted in 80 unique soil-crop combinations (Figure 18c).

4.2.2. Estimation of the hydraulic parameters

In this chapter, the pedotransfer functions (PTF) provided by Rawls and Brakensiek (1985) were used to estimate the hydraulic parameters of each layer of the soil profiles provided by the geophysics-based soil map. This PTF uses the fractions of sand, silt, and clay, and the bulk density to estimate the hydraulic parameters. The bulk density of the fine fraction < 2 mm ($BD_{<2}$) was not directly determined during soil profile characterization and sampling for soil texture. In the upper plow layers, a lower bulk density of $BD_{<2}$ of 1.30 g cm^{-3} for Ap horizons and a $BD_{<2}$ of 1.40 g cm^{-3} for AB horizons were assumed due to regular tillage (Ehlers et al., 1983; Unger and Jones, 1998). For the deeper soil horizons, a $BD_{<2}$ of 1.50 g cm^{-3} was assumed for fine sediments and a $BD_{<2}$ of 1.60 g cm^{-3} was assumed for 2C horizons that contained a lot of coarse material. These assumptions were based on results from previous sampling campaigns conducted on two test fields within the study area (field F01 and F10 in Figure 1). Because of the high gravel content of some soils in the study area, the bulk density of the fine earth fraction was corrected for gravel content according to Brakensiek and Rawls (1994) by

$$BD_t = BD_{<2} + G_v\,(BD_{>2} - BD_{<2}) \tag{14}$$

where BD_t is the bulk density of the soil, $BD_{>2}$ is the bulk density of gravel, and G_v is the volume of gravel (Flint and Childs, 1984). The bulk density of gravel was assumed to be that of solid quartz: $BD_{>2}$ = 2.65 g cm^{-3} (Brakensiek and Rawls, 1994). The volume of gravel was calculated using

$$G_v = G_w/(2 - G_w) \tag{15}$$

where G_w is the weight fraction of gravel (Flint and Childs, 1984), which was available from the soil texture information provided by the geophysics-based soil map.

Table 9: Hydraulic parameters of soil unit A1d estimated using the Rawls and Brakensiek PTF (Rawls and Brakensiek, 1985) and the Rosetta PTF (Zhang and Schaap, 2017).

PTF	Horizon	θ_s (cm^3 cm^{-3})	θ_r (cm^3 cm^{-3})	α (cm^{-1})	n (-)	K_s (cm h^{-1})
Ra. & Br.	Ap (loess)	0.416	0.055	0.0233	1.348	0.2605
Ra. & Br.	AB (loess)	0.401	0.054	0.0216	1.349	0.2099
Ra. & Br.	Bg (loess)	0.372	0.064	0.0150	1.322	0.0914
Ra & Br.	2C (coarse)	0.165	0.052	0.0087	1.306	0.0024
Rosetta	Ap (loess)	0.399	0.070	0.0042	1.558	1.0387
Rosetta	AB (loess)	0.389	0.069	0.0044	1.546	0.8535
Rosetta	Bg (loess)	0.395	0.081	0.0041	1.516	0.0807
Rosetta	2C (coarse)	0.245	0.053	0.0087	1.403	0.0105

Due to the high gravel content of the 2C horizon (estimated to be 70% in the upper terrace and 50% in the lower terrace), the estimates of the hydraulic properties were deemed to be less accurate for this horizon. To avoid introducing variation into the simulation results due to these uncertain hydraulic properties, it was decided to set the hydraulic parameters of the 2C horizon to the same values for all soils of the upper terrace (soil units A1a-d) and for all soils of the lower terrace (soil units D1a-d and D2a). In both cases, the hydraulic parameters were estimated from the average soil texture and corrected bulk density obtained from the estimation procedure outlined above. Finally, the estimated saturated hydraulic conductivity (K_s) (cm h^{-1}) of the 2C horizon was also corrected for gravel content according to Brakensiek and Rawls (1994):

$$K_b = K_s\,[2(1 - G_v)/(2 + G_w)] \tag{16}$$

were K_b is the saturated hydraulic conductivity of the bulk soil (fine earth and gravel) and K_s is the saturated conductivity of the fine earth fraction estimated by the PTF (Rawls and Brakensiek, 1985). In this simple correction, it is assumed that rock fragments have zero conductivity. An example of the estimated hydraulic parameters is shown in Table 9 for soil unit A1a. For comparison, the hydraulic parameters of soil unit A1a obtained by applying the same procedure but using the commonly applied ROSETTA PTF (Zhang and Schaap, 2017) are also shown.

4.2.3. Estimation of LAI from satellite observations

LAI was estimated from RapidEye multispectral satellite imagery using a logarithmic relationship to calculate LAI_{NDVI} from vegetation indices (Ali et al., 2015). Successful applications of this procedure have been published by Hasan et al. (2014), Montzka et al. (2016), Post et al. (2018), Reichenau et al. (2016), and Rudolph et al. (2015). For this work, six RapidEye images with a resolution of 5 m were available. The six images were acquired on 14th March, 20th April, 28th May (Figure 19a), 9th June, 12th August, and 8th September 2016, and thus cover the full growing season of various crops. Further data had to be discarded because of dense cloud cover and relatively poor illumination conditions with associated low signal-to-noise ratios.

In a first step, the NDVI (Normalized Difference Vegetation Index) was calculated for each image pixel using

$$\mathrm{NDVI} = \frac{\mathrm{NIR}-\mathrm{R}}{\mathrm{NIR}+\mathrm{RED}} \tag{17}$$

where NIR is the near infra-red (760-850 nm) and RED is the red spectral band (630 – 685 nm). An example of a NDVI map calculated from the satellite image of the 28th of May is shown in Figure 19b. In a next step, the fractional vegetation cover (FVC_{NDVI}) of each image was calculated using

$$\mathrm{FVC_{NDVI}} = \frac{\mathrm{NDVI}-\mathrm{NDVI_S}}{\mathrm{NDVI_V}-\mathrm{NDVI_S}} \tag{18}$$

where $NDVI_s$ is the NDVI for bare soil and $NDVI_v$ is the value at the fully vegetated state (Beck et al., 2006; Xiao and Moody, 2005; Zeng et al., 2003). The values of $NDVI_s$ and $NDVI_v$ were estimated through histogram evaluation ($NDVI_V$ = -0.05 and $NDVI_S$ = 0.81). Finally, the LAI_{NDVI} was calculated using

$$\mathrm{LAI_{NDVI}} = \frac{-\log\left(1-\mathrm{FVC_{NDVI}}\right)}{\mathrm{k}(\theta)} \tag{19}$$

where k(θ) is the light extinction coefficient for a given solar zenith angle (θ). This coefficient is a measure of attenuation of radiation in the canopy and depends on factors such as the latitude, date, solar elevation and declination, and terrain geometry.

A set of 45 *in situ* LAI measurements performed between 22nd March and 7th September 2016 were used to estimate k(θ) of sugar beet, winter barley and winter wheat. The fields in which these measurements were performed are shown in Figure 1a. At each sampling location, destructive measurements of LAI were performed by sampling 0.5 m of plants from three adjacent rows in wheat and barley. For sugar beet, three individual plants were collected and crop density was determined in the field.

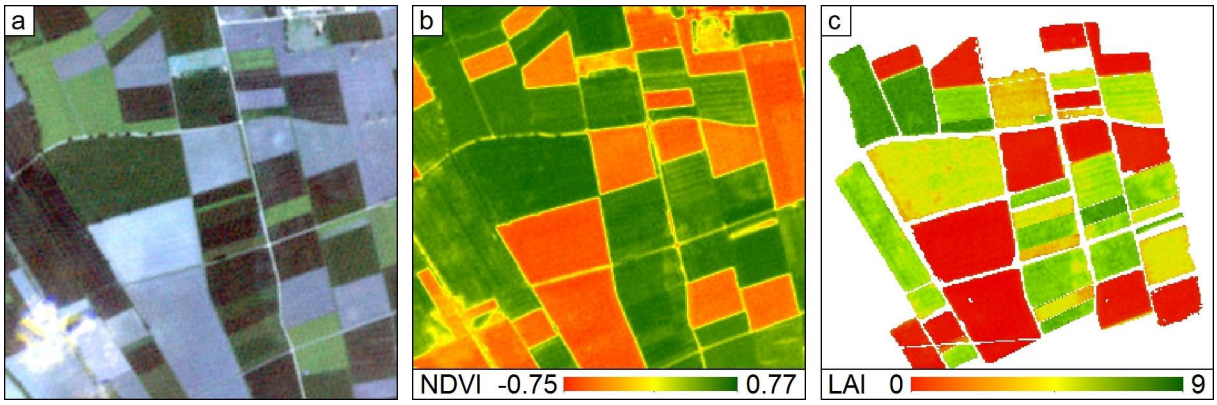

Figure 19: a) RapidEye satellite image of the study area at the 28th of May, b) NDVI map calculated from the satellite image, and c) LAI_{NDVI} map calculated from NDVI and *in situ* measurements.

Subsequently, the leaf area was measured in the lab by using a Flatbed Scanner (Epson GT-15000, Seiko Epson Corp., Suwa, Japan) and a public domain image analysis software (ImageJ, 2016). Upscaling to a square meter was performed based on the harvested area. These *in situ* LAI values were compared with the respective FVC_{NDVI} values to obtain an estimate of k(θ). In this process, only *in situ* measurements that were performed 8 days or less before or after the acquisition date of a satellite image were used. The number of *in situ* measurements, the R^2 between FVC_{NDVI} and *in situ* LAI, and the k(θ) of each crop are shown in Table 10. An example of a LAI_{NDVI} map calculated from the satellite image of the 28th of May is shown in Figure 19c.

In sugar beet, the initial R^2 obtained by using all available *in situ* measurements was rather low with 0.29. Therefore, two different k(θ) were used: one value for RapidEye images from March to August, and one value for September. This improved the resulting R^2 considerably to 0.79 (March-August) and 0.74 (September). The use of two different k(θ) within the growing season is justified by the fact that non-irrigated sugar beet generally suffers from water stress (Hoffmann and Kenter, 2018), which is known to have an immediate effect on leaf geometry and other plant characteristics (De Costa and Dennett, 1992). Late summer

water stress in sugar beet was reported in previous studies within the study area (Rudolph et al., 2015; Stadler et al., 2015). Similarly, two k(θ) were used in winter wheat since the R^2 obtained using all available measurements was 0.6 only. When two different values of k(θ) were used in March-April and in May-September, much improved R^2 values of 0.90 and 0.98 were obtained. On the contrary, barley showed an overall higher R^2 of 0.75 when all the available LAI measurements were used in the calculation of k(θ). In the case of corn, potato, and winter rapeseed, k(θ) was set to 0.25 since no ground-based LAI measurements were available for calibration. This value was suggested by Ali et al. (2015) to obtain LAI_{NDVI} maps from RapidEye in this area.

Table 10: Number of in situ LAI measurements for each crop, R^2 between FVCNDVI obtained from RapidEye images and in situ LAI, and estimated k(θ) coefficients.

Plant	N. of meas.	R^2	k(θ)
Sugar beet	13/6	0.79/0.74	0.33/0.49
Corn	NA	NA	0.25
Potato	NA	NA	0.25
Winter wheat	18	0.90/0.98	0.60/0.35
Winter barley	8	0.75	0.65
Winter raps	NA	NA	0.25

4.2.4. Set-up of the AgroC simulations

In the AgroC simulations, the soil is discretized using up to 232 nodes with variable separation: 0.1 cm for the first 10 nodes, 0.2 cm for nodes 11 to 20, 0.5 cm for nodes 21 to 30, 0.5 cm for nodes 31 to 40, and 1.0 cm until node 232 or until the profile depth was reached. Each node was assigned to a particular soil layer with associated hydraulic properties based on the soil profile description for each of the 80 unique soil-crop combinations derived from the land use and the geophysics-based soil map.

Two different set- ups were used for the AgroC simulations. The first set-up was used for soil profiles that have a coarse 2C horizon at the bottom of the soil profile. This includes all soils of the upper terrace and some soils of the lower terrace (i.e., soil units A1a-d, D1a-d and D2a in Figure 18). This coarse and less conductive layer is known to have a strong influence on water flow and crop growth (Rudolph et al., 2015; von Hebel et al., 2018). For these soils, the depth of the simulation domain was defined to be from the surface down to a depth of 3 cm into the 2C horizon. This resulted in different depths for the simulation domains that ranged from 52 cm to 137 cm depending on the soil profile description. The lower boundary

condition was set to free drainage for these profiles. This set-up and selection of boundary conditions was required to avoid unrealistic upward water flow from the 2C horizon that occurred when using longer soil profiles. The second set-up was used for soil profiles where fine sediments were present at depth. In this case, the simulation domain extended from the surface down to a depth of 2.0 m. A water table with variable depth was used to define a variable pressure head as the lower boundary condition. The maximum and minimum depth of the water table were obtained from a CTD-5 sensor (Decagon devices, Pullman WA, USA) installed in a well in the western part of field F10 (Figure 1). In 2015 and 2016, the water table below surface depth varied periodically over the year. The minimum depth was 2.0 m at ~15th January and the maximum depth was 2.6 m at ~15th July.

Crop-specific parameters required to parameterize AgroC were mainly obtained from literature (Allen et al., 1998; Bolinder et al., 1997; Boons-Prins et al., 1993; Borg and Grimes, 1986; Penning de Vries, 1989; Spitters et al., 1989; Van Heemst, 1988; Vanclooster, 1995; Vries, 1989). The parameters of the root water uptake stress parameters (Eq7) were set to h_0 = 0 cm, h_1 = -20 cm, h_2 = -5000 cm, and h_3 = -16000 cm (Vanclooster, 1995). For each crop, a specific maximum rooting depth was set: 150 cm for sugar beet and corn, 140 cm for rapeseed, 120 cm for barley, and 100 cm for wheat and potato. The root distribution with depth was calculated using the method of Rum et al. (1974). Due to the high bulk density of the 2C horizons, it is assumed that roots cannot grow into this layer due to high penetration resistance (Daddow and Warrington, 1983). Therefore, the rooting depth was reduced when a coarse 2C horizon was present within the rooting depth. In such a case, the root distribution between the surface and the 2C horizon was extracted from the distribution that was calculated with the crop-specific maximum rooting depth (i.e., a truncated root length distribution).

Meteorological data for 2015 and 2016 were used to define the upper atmospheric boundary condition using precipitation and potential grass reference evapotranspiration according to the Penman-Monteith approach (Allen et al., 1998). All simulations started on 1st July 2015 and ended on 31st December 2016, thus allowing simulation of both summer and winter crops. Two strategies were again used to define the initial pressure heads within each soil profile. The first strategy was applied to soil profiles where a water table with variable depth was used as lower boundary condition. Here, a spin-up simulation was used by repeatedly running a period of two years (1st of January 2015 to 31st of December 2016) until the pressure head

within the soil column did not change between subsequent simulations. This spin-up strategy resulted in very low water content within the soil column when simulating soil profiles with a free drainage boundary at the bottom. To avoid such unrealistically low initial water contents in these soil profiles, the pressure head of the underlying 2C horizon was set to -1 cm and hydrostatic equilibrium was assumed for the rest of the profile.

4.3. Results and discussion

4.3.1. Water content simulations for field F01

In Figure 20a-b, the soil water content measured at P01 and P02 is compared with the soil water content simulated with AgroC for soil units A1a and A1d. In general, the simulated and measured soil water content showed a similar response to atmospheric forcing with increasing water content after precipitation events followed by a dry-down in periods without precipitations in both locations. For the location P1 in soil type A1a (Figure 20a), the average RMSE between measured and simulated water content for all three soil depths was 0.056 cm^3 cm^{-3}. In general, the simulated water content was very similar for all three depths, whereas the measured water content considerably increased with depth and showed a stronger response to atmospheric forcing. For location P02 in soil type A1d (Figure 20b), the average root mean square error (RMSE) between measured and simulated water content for all three soil depths was considerably lower with 0.032 cm^3 cm^{-3}. However, differences between measured and simulated water content were also clearly present. For example, two peaks in measured soil water content at 10 cm depth in August were not well captured by the model. Also, the measured soil water content at 50 cm was overestimated during the dry period from August onward.

This difference in performance for the two locations is related to discrepancies between the actual soil profile and the average soil profile of the two soil units obtained from the geophysics-based soil map. In general, the actual horizon depths at point P02 were similar to the horizon depths of the soil profile of soil unit A1d. At this location, a rather thin layer of loess sediment was deposited on a coarse sand and gravel layer. The actual depth of the loess layer was 47 cm, whereas it was 49 cm in soil unit A1d of the soil map. Therefore, there was a good match between measured and simulated water content. For point P01 in soil unit A1a, a larger mismatch between the actual and the average soil profile was observed. In particular, the actual thickness the loess layer at P01 was 160 cm, whereas the average thickness of this

layer was only 87 cm in soil unit A1a. The differences in soil profile description are a likely explanation for the mismatch between the simulated and the measured water content at this location. Obviously, these differences are due to the scale mismatch between the point measurements and the geophysics-based soil map. This soil map is expected to capture the main variability in soil properties at the 1 km^2 scale, but is not expected to capture small-scale variabilities in profile depth and description within one soil unit. Apparently, P01 was not a representative location for the soil unit A1a and therefore it could not be simulated with the same accuracy as P02.

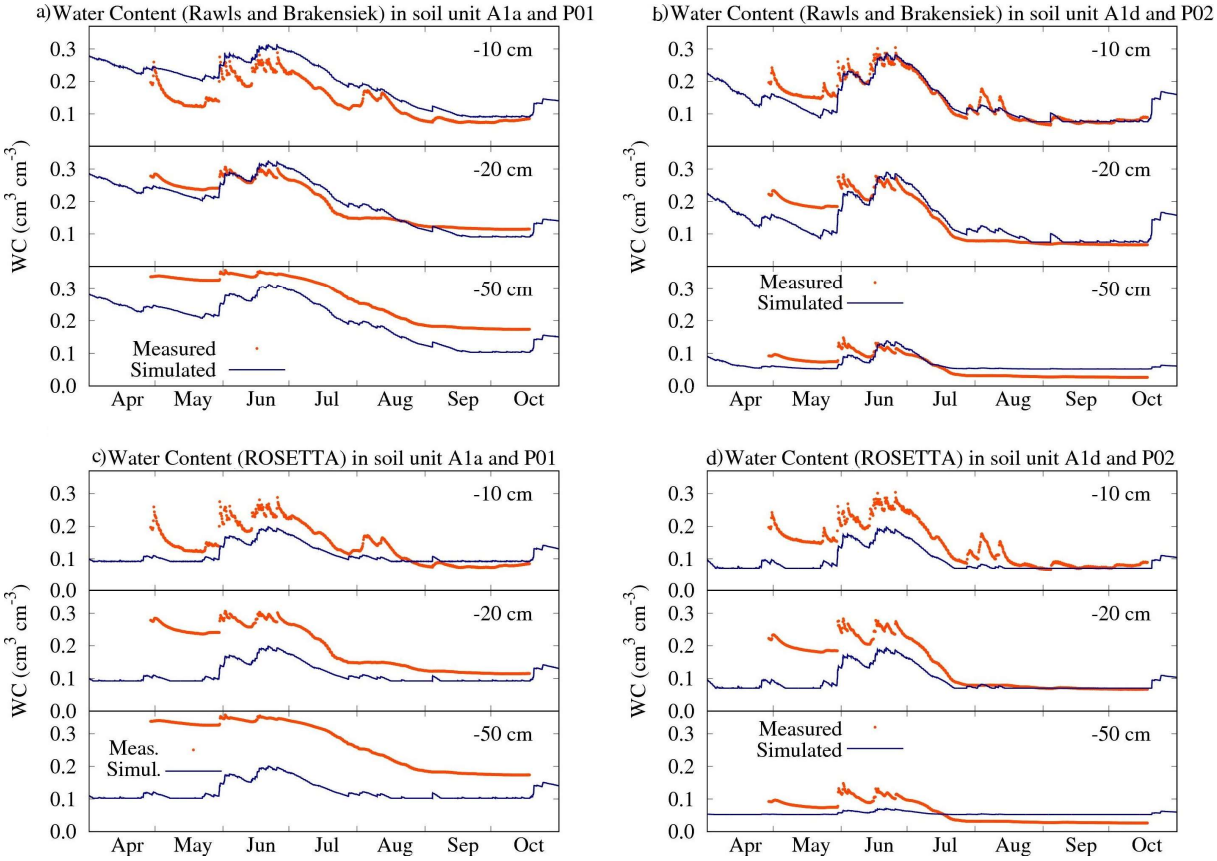

Figure 20: a) Simulated and measured soil water contents (cm^3 cm^{-3}) for sugar beet grown in soil unit A1a at P01, b) simulated and measured soil water contents (cm^3 cm^{-3}) for sugar beet grown in soil unit A1d at P02 based on the hydraulic parameters estimated by the PTF of Rawls and Brakensiek (1985), c) simulation performed for sugar beet grown in unit A1a at P01 and d) in unit A1d and P02 based on the ROSETTA PTF.

To investigate the sensitivity of the AgroC simulations to the choice of the PTF, the simulations for locations P01 and P02 were repeated with soil hydraulic parameters estimated from the widely used ROSETTTA PTF (Figure 20c-d). It can be seen that a stronger mismatch between measured and simulated water content was found when the ROSETTA

PTF was used. In particular, the RMSE increased from 0.056 to 0.134 cm^3 cm^{-3} for soil type A1a, and from 0.032 to 0.072 cm^3 cm^{-3} for soil type A1d. Also, the simulated water content obtained with ROSETTA PTF seemed unrealistically low for both soil units. The estimated hydraulic parameters of soil unit A1d using the Rawls and Brakensiek as well as the ROSETTA PTF are given in Table 9. It can be seen that the K_s estimated with ROSETTA was up to five times higher, and this likely explains the low simulated water contents and the increase in the mismatch between measured and modelled water content. Since the unrealistically low simulated water content was observed for all soil units, it was preferred to use the PTF of Rawls and Brakensiek in this chapter. Overall, it is concluded that the presented parameterization strategy provides reasonable predictions of soil water content dynamics considering that the soil profiles were obtained from a soil map and no calibration was used to improve the fit between measured and modelled soil water content.

4.3.2. Validation of LAI and yield simulations

In a next step, the results of the AgroC simulations at the km^2 scale are evaluated using LAI_{NDVI} derived from satellite remote sensing. When available, yield information is also used for model evaluation. The results will be presented for three groups of units: i) the soils of the upper terrace (units A1a-d), ii) the soils of the lower terrace with underlying fine layers (soil units B1a-b, B2a-c, C1a-b, and C2a-b), and iii) the soils of the lower terrace with underlying coarse layers (soil units D1a-d and D2a). For simplicity, we will refer to second group as BC soil units. In the following, we first present results for the summer crops that are more prone to water stress (sugar beet, corn, and potato) followed by the winter crops (wheat, barley, and rapeseeds).

4.3.2.1. Simulation of sugar beet

Figure 21a-c shows the simulated LAI (lines) and the observed LAI_{NDVI} (dots) for all soil units grown with sugar beet. The observed LAI_{NDVI} was obtained by averaging all LAI_{NDVI} values within each unique soil-crop combination. High LAI was observed for all BC soil units, which indicates that the crops in this area were not stressed. On the contrary, a generalized reduction in LAI_{NDVI} was observed in soil units A1a-d and D1a-d, and the reduction appears to be proportional to the depth of the coarse layer. In order to capture these differences in LAI between the three groups of soil units with the AgroC model, it was necessary to use three different crop parameterizations. In fact, the water stress simulated with

AgroC reduced the accumulation of new dry mass but had less influence on the green LAI, which was accumulated before the occurrence of prolonged periods of water stress in July and August (Figure 21d). In order to match the differences in observed LAI between the three groups of soil units, the death rate of the leaves was calibrated. After calibration, the death rate of the leaves was highest in soil units A1a-d, intermediate in D1a-d, and lowest in the BC units (see supplementary material S.2 for a detailed description of the input parameters). All other plant parameters were identical in all simulations. Therefore, the differences in LAI shown within each group of soils are solely due to differences in soil parameterization in terms of layering and hydraulic properties.

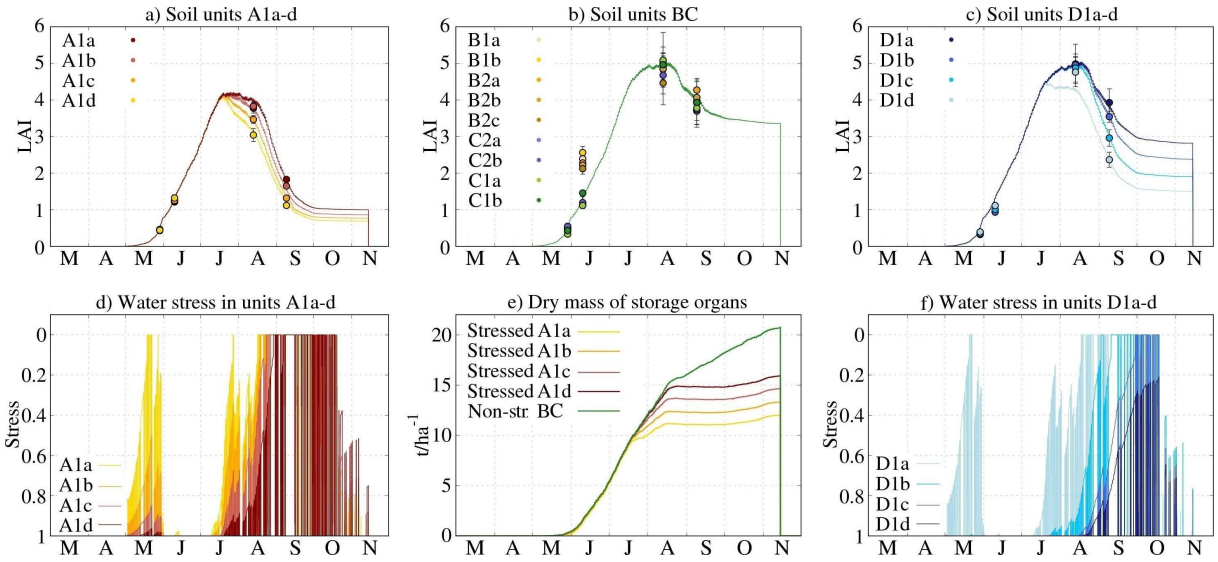

Figure 21: Simulations for sugar beet. a) Simulated LAI (lines) and observed LAI_{NDVI} (points) in soil units A1a-d, b) in soil units BC, c) and in soil units D1a-d. d) Simulated water stress in soil units A1a-d, f) and in soil units D1a-d. e) Simulated mass of storage organs at harvest in soil units A1a-d and BC.

In soil units A1a-d (Figure 21a), the LAI_{NDVI} was similar for all four soil units early in the growing season (May-June). This was well reproduced by the model simulations, despite the strong water stress in this period (Figure 21d). Apparently, this stress period did not strongly affect the simulated accumulation of aboveground biomass at this initial stage of crop development. In the second half of June and July, there was a period with no water stress where the simulated LAI increased rapidly. Afterwards, the absence of rain resulted in water stress and an associated reduction of LAI in August and September. Here, the simulated LAI was lower in soil units with higher water stress, and matched well with both the maximum value and the decrease of observed LAI_{NDVI} in response to water stress.

In soil units BC (Figure 21b), simulated LAI and observed LAI_{NDVI} generally matched well, but only showed limited variability between soil units. This is explained by the lack of water stress in this area. A mismatch can be observed on the 9th of June where simulations matched the LAI_{NDVI} of soil units C1a-b and C2a-b (LAI = 1.1-1.4) but did not match the LAI_{NDVI} of the soil units B2a-b and B2a-c (LAI = 2.2-2.6). This is attributed to differences in seeding and emergence dates between soil units that are not captured in the model. This is supported by the fact that the two groups of soil units are located in separate fields with different owners (units C1a-b/C2a-b in field F46 and units B1a-b/B2a-c in fields F12 and F50).

In soil units D1a-d (Figure 21c), a general decrease in LAI proportional to the amount of simulated water stress was observed in the second half of the growing season (similar to the soil units A1a-d). However, the simulated stress in D1a-d is generally lower than in A1a-d since the coarse layers are generally deeper in D1a-d and have different soil hydraulic parameters (Figure 4f). Again, simulated LAI and observed LAI_{NDVI} matched well. Until August, the simulated LAI for soil units D1a-c was very similar. A considerable difference between soil units was simulated on the 8th of September because water stress reduced the LAI of soil units D1a-c. This simulated behavior is well supported by the observed LAI_{NDVI}. On the contrary, the simulations for soil unit D1d underestimated LAI_{NDVI}, likely because water stress was overestimated. However, the area represented by unit D1d is small (0.3 ha within fields F50 and F51) compared to the total area cropped with sugar beet in 2016 (26.5 ha).

The simulated productivity of sugar beet (dry weight of storage organs) expressed in t ha^{-1} is shown in Figure 21e for selected soil units. The simulated productivity at harvest of the soil units A1a-d ranged from 12.0 to 15.9 t/ha and was well below the simulated productivity of soil units BC that was 20.7 t/ha. Here, a reduction in the mass allocated to the storage organs is apparent from July until the end of the growing season and is proportional to the magnitude of water stress. The simulated productivity at harvest of soil units A1a-d was compared with the actual productivity at harvest of field F01 in 2016. The area-weighted average simulated productivity (productivity of soil units A1a-d weighted on the actual area of each unit) in field F01 was 14.3 t ha^{-1} and well matched the actual productivity of 14.2 t ha^{-1}. The simulated productivity of soil units BC and D1a-d was compared with the average productivity at harvest of field F11 in 2011, 2014, and 2017. Again, the average simulated productivity of 19.7 t ha^{-1} in 2016 was similar to the average observed productivity of 19.3 t ha^{-1}.

4.3.2.2. Simulation of corn

The observed LAI_{NDVI} for corn in soil units A1a-d (Figure 22a) was similar on the 28th of May (~LAI = 0.4) and on the 9th of June (~LAI = 1.6). In contrast, the observed LAI_{NDVI} for soil units D1a-d (Figure 22c) was more variable on the 28th of May (ranging from 0.3 to 0.8). This indicates that the LAI of corn was quite heterogeneous in space at this point in time, likely due to different emergence dates within these soil units. In addition, the observed LAI_{NDVI} on the 9th of June (~LAI = 0.6) was lower than that of the soil units A1a-d, suggesting the presence of younger crops. Therefore, simulations were performed using the same crop parameterization, but with different emergence date. The emergence date for soil units A1a-d was set to 1st of May and the emergence date for soil units D1a-d was set to 10th of May.

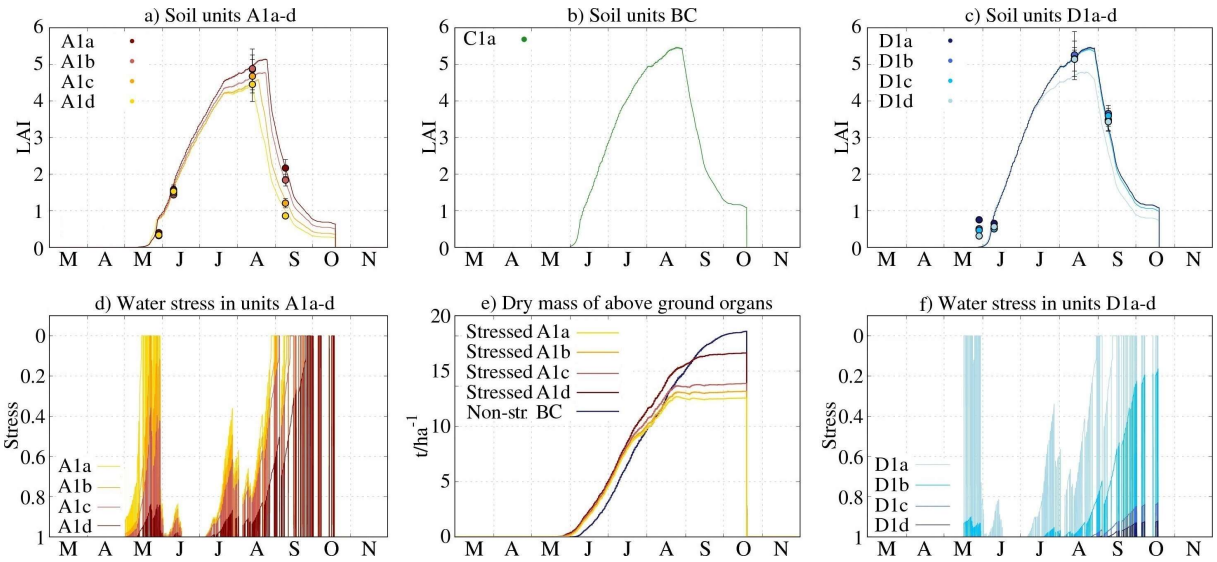

Figure 22: Simulations for corn. a) Simulated LAI (lines) and observed LAI_{NDVI} (points) in soil units A1a-d, b) in soil units C1a, c) and in soil units D1a-d. d) Simulated water stress in soil units A1a-d, f) and in soil units D1a-d. e) Simulated mass of above surface organs at harvest in soil units A1a-d and D1a.

The simulated LAI for soil units A1a-d (Figure 22a) suggested a homogeneous growth until late May. Afterwards, the simulated LAI of the four soil units diverged and showed considerable differences from June to August. The simulated LAI matched the observed LAI_{NDVI} well in general, although the simulated LAI of soil units A1b-c somewhat underestimated LAI_{NDVI}. Since water stress was relatively low in June compared to the second part of the growing season, this variability in simulated LAI was attributed to the combination of the early stress period in May with later stress in July and August. The following abrupt decrease in LAI_{NDVI} was due to the senescence stage of corn development. Interestingly,

differences in LAI_{NDVI} due to water stress were still present at this development stage. In the AgroC model, senescence in corn starts when a certain value of crop DVS is reached. In order to match the observed variation in LAI_{NDVI} at the 8th of September, four different DVS were used to start senescence at four different times in the soil units A1a-d. Earlier senescence was assumed in soil units where stronger water stress was observed since it was apparent from field observations how stronger stress resulted in smaller crops and early senescence. This required a modification of the model code as described in the supplementary material S.2.

The simulated LAI for soil units D1a-c (Figure 22c) showed similar development throughout the growing season. This is consistent with the observed values of LAI_{NDVI}. In contrast to soil units A1a-d, the water stress simulated in May was rather low for these three soil units and did not affect the simulated LAI in the following months (Figure 22f). In this case, the later emergence date for soil units D1a-c prevented water stress from strongly affecting LAI in the early stage of corn growth. To corroborate this hypothesis, we performed the same simulation on soil unit C1a that typically does not show water stress. The simulated LAI of corn grown on this soil unit is shown in Figure 22b and matched well with the simulated LAI of soil units D1a-c. This confirms that water stress in the early growth stage of simulated corn has a strong influence on simulated LAI. In the case of soil unit D1d, simulated LAI was strongly reduced by water stress and did not match LAI_{NDVI} values. Again, this is attributed to the very small area of this soil-crop combination (0.05 ha).

Figure 22e shows the simulated aboveground biomass of corn in soil units A1a-d and C1a, which is used as a measure of productivity because corn is used for livestock feeding in this area. The simulated productivity ranged from 12.5 to 17.1 t ha^{-1} in soil units A1a-d, and was 18.7 t ha^{-1} in C1a. These simulated productivity values are in good agreement with the results of Žydelis et al. (2018), who used a comparable methodology and found similar measured and simulated productivity: ~18.5 t ha^{-1} in healthy corn and ~14.5 t ha^{-1} in stressed corn.

4.3.2.3. Simulation of potato

Figure 23b-c shows the simulated LAI and the observed LAI_{NDVI} of potato in soil units C1a-b, C2a-b, and D1a-d. The observed LAI_{NDVI} only showed small variations, except for the 12th of August were moderate differences between soil units C1a-b/C2a-b (from ~4.4 to ~4.7) and soil units D1a-d (from ~3.8 to ~4.3) were observed. Overall, the AgroC model was able to capture LAI development of potato fairly well. However, Figure 23d shows that the simulated

water stress in soil units D1a-d was rather strong and affected the simulated LAI (Figure 23c) and the simulated dry biomass above ground (Figure 23e) to some extent. Unfortunately, no clear correlation between variations in simulated LAI and LAI_{NDVI} due to water stress was observed. This is attributed to irrigation of the potato field cropped in 2016. Regrettably, detailed information on the amount, timing, and location of this irrigation was not available. Therefore, it was not possible to meaningfully implement irrigation in our simulation. It is expected that irrigation increased the LAI_{NDVI} in soil units where strong water stress was simulated with AgroC, thus preventing a clear expression of water stress in LAI_{NDVI}.

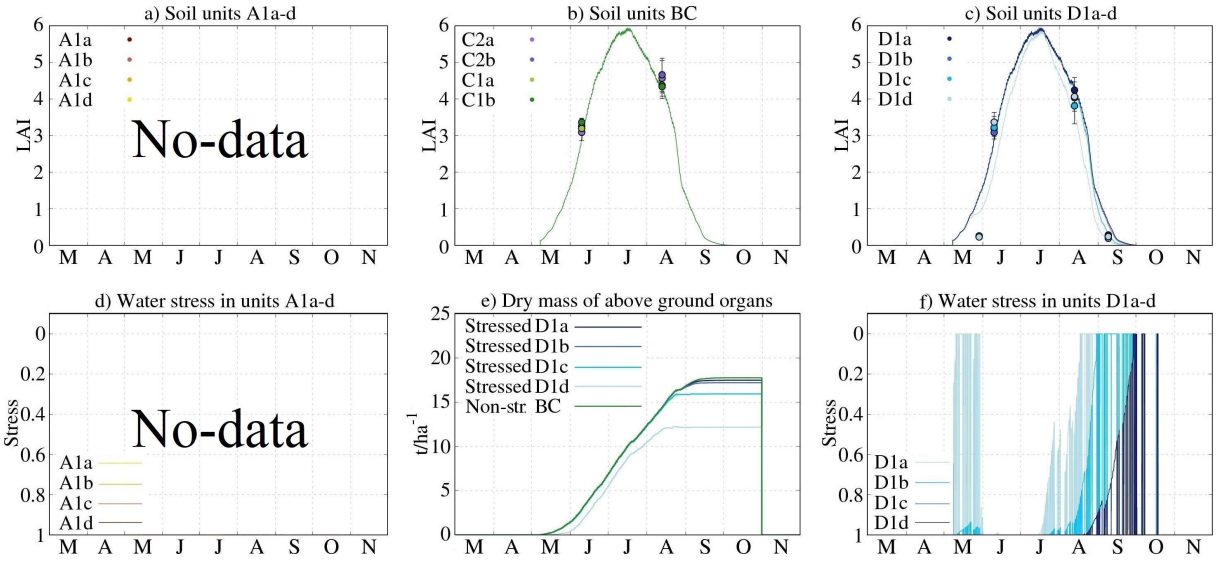

Figure 23: Simulations for potato. a) Simulated LAI (lines) and observed LAI_{NDVI} (points) in soil units A1a-d (no potatoes were cropped), b) in soil units BC, c) and in soil units D1a-d. d) Simulated water stress in soil units A1a-d (no potatoes were cropped), f) and in soil units D1a-d. e) Simulated mass of above surface organs at harvest in soil unit BC and D1a-d.

4.3.2.4. Simulation of winter wheat

The AgroC simulations for winter wheat are shown in Figure 24. Similar to sugar beet, three different crop parameterizations were used. In order to capture observed difference in maximum LAI_{NDVI}, it was necessary to calibrate the partitioning of the mass allocated to the stem and to the leaf as described in detail in the supplementary material S.2. As in the case of sugar beet, one parameterization was used for each group of soil units shown in Figure 24a-c. Thus, the variability in simulated LAI between soil units A1a-d and between soil units D1a-d can only be the results of different soil parameterizations. As shown in Figure 24, water stress was rather low throughout the growing season for winter wheat and was limited to three

distinct periods: late February and March, May, and finally in June. It is important to note that the simulated stress in February and March is caused by high water contents.

In soil units A1a-d (Figure 24a), simulated LAI is consistent with observed LAI_{NDVI}. Both simulated and observed LAI showed little variation between soil units A1a-c, and lower values for soil unit A1d at the 14th of March and at the 20th of April. In soil units BC (Figure 24b), the observed LAI_{NDVI} was generally higher than in the other soil units. Here, all values of LAI_{NDVI} were similar throughout the year and the simulated LAI matched the observed LAI_{NDVI} well. A similar result was obtained for soil units D1a-d and D2a, although the variability between soil units was somewhat higher than in the BC soil units. However, this variability does not seem to be related to simulated stress, except for soil unit D1d (Figure 24c) that showed lower simulated LAI and observed LAI_{NDVI} at the 28th of May and at the 9th of June compared to the soil units D1a-c.

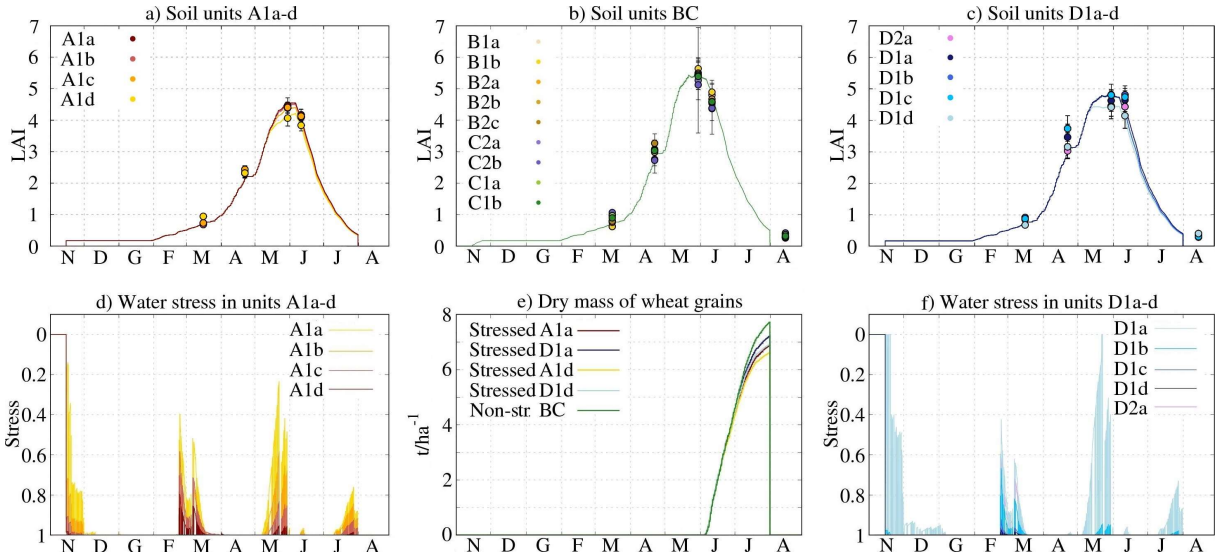

Figure 24: Simulations for winter wheat. a) Simulated LAI (lines) and observed LAI_{NDVI} (points) in soil units A1a-d, b) in soil units BC, c) and in soil units D1a-d. d) Simulated water stress in soil units A1a-d, f) and in soil units D1a-d. e) Simulated productivity at harvest in soil unit A1a, A1d, BC, D1a, and D1d.

Despite the lower magnitude compared to summer crops, water stress affected simulated productivity of winter wheat at harvest for the different soil units (Figure 24e). This is due to the fact that the storage organs grow until the end of the growing season (June and July), and are thus more influenced by water stress than LAI (Steduto et al., 2012). Here, non-stressed soil units produced 7.7 t ha^{-1} of dry grains whereas the most stressed soil unit produced 6.6 t ha^{-1}. These values are comparable to actual yields observed in other studies (Han and Yan,

2017; Káš et al., 2018; Liu et al., 2017) for winter wheat growing under no- and low water stress conditions.

4.3.2.5. Simulation of winter barley

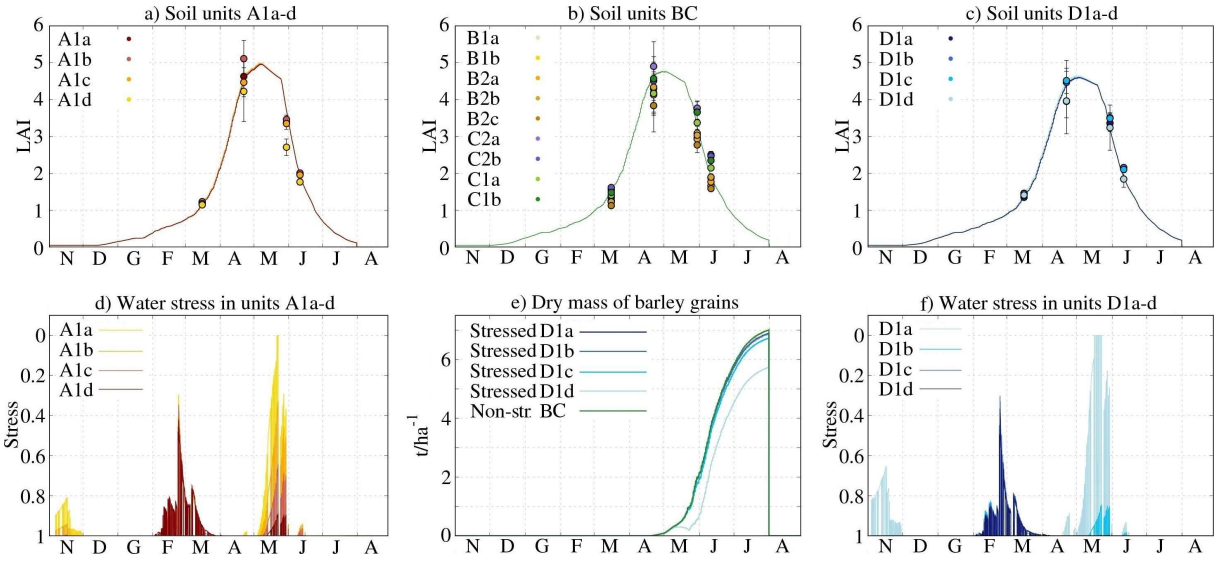

Figure 25: Simulations for winter barley. a) Simulated LAI (lines) and observed LAI_{NDVI} (points) in soil units A1a-d, b) in soil units BC, c) and in soil units D1a-d. d) Simulated water stress in soil units A1a-d, f) and in soil units D1a-d. e) Simulated productivity at harvest in soil units BC, and Da-d.

The simulated and observed LAI for winter barley are shown in Figure 25a-c. Here, the same crop parameterization was used for all simulations except for the emergence date, which was set to 10th of December for soil units A1a-d, 1st of December for the BC soil units and for soil units D1a-d. These different emergence dates resulted in lower simulated LAI for soil units A1a-d compared to D1a-d at the 20th of March, which is consistent with the observed LAI_{NDVI}. Throughout the growing season, the variability in LAI_{NDVI} at each date was rather low and was not related to water stress (Figure 25d and Figure 25f). For the BC soil units, the observed LAI_{NDVI} showed some variability within each date. However, this variability was seemingly not related to the specific characteristics of each soil unit. In summary, the simulated LAI of winter barley well matched the observed LAI_{NDVI} after selecting appropriate emerging dates. However, LAI_{NDVI} showed rather small differences between soil units, and effects of water stress were thus not observed.

As discussed in the case of wheat, barley yield is more sensitive to changes in growing conditions during the period when grain number is set (Steduto et al., 2012). For this reason, the water stress simulated in May had an influence on the final dry mass of grains (Figure

25e). The simulated dry weight of barley grains in soil units D1a-d and BC in field F11 was 6.9 t ha^{-1}. This simulated value for field F11 was identical to the harvest reported by the field owner in 2016.

4.3.2.6. Simulation of winter rapeseed

Simulations for winter rapeseed were performed using a single crop parameterization, but the emergence date was set to the 10th of November for soil units A1a-d and to the 1st of November for soil units BC and D1a-d based on observed LAI_{NDVI}. Figure 26a-c shows the simulated LAI and the LAI_{NDVI} of winter rapeseed, whereas Figure 26d and Figure 26f shows the water stress simulated in soil units A1a-d and D1a-d. A single peak of water stress was present in May and no other stress was obtained throughout the rest of the simulation.

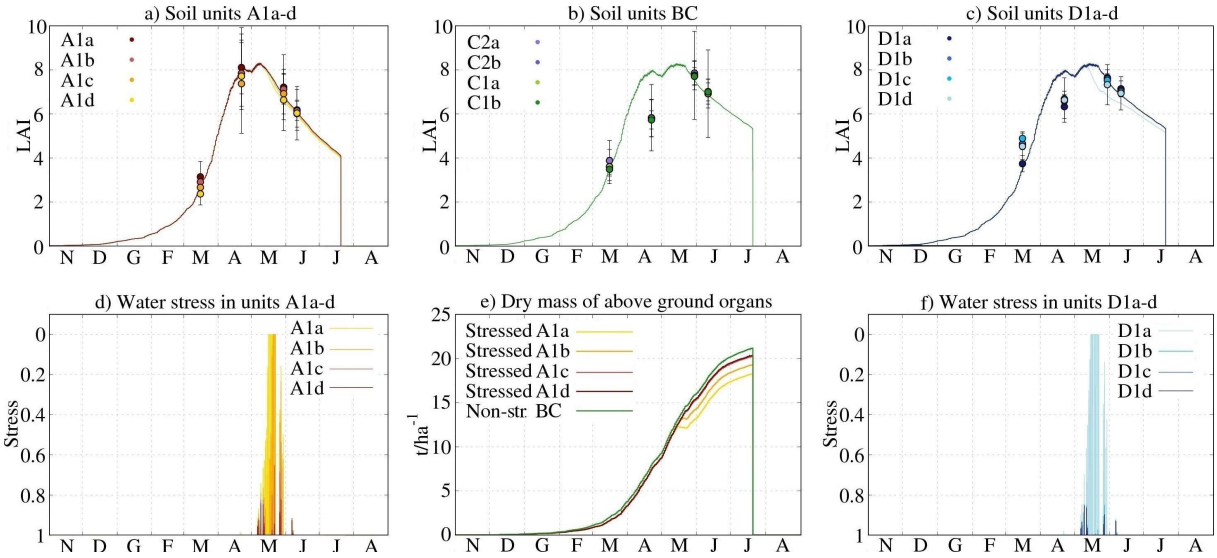

Figure 26: Simulations for winter rapeseed. a) Simulated LAI (lines) and observed LAI_{NDVI} (points) in soil units A1a-d, b) in soil units BC, c) and in soil units D1a-d. d) Simulated water stress in soil units A1a-d, f) and in soil units D1a-d. e) Simulated productivity at harvest in soil unit A1a-d and BC.

In the absence of extended periods of water stress, only small variations in simulated LAI were observed between different soil units. In contrast, some variability in observed LAI_{NDVI} was found for soil units A1a-d, especially for the 14th of March and at the 20th of April (Figure 26a), which suggests that the simulations underestimate the variation observed in the LAI_{NDVI}. On the 9th of June, both simulated and observed LAI did not vary between soil types anymore and showed a similar value (~LAI = 6.1).

The simulated LAI for soil units C1a-b, C2a-b, and D1a-d (Figure 26b-c) did not match the observed LAI_{NDVI} at all times. Obvious differences between simulated and observed LAI were present at the 14th of March and at the 20th of April. In March, the LAI_{NDVI} of soil units D1a-d showed considerable variability with LAI values ranging from 3.8 for soil unit D1a to 4.9 for soil unit D1c. This variability was not captured by the LAI simulations. The reason for this variability in LAI_{NDVI} may be associated with factors that are not considered in our modelling approach (e.g., nutrient availability, within-field management). In April, the simulated LAI considerably overestimated the observed LAI_{NDVI}. Here, the low observed LAI_{NDVI} may have been influenced by the blooming of winter rapeseed that occurs in April or May. This blooming has an influence on the LAI estimated from satellite remote sensing, and may have resulted in lower LAI_{NDVI} values. It is possible that the LAI_{NDVI} of soil units A1a-d were not affected by this because the late emergence date may have delayed the blooming stage. Overall, it is important to note that the simulated water stress had a rather low impact on crop growth.

4.3.3. LAI simulations at the km² scale

Figure 27 compares the simulated LAI of the 80 unique soil-crop combinations with the LAI_{NDVI} derived from the six RapidEye satellite images. Generally, the spatial pattern in the observed LAI_{NDVI} is well reproduced and the simulated emergence, growth, and senescence of each crop are well timed. However, a closer inspection allows identifying several discrepancies. For example, differences in simulated LAI and observed LAI_{NDVI} of corn (fields F13b, F41, and F42 in Figure 27) and sugar beet (fields F01, F05, F12, F13a, and F46-51 in Figure 27) can be observed in August and September (Figure 27e-f). In this case, the general average of each soil-crop combination is well captured (Figure 21a-c and Figure 22a-c). However, a lower variability was found in simulated LAI compared to the observations. As mentioned previously, the geophysics-based soil map can successfully capture the main variability in soil properties at the km^2 scale and thus the main patterns in soil-controlled water stress and resulting difference in crop development. However, it is not expected that the geophysics-based soil map can reproduce pixel-scale variabilities of LAI_{NDVI} that occur within a single soil-crop unit.

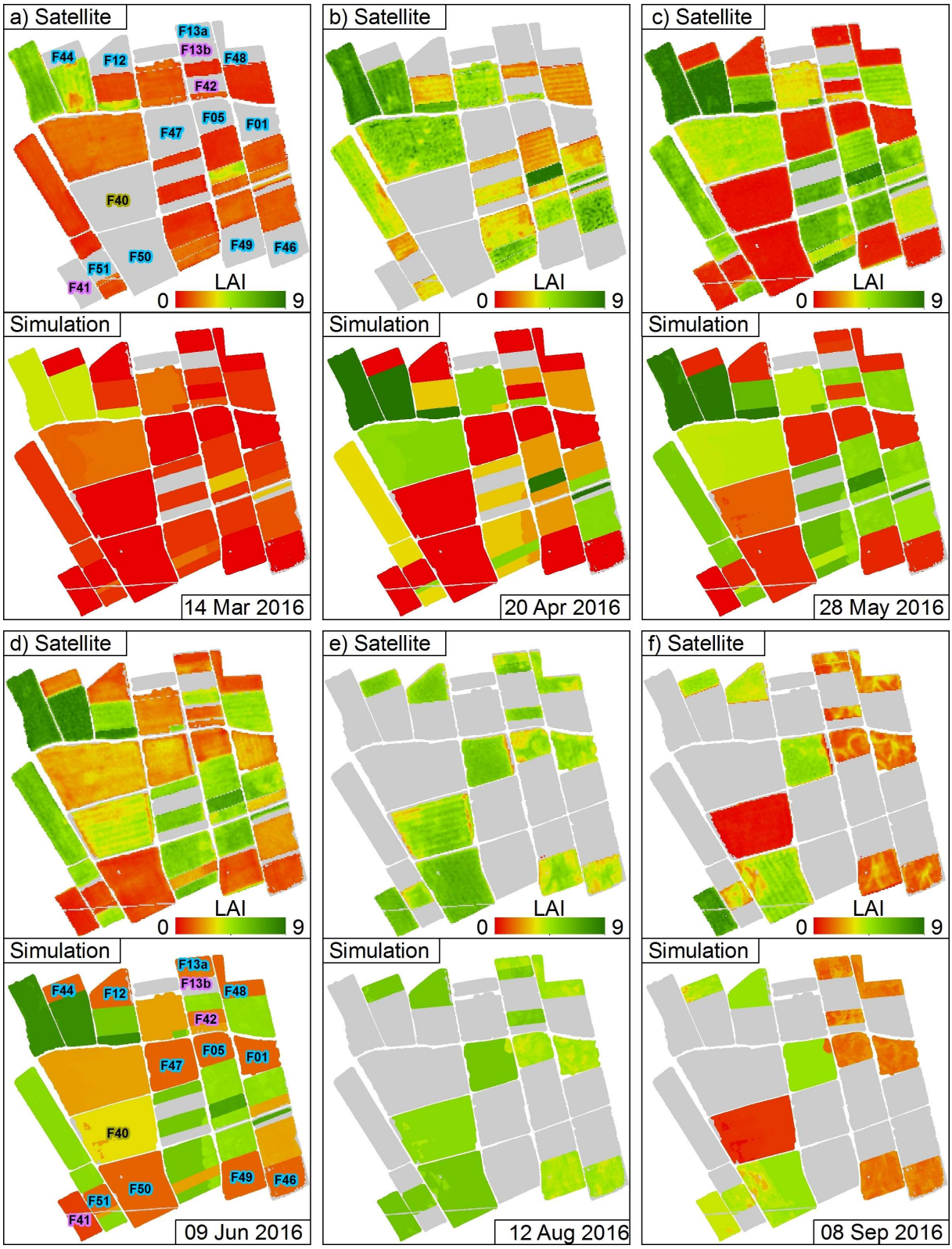

Figure 27: Comparison between observed LAI_{NDVI} (above) and simulated LAI (below) at the a) 14th March, b) 20th April, c) 28th May, d) 9th June, e) 12th August, and f) 8th September 2016.

A lower variability of simulated LAI compared to observed LAI_{NDVI} at the early growth stage of winter rapeseed was also observed (Figure 27a). This might be caused by the absence of

early water stress in the simulation of winter rapeseed (Figure 26a), but it may also be related to within-field management that is not considered in the methodology. The effects of local management are considered to be of secondary importance at the km^2 scale and cannot be meaningfully simulated with typically available information. Similar considerations are valid in the case of within-field variability associated with soil compaction by tractors, which are found in the fields cropped with potato (field F40 in Figure 27d-e) and sugar beet (Figure 27d-f). Overall, the agro-ecosystem simulations for the growing season 2016 were capable of reproducing the growth of the six investigated crops, and the simulated LAI is generally consistent with the LAI_{NDVI} observed in the satellite images.

4.3.4. Crop productivity simulations at the km^2 scale

The productivity at the time of harvest for each soil-crop combination of sugar beet, corn, winter wheat and winter barley is shown in Figure 28. In these maps, a value of 100% represents crops that have grown with optimal water supply for the entire growing season. Lower percentages are shown in the case of water-limited growth and correspond with a lower dry weight at harvest of storage organs (or aboveground biomass in the case of corn) relative to optimal water supply. All four crops achieved a productivity of 100% for the simulations of the BC soil units. For these soils, crops did not experience water stress since the shallow ground water table provided sufficient water to guarantee optimal growth in 2016. On the contrary, a lower productivity was apparent for the soil units with underlying coarse layers. In this case, the productivity of each crop showed a reduction that is largely proportional to the intensity of water stress. The lowest productivity was commonly observed for shallow 2C layers with a large amount of gravels.

The simulated sugar beet productivity at harvest was strongly influenced by soil type and ranged between 58% and 77% in soil units A1a-d, and between 62% and 92% in soil units D1a-d (Figure 28a). Corn simulated in soil units A1a-d (Figure 28b) had a similar range but higher average productivity compared to sugar beet (from 67% to 89%). On the contrary, the corn productivity was much higher than that of sugar beet in soil units D1a-c, and showed much lower variability (from 99% to 100%). For the winter crops, productivity was still influenced by soil type but the impact was generally lower as evidenced by the higher average productivity as compared to the summer crops. In particular, the productivity ranged from 86% to 94% for winter wheat (Figure 28c), and between 81% and 98% in winter barley (Figure 28d).

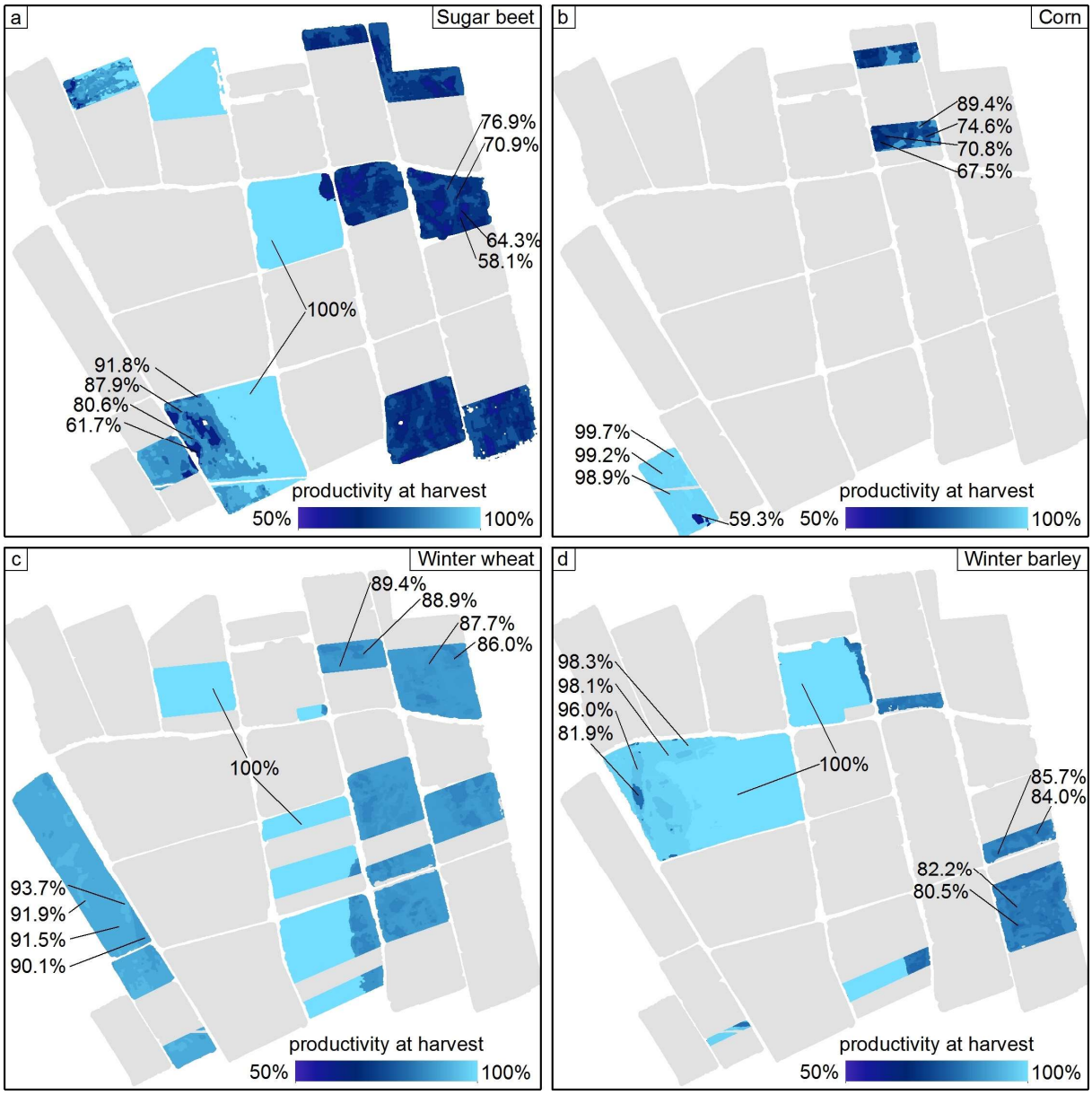

Figure 28: Maps of the simulated productivity at harvest in 2016 of a) sugar beet, b) corn, c) winter wheat, and d) winter barley.

The maps presented in Figure 28 have valuable practical applications in the maximization of agricultural productivity. For example, the selection of specific crop type could be based on the characteristics of the soils that are found in a given field. Furthermore, the seeding date of specific crops could be selected after investigating the precipitation recorded in the previous weeks and the forecasted meteorological conditions. Moreover, the proposed maps and simulation strategy could provide valuable information on the amount and timing of irrigation that is needed to reduce water stress and maximize productivity.

4.4. Conclusions

In this chapter, the growth of six crops in 2016 within a 1x1 km area was simulated using the agro-ecosystem model AgroC by using soil layering and texture that was provided by the high-resolution geophysics-based soil map described in Chapter 3.

The soil hydraulic parameters that are needed as input for the AgroC model were estimated using the pedotransfer function of Rawls and Brakensiek (1985). The simulated water content in two of the soil units was compared to measured soil water content at three depths. It was found that a low RMSE was obtained when the soil profile provided by the geophysics-based soil map well represented the actual soil profile. Additional simulations performed using soil hydraulic parameters estimated with the ROSETTTA pedotransfer function resulted in a much higher RMSE between measured and simulated water content, which was attributed to the higher estimated values of the saturated hydraulic conductivity.

In a next step, agro-ecosystem simulations were performed for six crops: sugar beet, corn, potato, winter wheat, winter barley, and winter rapeseed. In general, it was found that the magnitude of simulated water stress was a function of the crop type and of the soil characteristics. Higher water stress occurred in coarser soils and summer crops. To provide independent data and validate the agro-ecosystem simulations, six leaf area index (LAI_{NDVI}) maps were produced from RapidEye satellite images. Overall, the simulated LAI was found to be consistent with observed LAI_{NDVI} although local inconsistencies between simulations and observations were found (e.g., during the blooming of winter rapeseed, in the case of irrigation, or when the effect of field-scale management was not reproduced). Water stress had an impact on the simulated productivity at harvest for each of the investigated crops. Simulated productivity of sugar beet and winter barley matched the actual harvest in 2016 in two fields within the study area and the simulated productivity of corn and winter wheat corresponded to literature values. Maps of the productivity at harvest were produced for these four crops. These maps consistently showed a productivity reduction in soil units with underlying coarse layers. This reduction was largely proportional to the intensity of water stress.

Overall, this chapter showed that quantitative spatial information on soil heterogeneity derived from geophysics-based soil mapping allowed precise agro-ecosystem simulations of multiple crops on a large area where water stress is strongly influenced by soil characteristics.

The thematic maps produced with the results of these simulations are relevant in practical agricultural applications such as the selection of a specific crop type for a given soil or the selection of the best seeding date for crops that are particularly susceptible to water stress in the early growth stage. For this, additional information could be obtained by considering precipitation recorded in previous weeks or precipitation forecasted by weather models. By extending the simulation period (e.g., 30 years), the proposed strategy could also allow the evaluation of the cost-benefit ratio of long-term strategies such as the most suitable crop rotation. Finally, the proposed maps and simulation strategy might provide valuable insights about irrigation scheduling and quantity by implementing information from forecasted precipitations. A more in-depth discussion of the possible combined use of agro-ecosystem simulations and geophysics-based soil mapping will be provided in Chapter 6.

Chapter 5

Analysis of the added value of geophysics-based soil mapping in agro-ecosystem simulations

In this chapter*, it will be shown that geophysics-based soil mapping provides added value compared to conventional soil maps. In a first step, two commonly available soil maps for the 1 x 1 km study area will be described and a qualitative comparison with the geophysics-based soil map will be provided. In a next step, the growth of five crops that were cultivated in the study area in 2016 will be simulated using the methodology developed in Chapter 4 by using inputs from the geophysics-based soil map and the two commonly available soil maps. Then, the simulations based on each of these maps will be compared to the observed LAI_{NDVI} derived in Chapter 4. It will be shown that the use of inputs from the geophysics-based soil map consistently outperformed the use of the commonly available maps, especially for summer crops and in periods with strong reduction in crop performance. Finally, a more detailed comparison will be presented for sugar beet that includes the simulation of productivity at harvest in one field. Here, the aspects of the soil characterization that are responsible for the poorer performance of the commonly available soil maps will be discussed and the added value of the geophysics-based soil map will be highlighted.

* This chapter is adapted from a journal article in preparation:
Brogi, C., Huisman, J. A., Weihermüller, L., Herbst, M., Klosterhalfen, A., Montzka, C., Vereecken, H., Analysis of the added value of geophysics-based soil mapping in agro-ecosystem modelling.

5.1. Materials and methods

5.1.1. Extent of the analysis within the study area

The LAI simulated with AgroC was compared to the remotely observed LAI_{NDVI} in all fields where corn, sugar beet, winter barley, winter rapeseed, and winter wheat were grown in 2016. Since the potatoes grown in field F-40 were irrigated, this field was excluded from the analysis because the required information to adequately implement this irrigation in AgroC was not available. Therefore, the size of the area in which the comparison was performed totaled 90.4 ha. A detailed analysis was performed in fields where sugar beet (fields F-01, F-05, F13-a, F-46, F-48, and F-49 in the upper terrace and fields F-12, F-47, F-50, and F-51 in the lower terrace) was grown (26.5 ha).

5.1.2. Commonly available soil maps

In this chapter, AgroC simulations were performed using information from two commonly available soil maps: i) the most detailed regional soil map with a scale of 1:5000, which was produced in 1984/85 and revised in 1996 (Röhrig, 1996) and ii) a national soil and yield potential map from 1960 used for the standardization of agricultural taxation (NRW, 1960). The results for these two maps were compared with the results based on the geophysics-based soil map as described in Chapter 4.

The 1:5000 soil map for the study area is shown in Figure 29. This thematic map is part of the official soil inventory of North-Rhine Westphalia and it is broadly used in regional projects such as the preparation of local development or sustainable soil protection plans (NRW, 2018). In this map, the 1:5000 German Land Map (Deutsche Grundkarte) is used as a topographic base. The soil information is obtained from a relatively dense network of augering information where distances between auger positions are typically below 100 m. Each soil unit is provided with information on soil type, grain size distribution (qualitative description), and thickness of the top soil horizons (typically, two horizons are described). The depth of the interface between two overlapping soil horizons is generally represented by a range (e.g., soil unit A-1B in Figure 29 is composed of two horizons and the interface is located between 30 cm and 60 cm depth), which had to be generalized to one depth by taking the average of the maximum and minimum range values. In general, the soil units of the upper terrace are composed of silty loam or loamy sand above sand deposits. In the lower terrace,

silty loam and silt are generally present and sandy material is found locally underlying these deposits. In this map, the study area is divided into 13 soil units ranging from 1.0 to 25.3 ha.

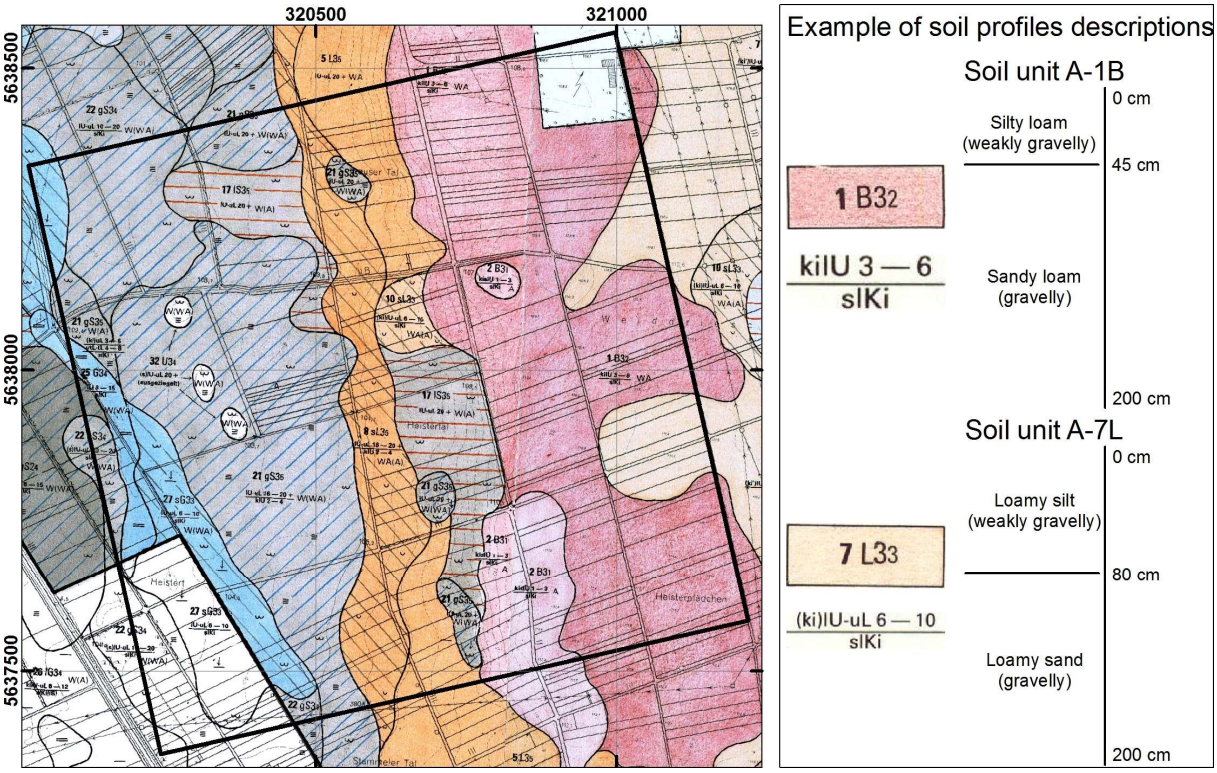

Figure 29: The 1.5000 soil map of the study area with examples of the qualitative description of soil profiles A-1B and A-7L.

The soil taxation map (Karte der Bodenschätzung) for the study area is shown in Figure 30. This map provides estimates of the yield potential of the agricultural land, which is used to calculate tax rates for land owners (NRW, 1960). The estimation of the potential of an agricultural land is based on soil characteristics based on i) soil texture (8 classes), ii) geological age of parent material (4 classes), and iii) overall soil development stage (7 classes). The German Cadaster map is used as the base for the soil information, which was collected by direct sampling with a density of one augering per 40 to 50 m. For each soil unit, the map is provided with soil profile information up to 2.0 m depth. Each profile is divided into multiple horizons (generally four), in which the grain size is qualitatively described. According to this map, the study area generally consists of silty loam soils on top of gravelly sandy loam in the upper terrace. Loamy silt and silty loam are present in the lower terrace and locally found on top of sandy loam. In total, 10 different soil units with an area ranging between 0.7 and 17.5 ha are present in the study area according to this map.

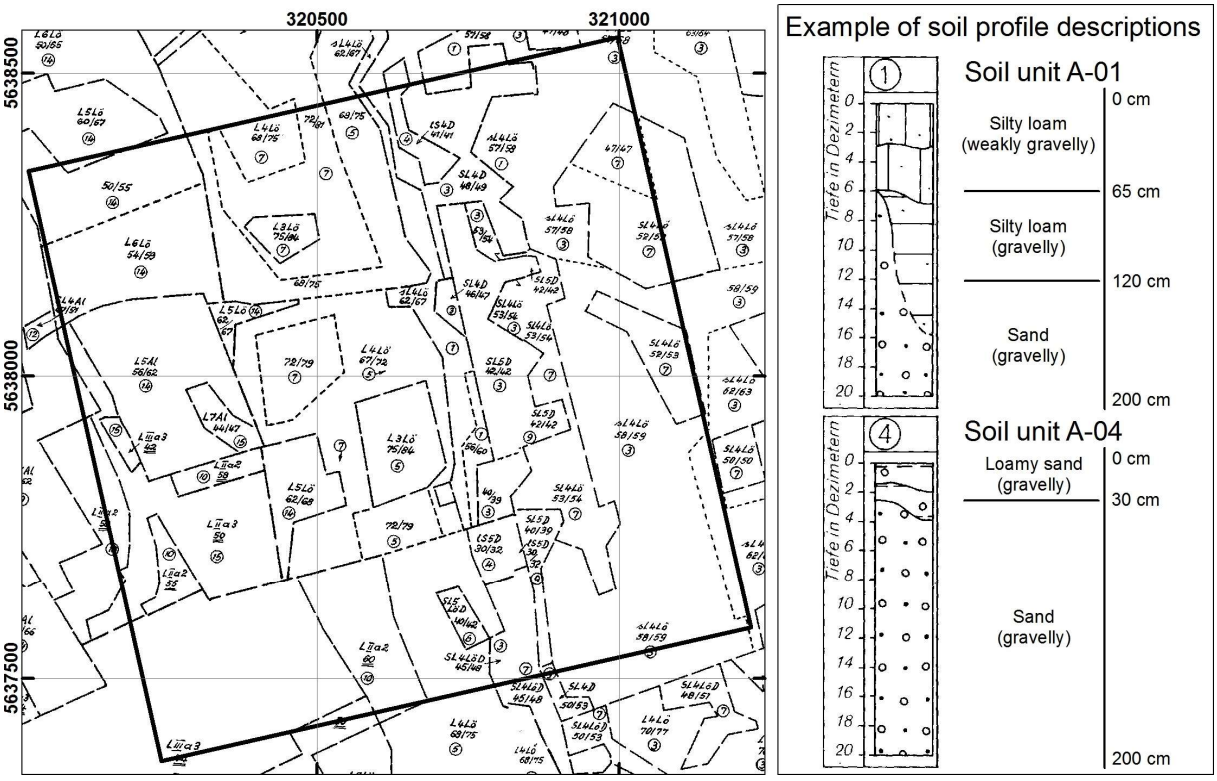

Figure 30: Soil taxation map of the study area and examples of the qualitative description of soil profile A-01 and A-04.

5.1.3. Similarities between sub-areas of the three soil maps

As described in Chapter 3, the geophysics-based soil map divides the study area into four sub-areas A, B, C, and D. However, AgroC simulations in sub-areas B and C were performed with the same crop parameterization and lower boundary conditions of the soil profile, and were described as sub-area BC in Chapter 4. Each soil unit of the two commonly available soil maps generally falls within one of these sub-areas. Therefore, the soil units of these two soil maps were assigned to one of the three sub-areas (A, BC, and D). The unified codes of the soil units of the three soil maps that will be used in this chapter are provided in Table 11.

Table 11: Unified codes of the soil units of the three soil maps following the general separation in sub-areas developed in Chapter 3 and 4.

Soil map	Sub-area A	Sub-area BC	Sub-area D
Geophysics-based soil map	A1a, A1b, A1c, A1d	B1a, B1b, B2a, B2b, B2c, C1a, C1b, C2a, C2b	D1a, D1b, D1c, D1d, D2a
1:5000 Soil map	A-01, A-02, A-03	BC-05, BC-06, BC-07	D-09, D-10, D-14, D-15
Soil taxation map	A-1B, A-2B, A-7L	BC-5L, BC-8sL, BC-10sL, BC-17lS, BC-21gS, BC-32U	D-20sG, D- 22gS, D-25G, D-27sG

5.1.4. Unique soil-crop combinations

The land use information from 2016 (Figure 31a) and the soil units of the two commonly available soil maps were intersected to obtain unique soil-crop combinations for the five investigated crops. This resulted in 42 unique soil-crop combinations for the 1:5000 soil map (figure 3b) and 35 unique combinations for the soil taxation map (figure 3c). The number of soil-crop combinations in the geophysics-based soil map was reduced to 72 after removing potato from the analysis.

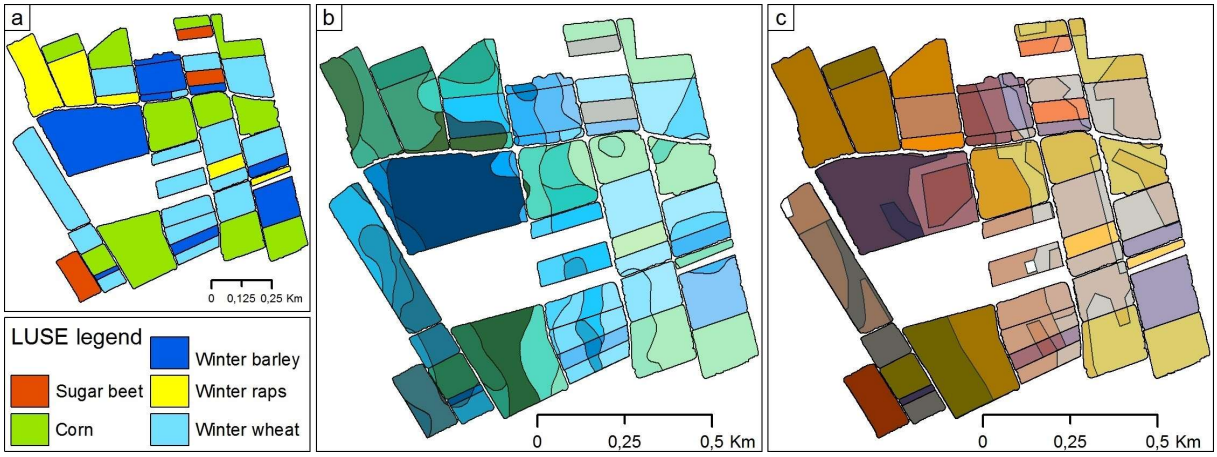

Figure 31: a) Distribution of the five investigated crops, b) unique soil-crop combinations for the 1:5000 soil map, and c) unique soil-crop combinations for the soil taxation map.

5.1.5. Estimation of soil hydraulic parameters

The soil units described in the two commonly available soil maps are provided with a qualitative description of soil texture (soil texture classes). Generally, with such qualitative description, look-up tables are used in land surface modeling (Van Looy et al., 2017) as they provide textural class-average hydraulic parameters (Baker, 1978; Bouma, 1989). However, in Chapter 4, a rather different methodology was used and soil hydraulic parameters were estimated from quantitative texture using the pedotransfer function from Rawls and Brakensiek (1985). To achieve a consistent comparison between the geophysics-based soil map and the commonly available soil maps, the qualitative description provided by the commonly available soil maps was translated in quantitative percentages of sand, silt, and clay content using the USDA soil textural classification (USDA, 2019). For this, the centroid of each soil class within the USDA soil texture triangle was calculated and the associated grain size distribution was determined (Table 12). Afterwards, the percentages of sand, silt,

and clay were used to estimate soil hydraulic parameters by using the pedotransfer function from Rawls and Brakensiek (1985). Occasionally, the presence of gravel is also qualitatively described in the maps. In these cases, 25% volume of gravel was assumed if the maps defined the gravel content as “gravelly” and 10% volume of gravel was assumed if the maps defined the gravel content as “weakly gravelly”.

Table 12: Grain size distribution of the centroid of relevant soil textural classes within the USDA soil texture triangle.

Soil class	Sand (%)	Silt (%)	Clay (%)
Loam	40	40	20
Loamy sand	80	10	10
Loamy silt	25	60	15
Sand	90	5	5
Sandy clay loam	60	10	30
Sandy loam	70	10	20
Silt	5	90	5
Silty loam	22	70	8

After estimation of the grain size distribution, the dry bulk density, BD, was estimated for each horizon following a similar approach as described in Chapter 4. Unfortunately, the depth of the interface between Ap and AB horizons is not provided in the soil profiles of the two commonly available soil maps, which is different from the geophysics-based soil map. Therefore, the first horizon of each soil profile was subdivided into Ap and AB horizons at a depth of 30 cm as commonly observed in the study area. In a next step, a $BD_{<2}$ of 1.30 g cm^{-3} was assigned to the first 30 cm (Ap horizon) and a $BD_{<2}$ of 1.40 g cm^{-3} was assigned to the remaining depth of the first horizon (AB horizon). In deeper and more compacted horizons, a $BD_{<2}$ of 1.50 g cm^{-3} was assigned for fine sediments and a $BD_{<2}$ of 1.60 g cm^{-3} was assigned when the horizons were reported to contain gravel. Following the same procedure as described in Chapter 4, these bulk densities were corrected for gravel content using Equation 12. Finally, the PTF of Rawls and Brakensiek (1985) was used to estimate the soil hydraulic parameters from sand, silt, and clay percentages as well as bulk density and the estimated saturated hydraulic conductivity (K_s) of the coarse horizon in sub-areas A and D was corrected for gravel content according to Brakensiek and Rawls (1994).

The results in Chapter 4 highlighted the importance of the properties of the 2C horizon for the correct simulation of crop productivity within the study area. However, the properties of these

deeper soil horizons were not adequately captured in the two commonly available soil maps. To avoid the introduction of strong and unrealistic variation in the results of the AgroC simulations performed with the different soil maps, the information obtained from the quantitative analysis of the soil sampling campaign performed in 2017 was integrated into the commonly available soil maps. In particular, the soil hydraulic parameters calculated in Chapter 4.2.2 for the 2C horizon in sub-area A and D were used. Therefore, the underlying horizon of the soil units of group A in the commonly available soil maps had the same soil hydraulic parameters as the 2C horizons of soil units A1a-d in the geophysics-based soil map. Similarly, the underlying sediments of the soil units of group D in the commonly available soil maps had the same soil hydraulic parameters as the 2C horizons of the soil units D1a-d and D2a of the geophysics-based soil map.

5.1.6. Set-up of AgroC simulations

The information provided by the commonly available soil maps were used to generate thirteen unique 1-dimensional soil columns for the 1:5000 soil map and ten unique 1-dimensional soil columns for the soil taxation map (i.e., one for each soil unit). As described in Chapter 4, a total of 232 nodes with variable separation were used to discretize each soil column. As for the simulations performed with the geophysics-based soil map, two different set-ups were used for the AgroC simulations. For the soil units of sub-area A and D, the depth of the simulation domain was set from the surface down to a depth of 3 cm into the coarse underlying horizon. Therefore, the depth of the modelling domain ranged from 33 cm to 143 cm in these sub-areas. The maximum rooting depth was set equal to the depth of the fine sediments overlying the coarse horizon. In these profiles, the lower boundary condition was set to free drainage. The second type of set-up was used for soil units of sub-area BC, where fine sediments were present even at larger depth. In this case, the simulation domain extended from the surface down to a depth of 2.0 m and a variable pressure head was used as the lower boundary condition as described in Chapter 4.

The same crop-specific parameters that were used in the simulations based on the geophysics-based soil map were used in the simulations based on the commonly available soil maps, including the differentiations between sub-areas A, BC, and D as described in Chapter 4. Similarly, the upper boundary condition was defined by the same meteorological data as used for the simulations based on the geophysics-based soil map. Finally, the initial pressure head

distribution within each soil profile was determined using the same approach as described in Chapter 4.

5.1.7. Comparison of simulations results

To compare the results of the AgroC simulations performed using information from different soil maps, simulated LAI was compared with observed LAI_{NDVI} calculated from six RapidEye images as described in Chapter 4. First, the mean value of the observed LAI_{NDVI} for each soil-crop combination of the three soil maps was compared with the LAI simulated with AgroC. The root mean square error (RMSE), the model efficiency (ME), and the R^2 coefficient of determination were calculated for each soil map for all six RapidEye images. In a following step, the RMSE, ME, and R^2 were calculated using the simulated LAI and all the observed LAI_{NDVI} values that were located within each soil-crop combination. In the following, we will refer to this comparison as pixel-by-pixel comparison. In this comparison, fields with sugar beet and corn were removed from the analysis for the satellite images collected on the 14th of March and the 20th of April, since the LAI_{NDVI} values of these crops are not reliable at this early growing stage. Similarly, fields with winter barley, winter rapeseed, and winter wheat were removed from the analysis for the 12th of August and the 8th of September since these crops were already harvested at this time. In a final step, a field-by-field analysis of the RMSE of the simulated LAI of the three soil maps for the images taken the 12th of August and 8th of September was performed in fields where sugar beet and corn were grown.

5.2. Results and discussion

5.2.1. Comparison of soil descriptions in the three maps

From a visual comparison, the three soil maps have a similar identification of the limit between the upper and lower terrace that divides sub-area A and BC (Figure 32). In the geophysics-based soil map, this border was identified based on the measured apparent electrical conductivity (ECa) data, whereas the delineation was mainly based on topography and coarse soil augering in the other two soil maps. The location of the border between sub-areas BC and D showed stronger differences between the three maps. In the geophysics-based soil map, this border is again obtained from measured ECa data. Since no clear topographic feature is associated with this border, only the information from augering was available to determine the position of this border in other two maps. This likely also explains why the border between the two sub-areas is locally coincident with the boundary between adjacent

fields. The geophysics-based soil map divides the study area in a larger number of soil units compared to the commonly available soil maps, and also has more complex polygon shapes due to high resolution of the ECa data used to identify the soil units. Generally, a single agricultural field within the study area is described by 4 to 9 soil units in this geophysics-based soil map. The two commonly available soil maps often integrate larger areas in one soil unit, and therefore single fields are often described by only one soil unit.

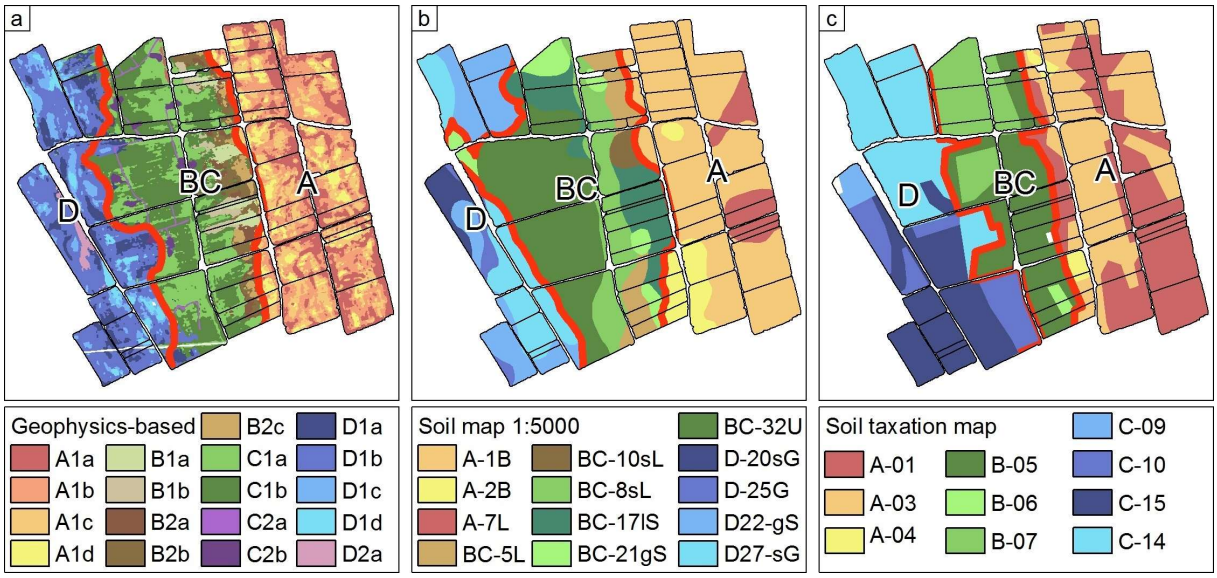

Figure 32: Distribution of soil units and of sub-areas A, BC, and D in a) the geophysics-based soil map, b) the 1:5000 soil map, and c) the soil taxation map.

The majority of the shallow soils within the study area are described by silty loam and loamy silt above coarser sediments in the commonly available soil maps. Figure 33 shows the percentages of sand and silt at 30cm depth in the three soil maps. The grain size distribution obtained from this qualitative description using Table 12 was generally similar to the one obtained by the quantitative analysis of the soil samples described Chapter 3. For example, the areas classified as loamy silt were estimated to have 25% sand, 60% silt, and 15% clay based on Table 12, whereas the range of values determined from the soil samples in this area was 13-24% sand, ~56-70% silt, and ~13-23% clay. The estimated grain size distribution for silty loam (22% sand, 70% silt, and 8% clay) differed more from the range of values obtained from the above mentioned laboratory results, but still is in reasonable agreement. The underlying coarse material in sub-areas A and D were classified as sand or sandy clay loam in the 1:5000 soil map and sandy loam or loamy sand in the soil taxation map. For these four soil textural classes, the sand fraction obtained from Table 2 is much higher than the values obtained from the laboratory analysis of the soil samples (60-90% sand compared to ~28-58%

for the laboratory data). As a consequence, the percentage of silt is much lower (5-10% silt compared to ~30-54% for the laboratory data). These textural differences are also apparent in in Figure 33 where the percentages of sand and silt at 150 cm depth in the three soil maps are shown.

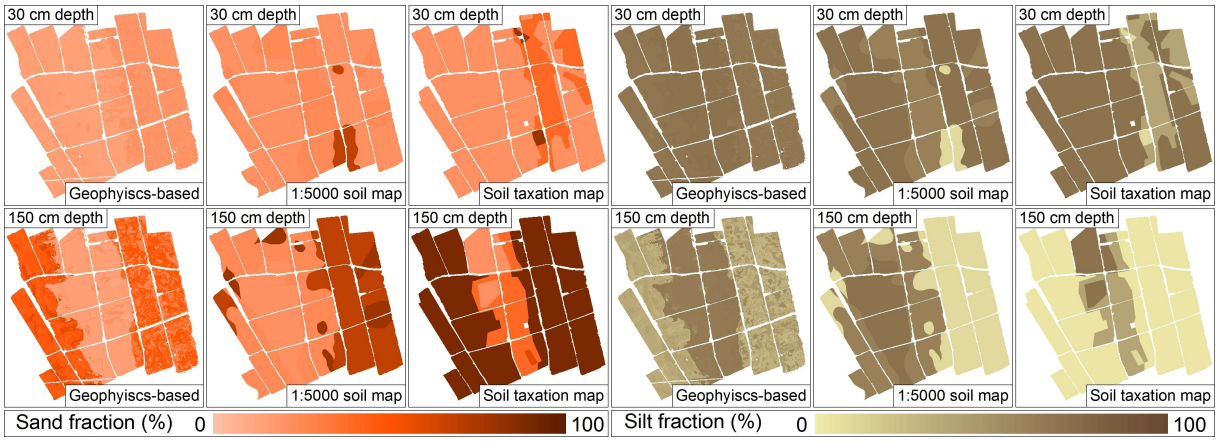

Figure 33: percentages of sand (orange color scale) and silt (brown color scale) at 30 cm and at 150 cm in the three soil maps.

Figure 34 shows the saturated hydraulic conductivity (K_s) and the saturated water content (θ_s) at 30 cm and at 150 cm depth in the three soil maps which were obtained from soil texture and estimated bulk density. Generally, the values of K_s and θ_s at 30 cm depth are rather similar in the three maps. The same applies to the values at 150 cm depth in sub-area BC. On the contrary, within sub-areas A and D, the values of K_s and θ_s at 150 cm depth are much higher in the commonly available soil maps compared to those of the geophysics-based soil map.

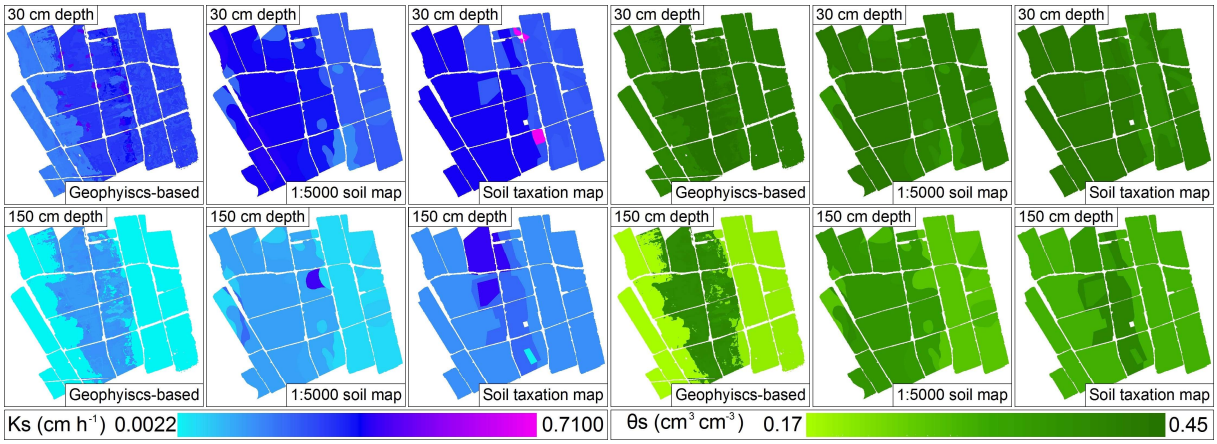

Figure 34: estimated saturated hydraulic conductivity (blue color scale) and saturated water content (green color scale) at 30 cm and at 150 cm in the three soil maps.

Overall it was concluded that the top soil was reasonably well described by the commonly available soil maps, whereas the description of the underlying coarse horizons did not match well with the soil texture determined from laboratory analysis.

The depth to the coarse 2C horizon varied between 49 and 86 cm in sub-area A and between 47 and 134 cm in sub-area D in the geophysics-based soil map. As described in the previous chapters, the depth of this coarse horizon has a strong effect on crop water stress and crop performance. In the 1:5000 soil map, the depth to this horizon ranged between 30 (soil unit A-2B) and 80 cm (soil unit A-7L) in sub-area A, and between 80 (soil unit D-27sG) and 150 cm (soil unit D-22gS) in sub-area D. In the soil taxation map, this depth ranged between 30 and 120 cm (soil units A-04 and A-01) in sub-area A and between 105 (soil unit D-10) and 140 cm (soil units D-09, D-10, and D-15) in sub-area D. Generally, it was found that this important depth was better represented by the 1:5000 soil map than by the soil taxation map. However, it is important to realize that the spatial distribution of the depth to this horizon is as essential as its depth for adequate prediction of patterns in crop productivity.

5.2.2. Performance of LAI simulations

Figure 35 shows the results of a comparison between simulated LAI and observed RapidEye LAI_{NDVI} for the different soil maps. For this comparison, we used the mean LAI_{NDVI} value within each soil-crop combination at the six dates of the RapidEye images.

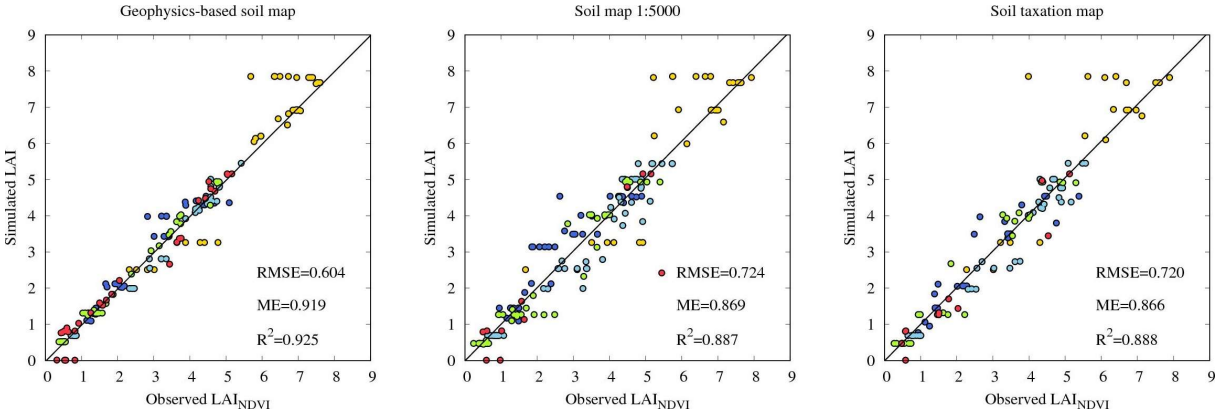

Figure 35: Simulated LAI and mean LAI_{NDVI} value within each soil-crop combination for simulations based on the a) geophysics-based soil map, b) the 1:5000 soil map, and c) the soil taxation map for all six available RapidEye images.

The values obtained by the AgroC simulations based on the inputs from the geophysics-based soil map (RMSE = 0.604, ME = 0.919, and R^2 = 0.925) showed an improvement compared to the simulation results based on the commonly available soil maps (RMSE = 0.724, ME = 0.869, and R^2 = 0.887 for the 1:5000 oil map and RMSE = 0.720, ME = 0.866, and R^2 = 0.886 for the soil taxation maps). However, this improvement is relatively small and the results for the two commonly available soil maps could also be considered to be satisfactory. These similarly good results are due to the simultaneous use of all simulated crops and dates and to the fact that the comparison is performed using the mean value of each soil-crop combination, thus reducing the influence of the naturally occurring pixel-scale variability of LAI_{NDVI}. In a next step, simulated LAI and the mean LAI_{NDVI} value within each soil-crop combination were compared separately for each RapidEye image. The results of this comparison are summarized in Table 13.

Table 13: RMSE, ME, and R^2 between simulated LAI and the mean of observed LAI_{NDVI} within each soil-crop unit for the three soil maps. The best performing result at each date are marked in bold.

	Geophysics-based map			**1:5000 Soil map**			**Soil taxation map**		
Date	**RMSE**	**ME**	**R^2**	**RMSE**	**ME**	**R^2**	**RMSE**	**ME**	**R^2**
14th Mar	**0.465**	**0.867**	**0.953**	0.628	0.752	0.816	0.512	0.733	0.818
20th Apr	**0.777**	**0.785**	**0.945**	1.309	0.199	0.751	1.708	-0.464	0.539
28th May	**0.333**	**0.983**	**0.985**	0.696	0.917	0.929	0.940	0.838	0.867
09th Jun	**0.198**	**0.991**	**0.992**	0.646	0.891	0.904	0.652	0.882	0.910
12th Aug	**0.185**	**0.906**	**0.943**	0.437	0.394	0.752	0.499	0.146	0.418
08th Sep	**0.732**	**0.701**	**0.773**	0.887	0.305	0.491	0.892	0.358	0.479

First, it should be noted that the geophysics-based soil map showed lower RMSE, higher ME, and higher R^2 for all individual dates, and thus also outperformed the two other soil maps in this analysis. However, it also becomes apparent that the three soil maps performed similarly well in March, May, and June. In April, the geophysics-based soil map outperformed the commonly available soil maps, although there was a general decrease in performance for all three maps. This might be related to the high variability in LAI_{NDVI} in different agricultural fields that is caused by the uncertainty in seeding and emergence dates of winter barley, winter rapeseed, and winter wheat. Moreover, the blooming of winter rapeseed affected the estimated LAI_{NDVI} as discussed in Chapter 4, and this may also have reduced the performance in April for all three soil maps. A second drop in the performance of the three soil maps was apparent in August for the 1:5000 soil map and the soil taxation map and in September for all three maps (Table 13). At this stage, corn and sugar beet were the only crops present and the

reduced correlation is likely caused by the appearance of crop stress that increased the spatial variability in LAI_{NDVI}. In this stressed situation, the geophysics-based soil map clearly outperformed the other soil map.

5.2.3. Pixel-by-pixel comparison of LAI simulation

Figure 36 shows the pixel-by-pixel comparison between simulated LAI and observed LAI_{NDVI}. Here, the highest density of pixels (in red) is close to the regression line in the case of the geophysics-based soil map, and showed more spread for the commonly available soil maps. This is also reflected in the error measures, which were slightly better for the geophysics-based soil map (RMSE = 0.747, ME = 0.859, and R^2 = 0.866) than those for the 1:5000 soil map (RMSE = 0.823, ME = 0.829, and R^2 = 0.842) and considerably better than those for the soil taxation map (RMSE = 1.166, ME = 0.655, and R^2 = 0.723). This comparison includes the values of each single cell of the LAI_{NDVI} dataset and is therefore different from the previous comparison in which only the mean LAI_{NDVI} of each soil-crop combination was used. As discussed in Chapter 4, the values of LAI_{NDVI} locally show a rather strong variability within single soil-crop combinations. This variability is responsible for the lower values of RMSE and higher values of ME and R^2 compared to the previous comparison that made use of the average LAI_{NDVI}.

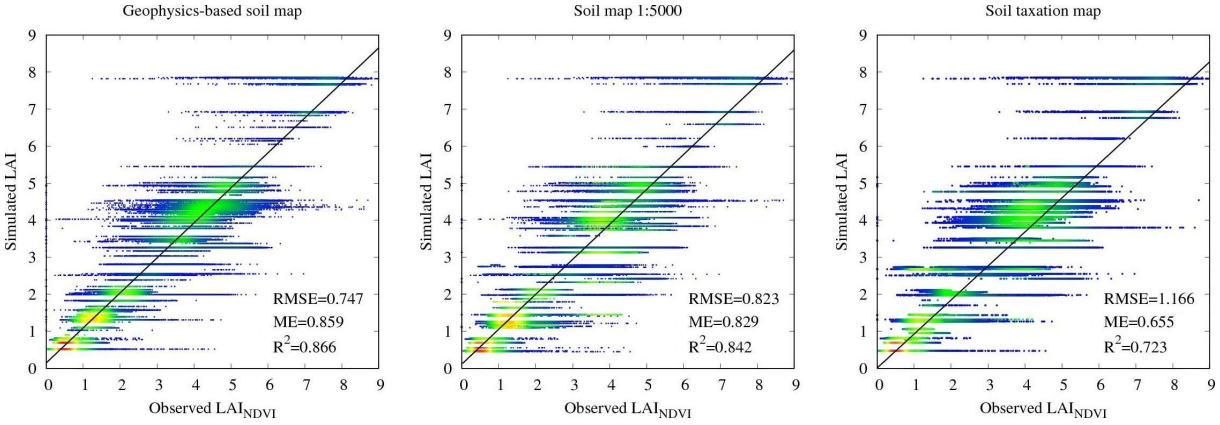

Figure 36: Pixel-by-pixel comparison between simulated LAI and observed LAI_{NDVI} for a) simulation based on the geophysics-based soil map, b) the 1:5000 soil map, and c) the soil taxation map. The color indicates the density of events with red being the most dense and blue the less dense.

Table 14 summarizes the pixel-by-pixel performance for all three soil maps for each RapidEye image. As in the case of the comparison of the mean values per soil-crop unit, the three soil maps performed well in March, May, and June. However, the higher performance of the geophysics-based soil map in comparison to the commonly available soil maps is more

apparent in this pixel-by-pixel analysis. In April, the geophysics-based soil map (RMSE = 1.10, ME = 0.55, and R^2 = 0.72) and the 1:5000 soil map (RMSE = 1.14, ME = 0.51, and R^2 = 0.70) showed similar performance and provided more accurate simulations than the soil taxation map (RMSE = 1.87, ME = -0.32, and R^2 = 0.43). In August and September, a strong drop in performance was observed for all three soil maps due to the increased spatial variability of LAI_{NDVI} that was not fully captured by the simulations. However, the geophysics-based soil map again outperformed the other soil maps with an increasing difference in performance towards the end of the growing season.

Table 14: RMSE, ME, and R^2 of the pixel-by-pixel comparison between simulated LAI and the observed LAI_{NDVI} within each soil-crop unit for the three soil maps. The best performing result at each date are marked in bold.

	Geophysics-based map			**1:5000 Soil map**			**Soil taxation map**		
Date	**RMSE**	**ME**	**R^2**	**RMSE**	**ME**	**R^2**	**RMSE**	**ME**	**R^2**
14th Mar	**0.619**	**0.761**	**0.836**	0.651	0.737	0.793	0.807	0.595	0.687
20th Apr	**1.095**	**0.546**	**0.715**	1.137	0.511	0.701	1.868	-0.321	0.434
28th May	**0.662**	**0.924**	**0.925**	0.676	0.921	0.923	1.0146	0.772	0.808
09th Jun	**0.653**	**0.883**	**0.887**	0.686	0.871	0.878	0.929	0.764	0.812
12th Aug	**0.852**	**0.326**	**0.337**	1.047	-0.019	0.257	0.886	0.271	0.282
08th Sep	**0.786**	**0.646**	**0.649**	1.073	0.340	0.446	1.114	0.289	0.340

5.2.4. Simulation of sugar beet

In a next step, simulations of sugar beet are analyzed in more detail. This crop was selected because of its importance in the study area (31.7% of the investigated area) and because the difference in performance between the three soil maps was strongest in August and September when this crop was still growing.

5.2.4.1 LAI simulation at the km² scale

Figure 37 shows the LAI_{NDVI} determined from Rapid Eye images and the simulated LAI based on the soil input from the three soil maps on the 9th of June, 12th of August, and 8th of September in fields where sugar beets were grown. On the 9th of June, LAI_{NDVI} showed high variability between fields that was mainly caused by differences in seeding date or field management (Figure 37a). As discussed in Chapter 4, the modelling set-up that was used in this chapter is not capable of reproducing this variability at this stage of crop development. On the 12th of August, the LAI_{NDVI} of sugar beet reached the maximum observed value in sub-area BC and water stress affected the development of crops growing in sub-area A. On the 8th

of September (Figure 37c), water stress affected the development of sugar beet in both sub-area A and sub-area D.

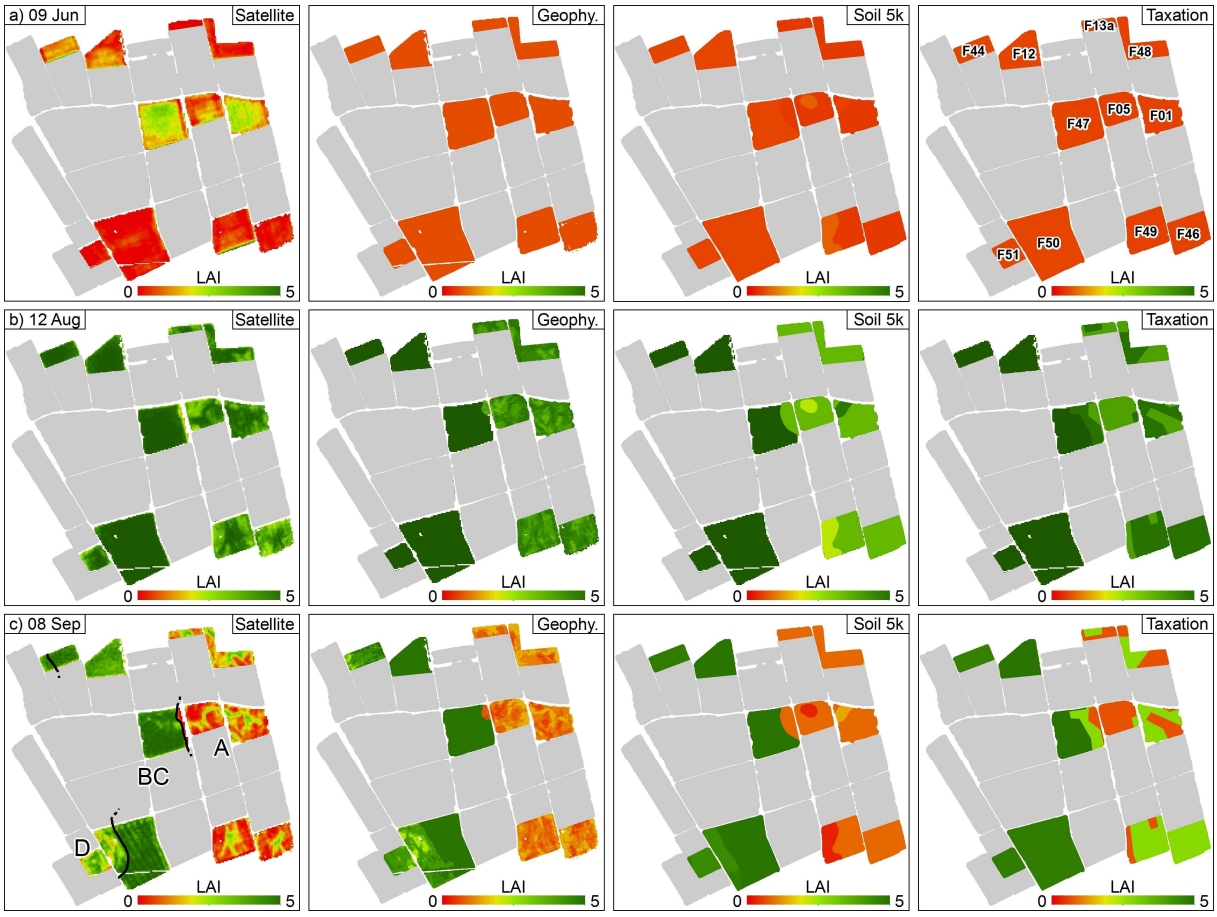

Figure 37: Satellite observed LAI_{NDVI} and simulated LAI using the geophysics-based soil map (Geophy.), the 1:5000 soil map (soil 5k), and the soil taxation map (Taxation); a) shows the codes of the investigated fields and c) shows the geometry of sub-areas A, BC, and D. The comparison is shown for the following dates: a) the 9th June, b) 12th August, and c) 8th September 2016.

The simulated LAI obtained using the geophysics-based soil map captured the correct location of the borders between sub-areas A, BC, and D, which were also clearly detected in the LAI_{NDVI}. In the case of the 1:5000 soil map, the border between sub-area A and sub-area BC was well represented. This was not the case for the border between sub-area BC and sub-area D since the simulated LAI was very similar for these two sub-areas. In the case of the soil taxation map, the border between sub-area A and BC was well represented, whereas no visible subdivision between sub-area BC and D was obtained using inputs from this map because of the absence of simulated water stress in sub-area D that did not result in a meaningful reduction of simulated LAI.

The patterns in simulated LAI within each sub-area obtained using the geophysics-based soil map matched well with the patterns in LAI_{NDVI} at the 12th of August and at the 8th of September. As discussed in Chapter 4, the variability of LAI_{NDVI} was not fully represented by the simulations based on the geophysics-based soil map as the simulation approach with soil-crop units cannot capture pixel-scale variabilities in LAI_{NDVI} that occur within a single soil unit. In contrast, simulations based on the other two soil maps did not result in representative patterns of simulated LAI within each sub-area.

Table 15 summarizes the RMSE between simulated and observed LAI for individual fields (see Figure 37a) where sugar beet was grown at the 12th August and at the 8th September for all three soil maps. Generally, these 14 fields can be divided in three groups according to the RMSE obtained for the different soil maps. The first group is composed of fields F-01, F-05, F13a, F-48, and F-49 that are located within sub-area A. In these fields, the geophysics-based soil map showed a lower RMSE in August and September compared to the simulations based on the two other soil maps. The only exception was field F-46 in August, where the lowest RMSE of 0.53 was obtained for the 1:5000 soil map. In some cases, the reduction of RMSE between the simulations of the geophysics-based soil map and the other soil maps was rather limited, such as in field F-48 or field F-49. Nevertheless, the reduction in RMSE obtained using the simulations based on the geophysics-based soil map was apparent for both days and increased in September.

The second group is composed of fields F-12, F-44, and F-47 that are located in sub-area BC, where no water stress was simulated. In this group, there was no general indication on which soil map provided the lowest RMSE. In particular, field F-12 showed the same RMSE irrespective of the soil map used as input, whereas fields F-44 and F-47 showed lower and similar RMSE when the geophysics-based soil map or the soil taxation map were used. The third group is composed of fields that are generally located in sub-area D (fields F-50 and F-51). The RMSE of the simulations performed using the three soil maps were rather similar in August, whereas the geophysics-based soil map outperformed the simulations based on the other two maps in September. Here, it has to be noted that water stress observed in sub-area D was rather low in August and had a stronger effect on sugar beet growth in September.

Table 15: Table of RMSE error of LAI simulation in fields cropped with sugar beet and corn. The best performing result at each date are marked in bold.

Field	12th August			8th September		
	Geophysics-based soil map	1:5000 Soil map	Tax. map	Geophysics-based soil map	1:500 Soil map	Tax. map
F-01	**0.78**	1.01	0.81	**0.49**	0.56	0.96
F-05	**0.78**	0.99	0.82	**0.45**	0.50	0.57
F-13	**0.57**	0.76	0.62	**0.57**	0.73	0.73
F-46	0.65	**0.53**	0.93	**0.43**	0.45	1.27
F-48	**0.79**	1.07	0.80	**0.65**	0.80	0.94
F-49	**0.80**	1.07	0.84	**0.49**	0.50	1.16
F-12	1.01	1.01	1.01	0.96	0.96	0.96
F-44	**1.10**	1.14	1.11	0.90	0.86	**0.84**
F-47	0.87	0.83	**0.76**	**0.82**	0.92	0.88
F-50	0.76	0.75	**0.71**	**0.63**	0.76	0.75
F-51	**1.37**	1.40	1.37	**1.06**	1.29	1.41

All in all, it is apparent how the improvements in simulation of sugar beet provided by the geophysics-based soil map are strongly dependent on the amount and timing of water stress. The results of the simulations based on the three soil maps were rather similar in areas and periods in which water stress is not affecting crop development. In periods with significant water stress, the RMSE obtained for simulations based on the geophysics-based soil map was 2% to 74% lower than the RMSE obtained with the other soil maps. Additionally, this reduction in RMSE varied substantially from field to field, likely because of differences in quality of the soil characterization provided by the three soil maps.

5.2.4.2 AgroC simulations of sugar beet in sub-area A

Figure 38a-c shows the simulated LAI based on the input from the three soil maps (lines) and the observed LAI_{NDVI} (dots) for sugar beet grown on the soil units of sub-area A. Figure 38d-f shows the related water stress simulated with AgroC in each soil-unit of sub-area A. As described in Chapter 4, the simulations based on the input from the geophysics-based soil map well matched the observed LAI_{NDVI}. The four soil units A1a-d showed nearly the same LAI values early in the growing season (28th May and 9th June) and differed in simulated LAI later in the growing season (12th August and 8th September) due to different amounts of water stress occurring in each soil unit.

In the case of the 1:5000 soil map, the LAI simulated for the three soil units well matched the observed LAI_{NDVI} in May and June with the exception of soil unit A-07L that underestimated observed LAI_{NDVI}. In August and September, soil unit A-07L well matched the observed LAI_{NDVI}, whereas the other two soil units underestimated observed LAI_{NDVI}. The mismatch between simulated and observed LAI for the soil units A-01B and A-02B is due to assumed shallow depth to the coarse sediments, which was 30 cm in soil unit A-02B, 45 cm in unit A-1B, and 80 cm in unit A-7L. As previously discussed, the depth to this coarse sediment has a strong influence on the timing and intensity of water stress. Since the uppermost soils had similar soil physical properties in the descriptions provided by the three soil maps, it can be concluded that the reduced match between simulations and observations was due to an underestimation of the depth to the coarse sediments in soil units A-01B and A-02B that caused stronger water stress due to lower water availability.

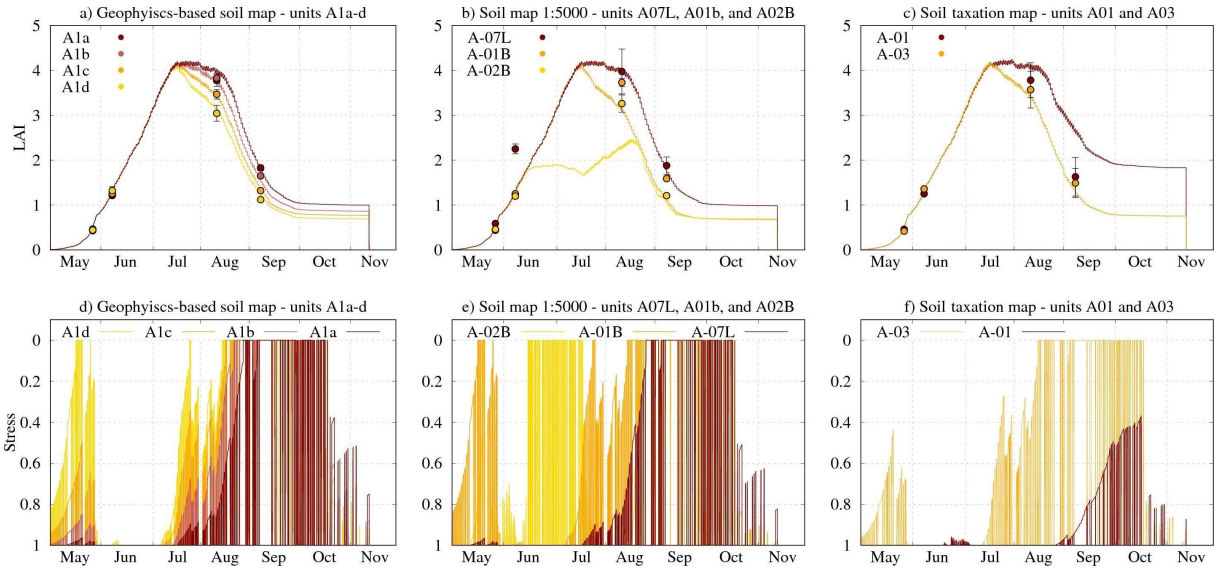

Figure 38: Observed LAI_{NDVI} (dots) of sugar beet in sub-area A compared to the LAI (lines) as well as corresponding stress occurrence simulated using input from a,d) the geophysics-based soil map, b,e) the 1:5000 soil map, and c,f) the soil taxation map.

In the case of the soil taxation map, the observed LAI_{NDVI} for the two soil units were rather similar. This suggests that the distribution of the two soil units did not capture differences in crop performance that are apparent in the satellite images. The depth to the coarse sediment in the two soil units was 120 cm in A-01, and 70 cm in A-03, respectively. Again, the uppermost soils horizons had similar soil physical properties compared to the soil units of the geophysics-based soil map. Due to the higher water availability in soil unit A-01 because of

the overestimation of the soil depth, the simulated LAI overestimated measured LAI_{NDVI}. The actual depth was better captured for soil unit A-03, thus leading to improved LAI simulations.

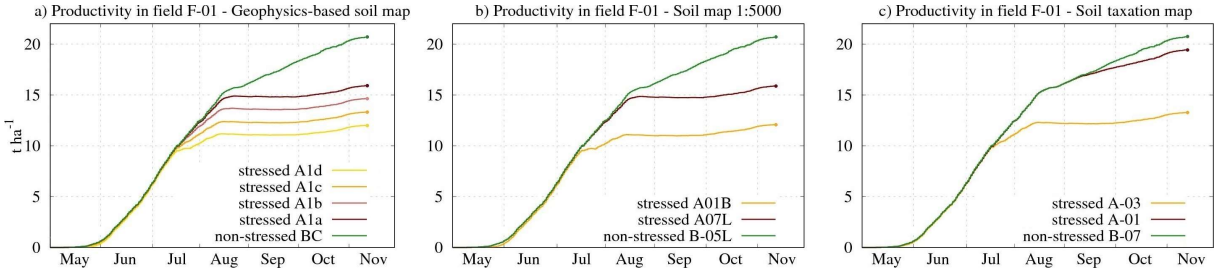

Figure 39: Productivity at harvest of the soil units of field F-01 simulated with inputs from a) the geophysics-based soil map, b) the 1:5000 soil map, and c) the soil taxation map. The productivity of sugar beet simulated on soil units without water stress is also provided in green.

Figure 39a-c shows the development of sugar beet biomass over time (expressed in t ha^{-1} of dry beets) simulated for sub-area A based on inputs from the three soil maps. All simulations based on the three soil maps showed reduced biomass development due to water stress from July until harvest compared to the non-stressed soil-crop combinations of sub-area BC. The total simulated productivity at harvest of sugar beet in field F-01 based on simulations with inputs from the geophysics-based soil map was 14.3 t ha^{-1}. As described in Chapter 4, this value matched well the actual total productivity recorded in this field (14.2 t ha^{-1}). The simulated productivity based on the 1:5000 soil map was 15.4 t ha^{-1}, which was an 8% overestimation of the actual productivity. In the case of the soil taxation map, the simulated productivity was 17.3 t ha^{-1} (+21%).

5.2.4.3 AgroC simulations of sugar beet in sub-area D

Figure 40a-c shows the simulated LAI (lines) and observed LAI_{NDVI} (dots) for sugar beet growing on the soil units of sub-area D for all three soil maps and Figure 40d-f shows the associated simulated water stress. As in sub-area A, the simulations based on the geophysics-based soil map matched well with the observed LAI_{NDVI} with the exception of soil unit D1d where the simulated LAI underestimated observed LAI_{NDVI} in August.

In the case of the 1:5000 soil map, the simulated LAI for the soil units D-22G and D-27G were similar in May, June, and August, and matched well with the observed LAI_{NDVI}. In September, simulated LAI of soil unit D-22G also matched well the observed LAI_{NDVI} but the simulated LAI for soil unit D-27G clearly overestimated LAI_{NDVI} because of the low amount

of simulated water stress. In this case, the upper depth to the coarse sediments for soil unit D-27G (80 cm) was similar to the depth to the coarse sediments in soil unit D1c of the geophysics-based soil map (83 cm). However, the simulated LAI for these soil units differed strongly because of differences in simulated water stress. This is caused by different soil hydraulic parameterizations of the uppermost horizons between these two soil units. In fact, the saturated water content of the uppermost horizons is generally higher in D-27G (between 0.434 and 0.396 cm^3 cm^{-3}) than in D1c (between 0.404 and 0.364 cm^3 cm^{-3}). At the same time, residual water content is lower in D-27G (between 0.037 and 0.021 cm^3 cm^{-3}) compared to D1c (between 0.072 and 0.066 cm^3 cm^{-3}). These differences in soil hydraulic parameters are due to differences in estimated soil texture, which was derived through laboratory analysis for the geophysics-based soil map and qualitatively described through hand texturing for the 1:5000 soil map. It is true that the above described difference in soil hydraulic parameters of these two maps is rather subtle compared to those occurring in coarser and deeper soils. Nevertheless, the result of this different parameterization is a generally higher plant available water content in D-27G compared to D1c.

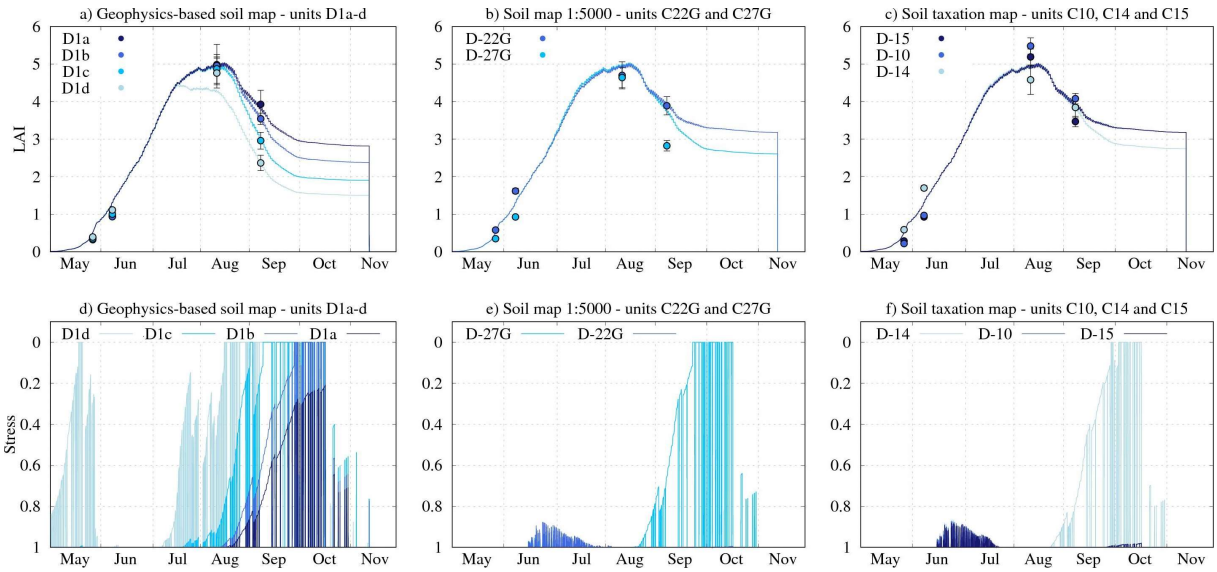

Figure 40: Observed LAI_{NDVI} (dots) of sugar beet in sub-area D compared to the LAI (lines) as well as corresponding stress occurrence simulated using input from a,d) the geophysics-based soil map, b,e) the 1:5000 soil map, and c,f) the soil taxation map.

Finally, Figure 40c,f shows the simulation results based on the input from the soil taxation map. As for the 1:5000 soil map, the simulated LAI in the three soil units D-10, D-14, and D-15 showed rather similar values in May, June, and August. In September, the simulated LAI of soil units D-10 and D-15 was again similar because the soil description provided by the soil

taxation map is identical for these two soil units. In contrast, the occurrence of simulated water stress in soil unit D-14 caused a reduction in simulated LAI compared to the other two soil units. Overall, the simulated LAI in the soil units of the soil taxation map did not match well the observed LAI_{NDVI}. This was attributed to two main factors. First, the depth to the coarse sediments ranged from 105 to 140 cm for the soil units of the soil taxation map. This depth is much larger than the depths obtained for the other two soil maps, thus reducing water stress in the simulations performed with inputs based on the soil taxation map. Second, the extent of sub-area D in the soil taxation map differed from the extent of the same sub-area in the other two soil maps (Figure 32). In particular, fields that are located in sub-area BC in the geophysics-based soil map and in the 1:5000 soil map were located in sub-area D in the soil taxation map. The fields within sub-area BC did not show water stress and thus have the highest LAI_{NDVI} values. Therefore, the inclusion of these areas in sub-area D resulted in higher observed LAI_{NDVI} in the soil taxation map that was not captured by the simulations.

Throughout the studied area, the magnitude of the reduction in performance of the two commonly available soil maps compared to geophysics-based soil map depended on local soil characteristics. Generally, this reduction was caused by a poor representation of the depth of coarse sediments, of the texture of the overlying fine sediments, and of the subdivision between large sub-areas that have different soil characteristics. The different quality of this soil representation had an impact not only on the quality of the simulation of LAI but also on simulation of crop productivity at harvest.

5.3. Conclusions

In this chapter, the agro-ecosystem simulations performed in Chapter 4 by using inputs from the geophysics-based soil map obtained in Chapter 3 were compared with simulations performed by using inputs of two commonly available soil maps. These two maps are provided with a qualitative description of the soil texture, which was converted to quantitative percentages of the grain size distribution using the USDA soil texture triangle. The three maps showed a comparable subdivision of the study area in three sub-areas A, BC, and D, (already described in the previous chapters). However, substantial differences were found in the location of the boundary between sub-area BC and D. The soil texture for the top soil was found to be similar in the three maps. On the contrary, the textural information of the underlying coarse horizons differed significantly.

In a next step, the growth of corn, sugar beet, winter barley, winter rapeseed, and winter wheat was simulated with the agro-ecosystem model AgroC. The simulated LAI obtained by the agro-ecosystem simulations was compared with observed LAI_{NDVI} determined from RapidEye images using the root mean square error (RMSE), the model efficiency (ME), and the explained variance (R^2). This analysis showed that the simulations performed with inputs from the geophysics-based soil map consistently resulted in lower RMSE and higher ME and R^2 and thus outperformed the simulations obtained by using inputs from the two commonly available soil maps. However, the improvement in simulation quality was subtle for winter crops and periods with limited water stress. In contrast, the simulations based on the geophysics-based soil map clearly outperformed the commonly available soil maps in periods with moderate to high water stress that caused a reduction in crop performance. This was particularly evident for corn and sugar beet.

A more detailed evaluation was performed using the AgroC simulations for sugar beet. It was found that the geophysics-based soil map clearly outperformed the commonly available soil representations in areas where stronger water stress was observed. This improved performance obtained with the geophysics-based soil map were locally caused by a more accurate depth to the coarse sediments, by a more accurate description of the soil texture of the overlying horizons, and by a more precise subdivision of the four sub-areas that are found in the study area. These aspects also had an impact on the simulation of the productivity at harvest where the geophysics-based soil map again outperformed the commonly available soil maps. However, these potential improvements in simulated productivity at harvest should be validated more extensively in future work since simulated and actual productivity were compared in one field only in this thesis.

Overall, it was found that the geophysics-based soil characterization provides an added value to agro-ecosystem modelling and allows for better simulation of crop LAI and crop productivity. However, improvements were more apparent when prolonged periods of drought resulted in reduced crop performance. At the same time, improvements depended on the combination of soil characteristics and crop type. Nevertheless, a substantial mismatch with observations was observed in the simulations obtained by using the two commonly available maps. A detailed and quantitative soil characterization such as the geophysics-based soil map can thus have long term utility in an agricultural environment and can enable the use

of advanced farming techniques and strategies that are not practicable when solely based on general-purpose soil maps.

Chapter 6

Conclusions and outlook

In this chapter, the overall conclusions of this thesis will be presented and further research questions and gaps in knowledge arising from the elaborated topics will be discussed in an extensive outlook.

6.1. Final conclusions

It is already well established that electromagnetic induction (EMI) measurements are valuable for the characterization of the shallow subsurface because EMI is a non-invasive geophysical technique that allows to collect a large amount of data with a rather limited consumption of time and resources. Nevertheless, only a few studies have made use of EMI to produce high-resolution soil maps beyond the scale of a single field. Furthermore, the added value of such geophysics-based soil representations within the context of agro-ecosystem modelling of multiple crops has not been demonstrated yet. This was the challenging starting point of the work presented in this thesis.

In Chapter 3, it was shown that multi-configuration EMI measurements can be used to obtain a high-resolution geophysics-based soil map of a large and heterogeneous agricultural area of 1 x 1 km. Here, the collection of detailed EMI measurements resulted in a total of nine apparent electrical conductivity (ECa) maps with an increasing depth of investigation. Despite the application of a temperature correction, the ECa maps clearly showed changes in ECa between fields due to different water content and land management (crop type, fertilization, etc.). This heterogeneity was present because EMI data acquisition was performed field-by-field and over a period of six months as a consequence of the combination of the large size

and heterogeneous land management that characterizes the study area. Therefore, it was necessary to adopt a field-by-field analysis approach. In a following step, a supervised classification method was used to subdivide the study area into management zones with similar soil properties using the nine available ECa maps. To achieve this, the study area was first divided into four sub-areas based on geomorphological setting, patterns within the nine available ECa maps, and commonly available soil maps. These sub-areas were further divided into a total of 18 soil classes using a field-by-field analysis of the ECa maps. Finally, the classified maps of each field were merged in a composite raster and the result was a 1 m resolution map divided into 18 zones. Subsequently, 100 sampling locations were randomly selected to provide this map with soil profile descriptions and quantitative information on textural characteristics of each soil horizon. Here, it has to be noted that one soil augering location per hectare was used, and that this density is similar or lower compared to the sample density used to make commonly available soil maps for the same area. In a next step, a typical soil profile was assigned to each zone of the classified map by averaging the characteristics of each sampling point that was located within that zone. It was found that there was at least one statistically significant difference in terms of layering or texture between each typical soil profile for each of the 18 zones. Therefore, we concluded that the 18 zones identified by the classified EMI map represented 18 distinct soil units. Finally, the geometry of these soil units was compared to patterns in crop stress of sugar beet that were obtained from a satellite image for approximately one fourth of the study area. It was found that the areas with stressed crops matched well with particular soil units. It was therefore concluded that the geophysics-based soil map is particularly useful for characterizing management zones that are of great interest to precision agriculture applications.

In Chapter 4, the quantitative soil characterization obtained in Chapter 3 was used to simulate the growth of six crops cultivated in the study area in 2016 using the agro-ecosystem model AgroC. The necessary soil hydraulic parameters were obtained from the soil texture described in the geophysics-based soil map and from estimated dry bulk density. For this, the pedotransfer function of Rawls and Brakensiek (1985) was used. Simulated water content was found to be consistent with soil water content measured in two different locations and their comparison resulted in relatively low values of root mean square error (RMSE). The lowest RMSE values were obtained when the soil profile provided by the geophysics-based soil map well represented the actual soil profile. Additional simulations performed with soil hydraulic parameters that were obtained using the ROSETTTA pedotransfer function resulted in a much

higher RMSE between the measured and the simulated water content. This was attributed to the higher estimated values of the saturated hydraulic conductivity. In a next step, agro-ecosystem simulations were carried out for sugar beet, corn, potato, winter wheat, winter barley, and winter rapeseed for the 2016 growing season. In general, it was found that the magnitude of simulated water stress was a function of the crop type and of the soil characteristics with higher water stress occurring in summer crops and in coarser soils. At the same time, a reduction of LAI that was generally proportional to the simulated water stress was apparent in the simulations. To validate the agro-ecosystem simulations with independent data, six LAI_{NDVI} maps were produced from RapidEye satellite images. The simulated LAI was overall consistent with observed LAI_{NDVI} despite local inconsistencies between simulations and observations (e.g., during the blooming of winter rapeseed, in the case of irrigation, or when the effect of field-scale management was not adequately represented in the model). Overall, it could be shown that water stress had an impact on the simulated productivity at harvest for each of the investigated crops. The simulated productivity of one sugar beet field and one winter barley field matched well with the actual harvest of these fields in 2016, and the simulated productivity of corn and winter wheat corresponded well with literature values. Finally, maps of the simulated productivity at harvest were created for all four crops for the entire study area. The simulated productivity was 100% in soil units without water stress, whereas a reduction in productivity that was largely proportional to the intensity of water stress was apparent in soil units with underlying coarse layers. Clearly, such maps are highly relevant for practical agricultural applications, such as the selection of crop type, crop rotation, and seeding date depending on the previously recorded and forecasted precipitation intensity as well as on local soil characteristics.

In Chapter 5, the agro-ecosystem simulations based on inputs from the geophysics-based soil map described in Chapter 3 were compared to simulations based on two commonly available soil maps: i) a 1:5000 official soil map from the geological office of North Rhein-Westphalia and ii) a soil taxation map from the German Ministry of Finance. The two commonly available maps are provided with a qualitative description of the soil texture, which was converted to quantitative percentages of the grain size distribution using the USDA soil texture triangle. By comparing the soil descriptions of the three maps, the soil texture described for the upper fine sediments appeared to be rather similar. However, the textural information of the underlying coarse horizons differed significantly between the commonly available soil maps and the geophysics-based soil map. At the same time, the three soil maps

showed substantial differences in the location of the boundary between the four sub-areas in which the study area was previously divided. In a following step, the growth of corn, sugar beet, winter barley, winter rapeseed, and winter wheat was simulated with the agro-ecosystem model AgroC using the methodology described in Chapter 4 and inputs from the three soil maps. Here, the LAI simulated with AgroC was compared to the observed LAI_{NDVI} using the RMSE, the model efficiency (ME), and the explained variance (R^2). The use of inputs from the geophysics-based soil map consistently showed lower RMSE and higher ME and R^2. However, the improvement in simulation quality was rather subtle for winter crops and for periods with limited water stress. In contrast, the use of the geophysics-based soil map clearly outperformed the commonly available soil maps for summer crops (sugar beet and corn) and in periods with strong reduction in crop performance caused by water stress. Therefore, a more detailed comparison was performed for sugar beet. It was found that the magnitude of the reduction in performance of the commonly available soil maps compared to the geophysics-based soil map was caused by: i) a poor representation of the depth of the coarse sediments, ii) an inappropriate description of the soil texture of the upper fine horizons, and iii) a poor representation of the subdivision between sub-area BC and D. The lower performance of the simulations based on the commonly available soil maps also affected the simulated productivity at harvest. For example, the simulated productivity of sugar beet in a 2.3 ha field was overestimated when using inputs from the two commonly available soil maps, which was not the case for the simulations performed with inputs from the geophysics-based soil map.

Overall, it was concluded that an accurate representation of the spatial variability of soil characteristics that is provided by geophysics-based soil mapping provides long term benefits within an agricultural environment that is characterized by a reduced productivity caused by soil heterogeneity. The amount of soil augering locations that are necessary to obtain such a geophysics-based soil map is similar or lower than what is generally required for commonly available soil maps, but the resulting resolution is much higher. The geophysics-based soil map allows identifying meaningful management zones within individual fields, and thus clearly provides added value in agricultural applications. Due to the quantitative information on layering and texture, this map also allowed meaningful agro-ecosystem simulations of multiple crops in which soil water content dynamics, crop growth, and crop productivity at harvest were correctly captured at the field scale and beyond. It was also shown that simulations based on this geophysics-based soil characterization clearly outperformed

simulations based on the commonly available soil maps for the study area investigated here, especially in dry periods. Since the combination of geophysics-based soil mapping and agro-ecosystem modelling provided reliable information on the spatial distribution of water stress and crop productivity at harvest, this approach may allow to reduce yield gaps by supporting site-specific selection of the most productive and sustainable agricultural management options. One could argue that similar results could be achieved by parametrizing agro-ecosystem models using time series of available satellite images. However, the advantage of the methodology proposed here lies in the potential of simulating future scenarios (e.g. climate change scenarios), which is vital to meet present and future food security and environmental challenges.

6.2. Outlook

The geophysical data analysis and agro-ecosystem modelling strategies developed in this thesis are able to provide valuable information for agricultural management. For example, maps of simulated productivity at harvest similar to those presented in Chapter 4 can help farmers in the maximization of crop productivity. Furthermore, the seeding of summer crops could be timed based on the precipitation forecast for the coming days or weeks. Finally, the best crop rotation for a particular field could be determined using the developed strategies. In this case, the agro-ecosystem simulations should not be based on a single growing season. Instead, the simulation period should be extended to longer periods (e.g., 30 years) in order to allow the evaluation of the cost-benefit ratio of long-term strategies.

Despite the promising results, the methodology described in this thesis is not exempt from limitations and can certainly be improved. For example, the results of the supervised classification methodology depend to some extent on the interpreter as discussed in Chapter 3. Even if this approach was found to be the most suited to obtain soil information from EMI measurements in this study, future research should explore the use of more complex classification methods such as supervised machine learning classification. The use of unsupervised classification methodologies, such as the iterative self-organizing (ISO) clustering technique or even the application of more complex artificial neural networks should also be explored as the influence of the operator is strongly reduced in these methods. However, the suitability of such methodologies may be limited by the influence of contrasting environmental conditions that are affecting EMI measurements collected at different times. Nevertheless, the application of more complex data filtering, management, and conversion

techniques could lead to significant improvements. For example, the Z-score normalization method described in Rudolph et al. (2015) can partially remove the influence of contrasting environmental conditions from EMI measurements, which may allow the use of an unsupervised classification methodology. This is illustrated in Figure 41 for 18 fields located in the upper terrace of the study area. The unsupervised classification of Z-transformed ECa maps resulted in a consistent map in which all fields show patterns that are likely to represent subsurface structures (Figure 41b). In contrast, an unsupervised classification of the non-transformed data did not result in meaningful results (Figure 41a) and only five fields showed patterns that represent the known variation in subsurface properties (see patterns in crop performance in Figure 17a and classified map in Figure 13a-b). Despite these encouraging preliminary results, the use of Z-transformed ECa for the classification of EMI data also showed some limitations that require further investigation. For example, some fields are subdivided in areas with different and unrecorded management that might have unclear effects on the classification results. This example demonstrates that it is worthwhile to test and analyze the use of different strategies for the classification of an extensive EMI dataset and obtain more standardized products.

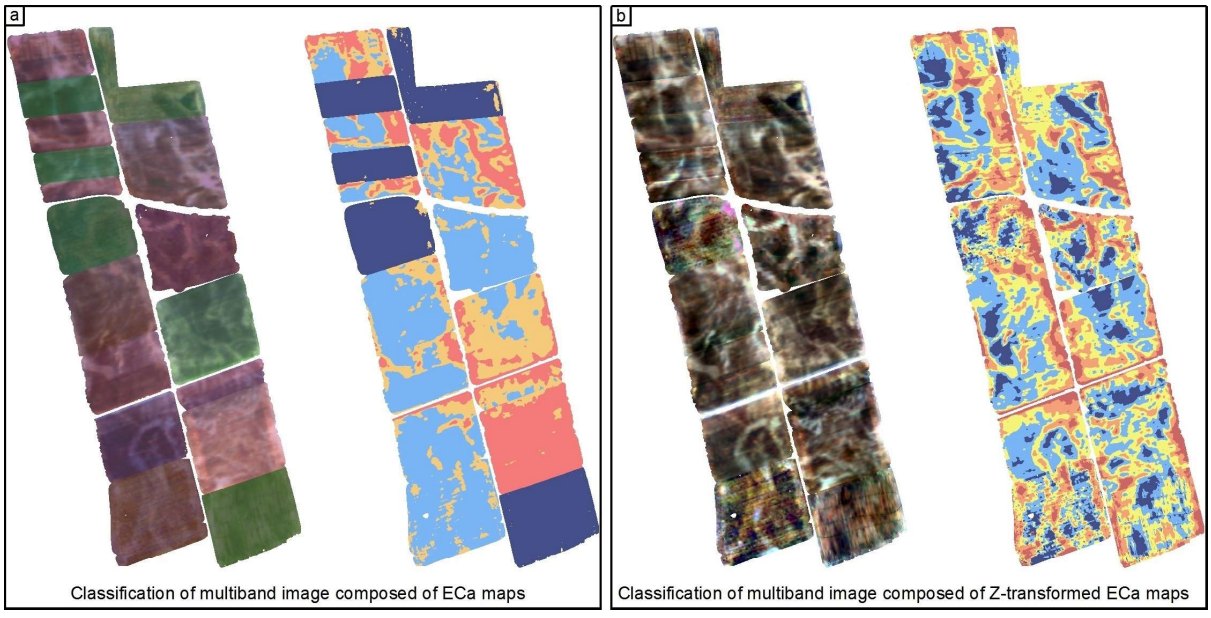

Figure 41: a) Multiband image of ECa maps of 18 fields within the upper terrace and resulting classified map obtained with unsupervised classification method and b) multiband image of the Z-transformed ECa maps of the same fields and resulting unsupervised classification map. Both multiband images are composed of red band = HCP 35 cm, green band = HCP 50 cm, and blue band = HCP 71 cm).

This thesis demonstrated the added value provided by geophysics-based soil mapping beyond the farm-scale. Although it seems attractive to extend this approach to other areas or the regional scale, the costs of the collection of EMI and ground truth data should be taken into account in such considerations. In fact, the production of the geophysics-based soil map was a time- and resource-consuming activity that can be divided in three distinct phases: i) the collection of EMI measurements (220 hours of work with two operators), ii) the description of soil profiles and the collection of soil samples (50 hours of work with three operators), and iii) the laboratory analysis of soil samples (400 hours of work with one laboratory technician). Using the results of the comparison of the agro-ecosystem simulations obtained with the inputs from the three soil maps, it is possible to speculate about scenarios with a reduced amount of invested resources. The EMI measurements were performed with a dense spacing of 2.5 m between measurement lines. In retrospect, this spacing could have been increased to 10 m in some fields without strong soil heterogeneity. By increasing the spacing between measured lines, a considerable reduction of ~60% in the measurement time can be obtained. For the study area investigated here, this applied to 7.5 ha. Therefore, a reduction of 4.7% of the measurement time could have been achieved. During the selection of soil sampling locations, 21 points were placed in anthropogenic deposits or in other rather small soil units. In the end, these deposits did not show meaningful differences in the agro-ecosystem simulations compared to the surrounding non-anthropogenic deposits, despite clear differences in soil layering and texture. The time needed to perform soil sampling could have been reduced by ~20% by removing these locations. Finally, a total of 552 soil samples were analyzed to obtain information on grain size distribution. By analyzing the results of the ago-ecosystem simulations performed with the three soil maps, it is apparent that similar results could have been achieved with a qualitative characterization of soils. Therefore, the textural characterization could have been obtained from the commonly available soil maps or estimated with hand texturing. This could have substantially reduced the laboratory analysis to the subsoil properties. In this scenario, the number of soil samples would have been reduced to 229, which is a time reduction of 59%. In summary, this retrospective analysis suggests that the total time needed to characterize the 1 x 1 km study area could have been reduced by 29%. Obviously, the appropriate resolution of EMI measurements and the required amount of soil samples is not known a priori. However, the results of this retrospective analysis may guide the characterization of neighboring areas since the geology that characterizes the investigated study area extends well beyond the 1 km^2 area investigated here.

In order to move forward, a hierarchical analysis approach could be used to obtain detailed soil information in agricultural areas at the regional, national, or transnational scale. In a first step, large areas of tens of km^2 within typical geological settings could be identified based on available soil and geological maps. Within each of these areas, a relatively small area could be investigated with the procedures described in this thesis. Then, the insights obtained within this small area could be used to assemble a complete soil map for the agricultural areas within each geological setting. Clearly, this would require a considerable amount of time and resources, but this is common to all soil mapping performed at a regional or national level. In order to achieve such a large-scale digital soil characterization, improvements in geophysical instruments and data acquisition strategies are required. For example, it would be highly desirable when EMI devices would provide accurate measurements when operated on a tractor because this would allow the collection of ECa measurements during field management. Commercial EMI equipment to achieve such measurements is becoming available, and novel EMI system designs (e.g., Mester et al. 2014) may allow to improve the accuracy of EMI measurements in the presence of measurement errors associated with the proximity of the tractor that affects the inductive measurements.

Obviously, EMI is only one of the available mobile methods that provide proximal information on soil properties. As previously discussed, a number of studies used a combination of multiple proximal and remote sensing platforms for soil mapping with encouraging results. Even if EMI proved effective in studying a rather exhaustive soil depth of an extensive area and provided vital information that enabled exploiting crop modelling capabilities, the application of the same technique to a rather different area might not be as effective as in this study. Different sensors are more effective under certain site-specific conditions and the simultaneous use of multiple sensors can overcome the limitation of a single device. However, each additional measurement increases the mapping costs (Taylor et al., 2010). Therefore, it is vital to use the most effective instrument at each site. To reduce measurement costs, the assessment of the most suited proximal or remote sensing technique could be performed on a small portion of the area that is the objective of the mapping. In a second step, the best performing device could be used to map the entire area with the support of existing datasets (e.g., general-purpose soil maps, yield maps, and satellite data) or in combination with air-borne devices such as air-borne EM or air-borne gamma-ray spectrometry.

Finally, in order to develop more efficient data acquisition strategies, farmers should be more actively involved in the collection of geophysical data and soil samples. For example, farmers are already collecting a variety of soil samples for bio-geochemical analysis on a regular basis for regulatory control and planning of nutrient management. An important step forward would be to include soil description and/or photos of soil profiles provided by farmers via a simple and standardized procedure that makes use of the latest portable technology (e.g., mobile apps). This may allow the development of an extensive database that can be used to develop and validate high-resolution digital soil maps. By doing this, farmers would benefit from a product that is publicly available and would not be forced to produce their own soil characterization. Moreover, continuous feedback between farmers and soil scientists on the practical use of these soil maps would make these products more effective. This process could be streamlined by regulatory bodies through the definition of guidelines for fruitful cooperation between farmers and soil scientists (Bouma, 2001) and appropriate incentives, thus paving the way for a more productive and sustainable agriculture.

A further promising extension of the research presented in this thesis is to combine the simulation set-up with weather forecast. By assimilating information on forecasted precipitation quantity and timing, it would be possible to optimize irrigation scheduling aimed at the maximization of crop productivity in drought conditions. The potential of this approach is illustrated in the following example, where the amount and timing of irrigation were implemented into the atmospheric input data of the AgroC model by increasing the amount of precipitation at certain time steps. A rule-based approach for irrigation scheduling was adopted and it was assumed that a 7-day perfect weather forecast was available. Rule-based irrigation scheduling is a well-established method in which a set of rules is used to determine irrigation timing and amount (Bergez et al., 2002; Jamal et al., 2018).

In the example presented here, the need for irrigation was evaluated at the first day of each week after the emergence of sugar beet on the 2nd of May. The amount of irrigation was determined based on the simulated water stress reduction factor (h in Equation 10 in Chapter 4) at the end of the coming week using the actual precipitation in 2016 (i.e., a perfect weather forecast). If the reduction factor was between 0.85 and 1.0, no irrigation was applied. If the stress reduction factor was lower than 0.85, 3 mm of irrigation was applied and the simulation for the coming week was repeated. If the reduction factor after seven days was still lower than

0.85, the process was repeated by adding an additional 3 mm of irrigation. This procedure was repeated until h > 0.85 was obtained or until a maximum of 30 mm of irrigation was applied. This weekly irrigation scheduling was repeated until the end of the growing season.

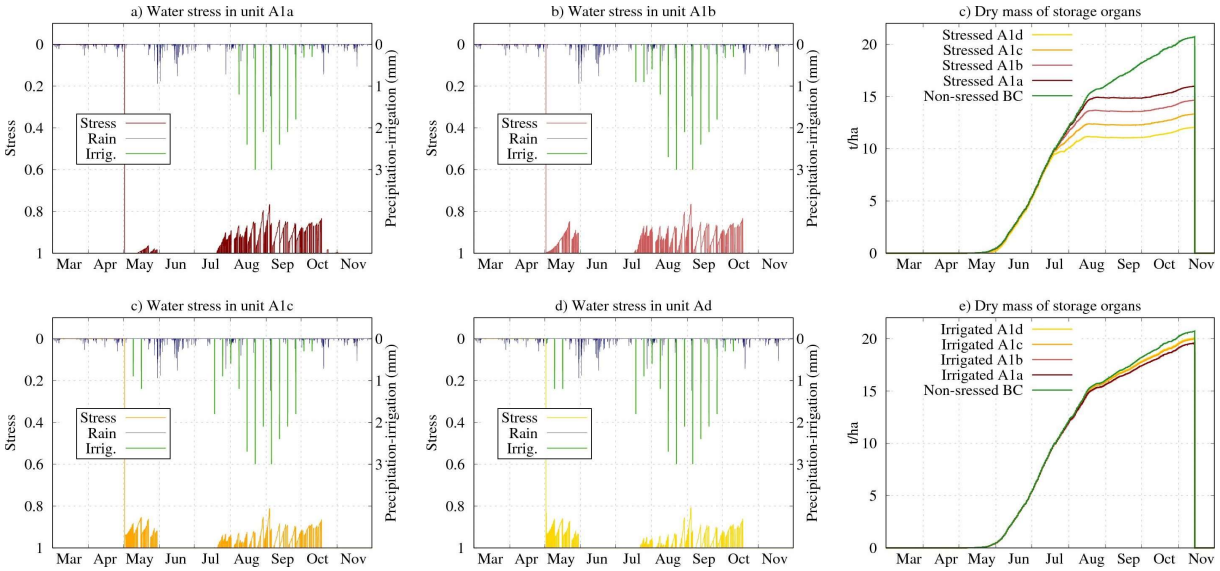

Figure 42: Effect of irrigation on the simulation of sugar beet growing on field F01. The amount of precipitation, irrigation, and the water stress simulated in each soil unit is shown in a) for soil unit A1a, b) for A1b, d) for A1c, and e) for A1d. The productivity at harvest of sugar beet is shown for the case c) without irrigation and f) with rule-based irrigation.

Table 16: Number of irrigation events, average irrigated amount (mm), total amount of irrigation (m^3 ha^{-1}), and productivity at harvest (t ha^{-1}) with non-irrigated and irrigated sugar beet for the four soil units of field F01.

Soil unit	Irrigation events	Avg. Irrig. (mm)	Total (m^3 ha^{-1})	Non-irrigated prod. (t ha^{-1})	Irrigated prod. (t ha^{-1})
A1a	10	18.6	1860	16.0	19.6
A1b	13	16.6	2160	14.5	19.7
A1c	15	16.4	2460	13.3	19.7
A1d	16	16.3	2610	12.1	19.8

The simulation results obtained with this irrigation scheduling are shown in Figure 42 and summarized in Table 16. The simulated productivity at harvest of dry beets in field F01 without irrigation was 14.3 t ha^{-1} and increased to 19.7 t ha^{-1} using irrigation (+ 23.3 t ha^{-1} of wet beets). The amount of irrigation that was needed to achieve this increase in productivity was 2231 m^3 ha^{-1}. The simulation strategy outlined above could allow farmers to optimize irrigation and maximize productivity, or to perform a cost-benefit analysis for the use of irrigation. Even if it is an essential practice in other regions of the world (Topak et al., 2011),

irrigation of sugar beet is considered to be a non-profitable practice in North Rhein-Westphalia based on current climate conditions (Landwirtschaftskammer, 2019). In the proposed irrigation scenario, a rough estimation resulted in additional cost for the farmer of ~330 Euro ha^{-1} (~100 Euro ha^{-1} for the installation/usage of the machinery and 1 Euro ha^{-1} per mm of irrigated water). Here, it was assumed that the equipment for irrigation is already available (Hanse et al., 2010; Lozán et al., 2007). Assuming a price of ~30 Euro t^{-1} of wet beets, the increase in productivity of 23.3 t ha^{-1} would result in an increased income of ~690 Euro ha^{-1} for the farmer, which is higher than the costs. Even if this rough calculation suggests that irrigation might be profitable, it is important to realize that the necessary perfect weather forecast is currently not available. Obviously, the irrigation cost might strongly increase in case of underestimated precipitation (overuse of irrigation) and the income may decrease in case of overestimated precipitation (lower productivity). Furthermore, costs for irrigation water and fuel vary in different regions, and the final sugar content of the wet beets also influences the income for the farmer. Finally, the European sugar sector no longer has a guaranteed price/quota system for sugar beet. Therefore, sugar price is are currently fluctuating depending on the supply and demand of beets, thus increasing the uncertainty of such cost/benefit analyses.

In the light of recent global climatic change and the expected more frequent occurrence of dry summers and heat waves, the long-term vision of central-European farmers and regulatory bodies is rapidly changing and irrigation is now not only necessary to improve yield but also to prevent harvest failure. Within this light, a reliable quantification of both the economic costs and benefits of irrigating crops is vital, and the work presented in this thesis can help to provide a foundation for improved methods to simulate present and future climate scenarios. An important step for an operational irrigation scheduling system based on the approach outlined here would be the consideration of uncertainty in forecasted meteorological data. Currently, weekly precipitation forecasts are often not very reliable, which affects the performance of this type of irrigation scheduling (Linker et al., 2018). However, short-term forecasting tools are constantly improving and their availability on the internet is rapidly expanding (Linker and Sylaios, 2016).

A promising long-term further development would be the consideration of nutrient availability and stress in the developed model framework. This would require extending AgroC with a module that simulates nutrient uptake and distribution within the soil-crop

continuum. In a first step, nitrogen should be added to the AgroC model, but other nutrients such as phosphorus are also of interest because crop growth is limited by phosphorous in many regions of the world (Goll et al., 2017; Jiang et al., 2019; Lun et al., 2018). With this addition, the AgroC model could be used as a digital agricultural avatar (DAA) and be exploited to predict and forecast crop development in response to agricultural management and within-field interventions.

Another promising avenue for further analysis is to use the methodology proposed in this thesis for the simulation of carbon turnover on the landscape scale. This is relatively straightforward since AgroC is already designed to calculate CO_2 assimilation by crops and soil respiration. Crops experiencing water stress generally show a reduced magnitude of net ecosystem exchange (NEE). By applying irrigation, the magnitude of NEE can be increased and this could lead to increased carbon sequestration that can be quantified with agro-ecosystem models. A comparison between irrigated and non-irrigated scenarios could provide an estimation of the environmental costs and benefits of irrigation that should be examined alongside the economic analysis. Moreover, CO_2 emissions are known to be reduced by an efficient management of irrigation (West et al., 2004) and the application of irrigation could save a considerable portion of land from farming. For example, 1 hectare of irrigated sugar beet produced as much as 1.4 hectares of non-irrigated sugar beet in the irrigation analysis for field F01 presented above. Maximizing local productivity is not only required for feeding the growing world population but also by environmental concerns since it is known that land use changes, such as the conversion from forest to cropland, can reduce global carbon sequestration (Quesada et al., 2018). Within this context, it is vital to use the most updated methods and technology not only to achieve higher yield, but also to look at agriculture in a more holistic way as it is done, for example, in the field of agro-ecology. By doing so, it would be possible to meet the goals of sustainable agriculture and to combine a high economic income with low environmental impact and reduced use of non-renewable resources.

References

Adamchuk, V. I., Hummel, J. W., Morgan, M. T., Upadhyaya, S. K., (2004): On-the-go soil sensors for precision agriculture. *Computers and electronics in agriculture* 44(1), 71-91, doi:10.1016/j.compag.2004.03.002.

Ali, M., Montzka, C., Stadler, A., Menz, G., Thonfeld, F., Vereecken, H., (2015): Estimation and validation of RapidEye-based time-series of leaf area index for winter wheat in the Rur catchment (Germany). *Remote sensing* 7(3), 2808-2831, doi:10.3390/rs70302808.

Allen, R. G., Pereira, L. S., Raes, D., Smith, M., (1998): FAO Irrigation and drainage paper 56 - Crop evapotranspiration, Guidelines for computing crop water requirements. *FAO, Rome* 300(9), D05109.

Allred, B., Daniels, J. J., Ehsani, M. R., (2008). Handbook of agricultural geophysics. CRC Press.

André, F., van Leeuwen, C., Saussez, S., Van Durmen, R., Bogaert, P., Moghadas, D., de Rességuier, L., Delvaux, B., Vereecken, H., Lambot, S., (2012): High-resolution imaging of a vineyard in south of France using ground-penetrating radar, electromagnetic induction and electrical resistivity tomography. *Journal of Applied Geophysics* 78, 113-122, doi:10.1016/j.jappgeo.2011.08.002.

Anjum, S. A., Xie, X., Wang, L. C., Saleem, M. F., Man, C., Lei, W., (2011): Morphological, physiological and biochemical responses of plants to drought stress. *African Journal of Agricultural Research* 6(9), 2026-2032.

Antle, J. M., Basso, B., Conant, R. T., Godfray, H. C. J., Jones, J. W., Herrero, M., Howitt, R. E., Keating, B. A., Munoz-Carpena, R., Rosenzweig, C., (2017): Towards a new generation of agricultural system data, models and knowledge products: Design and improvement. *Agricultural systems* 155, 255-268, doi:10.1016/j.agsy.2016.10.002.

Baker, F. G., (1978): Variability of hydraulic conductivity within and between nine Wisconsin soil series. *Water Resources Research* 14(1), 103-108.

Ball, G., Hall, D. J., (1965). A novel method of data analysis and pattern classification. Tch. Report 5RI, Project 5533. Stanford RI, Menlo Park, Ca. USA.

Baret, F., Houles, V., Guérif, M., (2007): Quantification of plant stress using remote sensing observations and crop models: the case of nitrogen management. *Journal of Experimental Botany* 58(4), 869-880, doi:10.1093/jxb/erl231.

Basso, B., Ritchie, J. T., Pierce, F. J., Braga, R. P., Jones, J. W., (2001): Spatial validation of crop models for precision agriculture. *Agricultural Systems* 68(2), 97-112, doi:10.1016/S0308-521X(00)00063-9.

Batchelor, W. D., Basso, B., Paz, J. O., (2002): Examples of strategies to analyze spatial and temporal yield variability using crop models. *European Journal of Agronomy* 18(1-2), 141-158, doi:10.1016/S1161-0301(02)00101-6.

Batchelor, W. D., Paz, J. O., (1998). Process-oriented crop growth models as a tool to evaluate spatial yield variability, Proceedings of the First International Conference on Geospatial Information in Agriculture and Forestry, pp. 198-205.

Beck, P. S. A., Atzberger, C., Høgda, K. A., Johansen, B., Skidmore, A. K., (2006): Improved monitoring of vegetation dynamics at very high latitudes: A new method using MODIS NDVI. *Remote sensing of Environment* 100(3), 321-334, doi::10.1016/j.rse.2005.10.021.

Bergez, J. E., Deumier, J. M., Lacroix, B., Leroy, P., Wallach, D., (2002): Improving irrigation schedules by using a biophysical and a decisional model. *European journal of Agronomy* 16(2), 123-135.

Binley, A., Hubbard, S. S., Huisman, J. A., Revil, A., Robinson, D. A., Singha, K., Slater, L. D., (2015): The emergence of hydrogeophysics for improved understanding of subsurface processes over multiple scales. *Water Resources Research* 51(6), 3837-3866, doi:10.1002/2015WR017016.

Boenecke, E., Lueck, E., Ruehlmann, J., Gruendling, R., Franko, U., (2018): Determining the within-field yield variability from seasonally changing soil conditions. *Precision Agriculture* 19(4), 750-769, doi:10.1016/S0022-1694(01)00464-4.

Bogena, H., Huisman, J., Schilling, B., Weuthen, A., Vereecken, H., (2017): Effective calibration of low-cost soil water content sensors. *Sensors* 17(1), 208, doi:10.2136/vzj2018.03.0055.

Bogena, H. R., Montzka, C., Huisman, J. A., Graf, A., Schmidt, M., Stockinger, M., von Hebel, C., Hendricks-Franssen, H. J., van der Kruk, J., Tappe, W., (2018): The TERENO-Rur Hydrological Observatory: A Multiscale Multi-Compartment Research Platform for the Advancement of Hydrological Science. *Vadose Zone Journal* 17(1).

Bolinder, M. A., Angers, D. A., Dubuc, J. P., (1997): Estimating shoot to root ratios and annual carbon inputs in soils for cereal crops. *Agriculture, ecosystems & environment* 63(1), 61-66.

Boons-Prins, E. R., De Koning, G. H. J., Van Diepen, C. A., (1993). Crop-specific simulation parameters for yield forecasting across the European Community, CABO-DLO [etc.].

Boote, K. J., Jones, J. W., Pickering, N. B., (1996): Potential uses and limitations of crop models. *Agronomy journal* 88(5), 704-716.

Borg, H., Grimes, D. W., (1986): Depth development of roots with time: An empirical description. *Transactions of the ASAE* 29(1), 194-0197.

Bouma, J., (1989). Using soil survey data for quantitative land evaluation, Advances in soil science. Springer, pp. 177-213.

Bouma, J., (2001): The new role of soil science in a network society. *Soil Science* 166(12), 874-879.

Bouman, B. A. M., (2001). ORYZA2000: modeling lowland rice. IRRI.

Brakensiek, D. L., Rawls, W. J., (1994): Soil containing rock fragments: effects on infiltration. *Catena* 23(1-2), 99-110.

Brauman, K. A., Siebert, S., Foley, J. A., (2013): Improvements in crop water productivity increase water sustainability and food security—a global analysis. *Environmental Research Letters* 8(2), 024030, doi:10.1088/1748-9326/8/2/024030.

Brogi, C., Huisman, J. A., Pätzold, S., von Hebel, C., Weihermüller, L., Kaufmann, M. S., van der Kruk, J., Vereecken, H., (2019): Large-scale soil mapping using multi-configuration EMI and supervised image classification. *Geoderma* 335, 133-148, doi:10.1016/j.geoderma.2018.08.001.

Campbell, R. B., Bower, C. A., Richards, L. A., (1949): Change of electrical conductivity with temperature and the relation of osmotic pressure to electrical conductivity and ion concentration for soil extracts. *Soil Science Society of America Journal* 13(C), 66-69.

Cassman, K. G., Dobermann, A., Walters, D. T., Yang, H., (2003): Meeting cereal demand while protecting natural resources and improving environmental quality. *Annual Review of Environment and Resources* 28(1), 315-358, doi:10.1146/annurev.energy.28.040202.122858.

Castrignano, A., Wong, M. T. F., Stelluti, M., De Benedetto, D., Sollitto, D., (2012): Use of EMI, gamma-ray emission and GPS height as multi-sensor data for soil characterisation. *Geoderma* 175, 78-89, doi:10.1016/j.geoderma.2012.01.013.

Ceglar, A., Toreti, A., Lecerf, R., Van der Velde, M., Dentener, F., (2016): Impact of meteorological drivers on regional inter-annual crop yield variability in France. *Agricultural and forest meteorology* 216, 58-67, doi:10.1016/j.agrformet.2015.10.004.

Chartzoulakis, K., Bertaki, M., (2015): Sustainable water management in agriculture under climate change. *Agriculture and Agricultural Science Procedia* 4, 88-98, doi:10.1016/j.aaspro.2015.03.011.

Chipanshi, A. C., Ripley, E. A., Lawford, R. G., (1999): Large-scale simulation of wheat yields in a semi-arid environment using a crop-growth model. *Agricultural Systems* 59(1), 57-66, doi:10.1016/S0308-521X(98)00082-1.

Ciampalini, A., André, F., Garfagnoli, F., Grandjean, G., Lambot, S., Chiarantini, L., Moretti, S., (2015): Improved estimation of soil clay content by the fusion of remote hyperspectral and proximal geophysical sensing. *Journal of Applied Geophysics* 116, 135-145, doi:10.1016/j.jappgeo.2015.03.009.

Coleman, K., Jenkinson, D. S., (1996). RothC-26.3-A Model for the turnover of carbon in soil, Evaluation of soil organic matter models. Springer, pp. 237-246.

Corwin, D. L., Lesch, S. M., (2003): Application of soil electrical conductivity to precision agriculture. *Agronomy Journal* 95(3), 455-471.

Corwin, D. L., Lesch, S. M., (2005): Apparent soil electrical conductivity measurements in agriculture. *Computers and electronics in agriculture* 46(1), 11-43, doi:10.1016/j.compag.2004.10.005.

Daddow, R. L., Warrington, G., (1983). Growth-limiting soil bulk densities as influenced by soil texture. Watershed Systems Development Group, USDA Forest Service Fort Collins, CO.

De Benedetto, D., Castrignanò, A., Rinaldi, M., Ruggieri, S., Santoro, F., Figorito, B., Gualano, S., Diacono, M., Tamborrino, R., (2013): An approach for delineating homogeneous zones by using multi-sensor data. *Geoderma* 199, 117-127, doi:10.1016/j.geoderma.2012.08.028.

De Costa, W. A. J. M., Dennett, M. D., (1992): Is canopy light extinction coefficient a species-specific constant?

De Smedt, P., Van Meirvenne, M., Meerschman, E., Saey, T., Bats, M., Court-Picon, M., De Reu, J., Zwertvaegher, A., Antrop, M., Bourgeois, J., (2011): Reconstructing palaeochannel morphology with a mobile multicoil electromagnetic induction sensor. *Geomorphology* 130(3-4), 136-141, doi:10.1016/j.geomorph.2011.03.009.

Della Chiesa, S., la Cecilia, D., Genova, G., Balotti, A., Thalheimer, M., Tappeiner, U., Niedrist, G., (2019): Farmers as data sources: Cooperative framework for mapping soil properties for permanent crops in South Tyrol (Northern Italy). *Geoderma* 342, 93-105, doi:10.1016/j.geoderma.2019.02.010.

Ding, J., Yu, D., (2014): Monitoring and evaluating spatial variability of soil salinity in dry and wet seasons in the Werigan–Kuqa Oasis, China, using remote sensing and electromagnetic induction instruments. *Geoderma* 235, 316-322, doi:10.1016/j.geoderma.2014.07.028.

Doolittle, J. A., Brevik, E. C., (2014): The use of electromagnetic induction techniques in soils studies. *Geoderma* 223, 33-45, doi:10.1016/j.geoderma.2014.01.027.

Ehlers, W., Köpke, U., Hesse, F., Böhm, W., (1983): Penetration resistance and root growth of oats in tilled and untilled loess soil. *Soil and Tillage Research* 3(3), 261-275.

ESRI, (2014). ArcGIS Desktop Help.

ESRI, (2015). Esri, DIgitalGlobe, GeoEye, Earthstar Geographics, CNES/Airbus DS, USDA, AEX, Getmapping, Aerogrid, IGN, IGP, swisstopo, and the GIS User Comunity.

ESRI, (2017). ArcGIS Desktop: Release 10.3 Redlands, CA.

European Committee for Standardization, M. C. A. M., B-10000 Brussels, CWA 16373:2011, (2011). Best practice approach for electromagnetic induction (EMI) measurements of the near surface.

Evans, L. T., (1996). Crop evolution, adaptation and yield. Cambridge university press.

Evans, L. T., Fischer, R. A., (1999): Yield potential: its definition, measurement, and significance. *Crop science* 39(6), 1544-1551.

FAO, (1999). Agribusiness Handbooks, vol. 4, sugar beet and white sugar. Food and Agricultural Organization of the United Nations/European Bank for ….

Feddes, J, K. P., H, Z., (1978): Simulation of field water use and crop yield. *Simulation Monographs*.

Flint, A. L., Childs, S., (1984): Physical Properties of Rock Fragments and Their Effect on Available Water in Skeletal Soils 1. *Erosion and productivity of soils containing rock fragments* (erosionandprodu), 91-103.

Foley, J. A., Ramankutty, N., Brauman, K. A., Cassidy, E. S., Gerber, J. S., Johnston, M., Mueller, N. D., O'Connell, C., Ray, D. K., West, P. C., (2011): Solutions for a cultivated planet. *Nature* 478(7369), 337, doi:10.1038/nature10452.

Franzen, D. W., Hopkins, D. H., Sweeney, M. D., Ulmer, M. K., Halvorson, A. D., (2002): Evaluation of soil survey scale for zone development of site-specific nitrogen management. *Agronomy Journal* 94(2), 381-389.

Frederiksen, R. R., Christiansen, A. V., Christensen, S., Rasmussen, K. R., (2017): A direct comparison of EMI data and borehole data on a 1000ha data set. *Geoderma* 303, 188-195, doi:10.1016/j.geoderma.2017.04.028.

Galambošová, J., Rataj, V., Prokeinová, R., Presinska, J., (2014): Determining the management zones with hierarchic and non-hierarchic clustering methods. *Research in Agricultural Engineering* 60(Special Issue), doi:10.17221/34/2013-RAE.

Gebbers, R., Adamchuk, V. I., (2010): Precision agriculture and food security. *Science* 327(5967), 828-831, doi:10.1126/science.1182768.

Gebbers, R., Lück, E., (2005). Comparison of geoelectrical methods for soil mapping, Proceedings of the 5th European Conference on Precision Agriculture'.(Ed. JV Stafford) pp, pp. 473-479.

GF_Instruments, (2011). CMD electromagnetic conductivity meter user manual V. 1.5 GF Instruments s.r.o. Geophysical Equipment and Services.

Goll, D., Vuichard, N., Maignan, F., Jornet-Puig, A., Sardans, J., Violette, A., Peng, S., Sun, Y., Kvakic, M., Guimberteau, M., (2017): A representation of the phosphorus cycle for

ORCHIDEE (revision 4520). *Geoscientific Model Development Discussions* 10(10), 3745-3770, doi:10.5194/gmd-10-3745-2017.

Grisso, R. D., Alley, M. M., Holshouser, D. L., Thomason, W. E., (2005): Precision Farming Tools. Soil Electrical Conductivity.

Han, H., Yan, Y. R. Z., (2017): Response of winter wheat grain yield and water use efficiency to deficit irrigation in the North China Plain. *Emirates Journal of Food and Agriculture*, 971-977, doi:10.9755/ejfa.2017.v29.i12.1567.

Hanse, B., Tijink, F. G. J., Mußhoff, O., Märländer, B., (2010): Comparison of costs and yields of'type top'and'type average'growers in Dutch sugar beet growing. *Sugar Industry* 135, 550-560.

Hasan, S., Montzka, C., Rüdiger, C., Ali, M., Bogena, H. R., Vereecken, H., (2014): Soil moisture retrieval from airborne L-band passive microwave using high resolution multispectral data. *ISPRS Journal of Photogrammetry and Remote Sensing* 91, 59-71, doi:10.1016/j.isprsjprs.2014.02.005.

Heuvelink, G. B. M., Webster, R., (2001): Modelling soil variation: past, present, and future. *Geoderma* 100(3-4), 269-301.

Hoffmann, C. M., Kenter, C., (2018): Yield Potential of Sugar Beet–Have We Hit the Ceiling? *Frontiers in plant science* 9, 289, doi:10.3389/fpls.2018.00289.

Hoogenboom, G., Jones, J. W., Wilkens, P. W., Batchelor, W. D., Bowen, W. T., Hunt, L. A., Pickering, N. B., Singh, U., Godwin, D. C., Baer, B., (1994): Crop models. *DSSAT version* 3(2), 95-244.

Huang, J., Koganti, T., Santos, F. A. M., Triantafilis, J., (2017a): Mapping soil salinity and a fresh-water intrusion in three-dimensions using a quasi-3d joint-inversion of DUALEM-421S and EM34 data. *Science of The Total Environment* 577, 395-404, doi:10.1016/j.scitotenv.2016.10.224.

Huang, J., Lark, R. M., Robinson, D. A., Lebron, I., Keith, A. M., Rawlins, B., Tye, A., Kuras, O., Raines, M., Triantafilis, J., (2014): Scope to predict soil properties at within-field scale from small samples using proximally sensed γ-ray spectrometer and EM induction data. *Geoderma* 232, 69-80, doi:10.1016/j.geoderma.2014.04.031.

Huang, J., McBratney, A. B., Minasny, B., Triantafilis, J., (2017b): Monitoring and modelling soil water dynamics using electromagnetic conductivity imaging and the ensemble Kalman filter. *Geoderma* 285, 76-93, doi:10.1016/j.geoderma.2016.09.027.

ImageJ, i. p. a. a. i. j., NIH, (2016).

Jadoon, K. Z., Moghadas, D., Jadoon, A., Missimer, T. M., Al-Mashharawi, S. K., McCabe, M. F., (2015): Estimation of soil salinity in a drip irrigation system by using joint inversion of multicoil electromagnetic induction measurements. *Water Resources Research* 51(5), 3490-3504, doi:10.1002/2014WR016245.

Jamal, A., Linker, R., Housh, M., (2018): Comparison of various stochastic approaches for irrigation scheduling using seasonal climate forecasts. *Journal of Water Resources Planning and Management* 144(7), 04018028, doi:10.1061/(ASCE)WR.1943-5452.0000951.

Jiang, M., Caldararu, S., Zaehle, S., Ellsworth, D. S., Medlyn, B. E., (2019): Towards a more physiological representation of vegetation phosphorus processes in land surface models. *New Phytologist*, doi:10.1111/nph.15688.

Jing, Y. Z., Huang, J., Banks, R., Triantafilis, J., (2017): Scope to map soil management units at the district level from remotely sensed γ-ray spectrometry and proximal sensed EM induction data. *Soil Use and Management* 33(4), 538-552, doi:10.1111/sum.12359.

Jones, C. A., Kiniry, J. R., (1986). CERES-Maize; a simulation model of maize growth and development.

Jones, J. W., Hoogenboom, G., Porter, C. H., Boote, K. J., Batchelor, W. D., Hunt, L. A., Wilkens, P. W., Singh, U., Gijsman, A. J., Ritchie, J. T., (2003): The DSSAT cropping system model. *European journal of agronomy* 18(3-4), 235-265.

Káš, M., Mühlbachova, G., Kusá, H., (2018): Winter wheat yields under different soil-climatic conditions in a long-term field trial. *Plant, Soil and Environment*, doi:10.17221/606/2018-PSE.

Keller, G. V., Frischknecht, F. C., (1966): Electrical methods in geophysical prospecting.

Kelley, J., Higgins, C. W., Pahlow, M., Noller, J., (2017): Mapping Soil Texture by Electromagnetic Induction: A Case for Regional Data Coordination. *Soil Science Society of America Journal* 81(4), 923-931, doi:10.2136/sssaj2016.12.0432.

King, J. A., Dampney, P. M. R., Lark, R. M., Wheeler, H. C., Bradley, R. I., Mayr, T. R., (2005): Mapping potential crop management zones within fields: use of yield-map series and patterns of soil physical properties identified by electromagnetic induction sensing. *Precision Agriculture* 6(2), 167-181.

Klosterhalfen, A., Herbst, M., Weihermüller, L., Graf, A., Schmidt, M., Stadler, A., Schneider, K., Subke, J. A., Huisman, J. A., Vereecken, H., (2017): Multi-site calibration and validation of a net ecosystem carbon exchange model for croplands. *Ecological Modelling* 363, 137-156, doi:10.1016/j.ecolmodel.2017.07.028.

Klostermann, J., (1992). Das Quartär der Niederrheinischen Bucht: Ablagerungen der letzten Eiszeit am Niederrhein. Geologisches Landesamt Nordrhein-Westfalen.

Krüger, J., Franko, U., Fank, J., Stelzl, E., Dietrich, P., Pohle, M., Werban, U., (2013): Linking geophysics and soil function modeling—An application study for biomass production. *Vadose Zone Journal* 12(4), doi:10.2136/vzj2013.01.0015.

Landwirtschaftskammer, N., (2019). Hans Jürgen Hölzmann. Modellrechnung für möglichen mehrwert einer beregnung. landwirtschaftskammer Nordrhein-Westfalen.

Lavoué, F., Van Der Kruk, J., Rings, J., André, F., Moghadas, D., Huisman, J. A., Lambot, S., Weihermüller, L., Vanderborght, J., Vereecken, H., (2010): Electromagnetic induction calibration using apparent electrical conductivity modelling based on electrical resistivity tomography. *Near Surface Geophysics* 8(6), 553-561, doi:10.3997/1873-0604.2010037.

Linker, R., Sylaios, G., (2016): Efficient model-based sub-optimal irrigation scheduling using imperfect weather forecasts. *Computers and Electronics in Agriculture* 130, 118-127, doi:/10.1016/j.compag.2016.10.004.

Linker, R., Sylaios, G., Tsakmakis, I., Ramos, T., Simionesei, L., Plauborg, F., Battilani, A., (2018): Sub-optimal model-based deficit irrigation scheduling with realistic weather forecasts. *Irrigation Science* 36(6), 349-362, doi:10.1007/s00271-018-0592-x.

Liu, J., Williams, J. R., Zehnder, A. J. B., Yang, H., (2007): GEPIC–modelling wheat yield and crop water productivity with high resolution on a global scale. *Agricultural systems* 94(2), 478-493.

Liu, X., Ren, Y., Gao, C., Yan, Z., Li, Q., (2017): Compensation effect of winter wheat grain yield reduction under straw mulching in wide-precision planting in the North China Plain. *Scientific Reports* 7(1), 213, doi:10.1038/s41598-017-00391-6.

Lozán, J. L., Brabi, H., Hupfer, P., Menzel, L., Schonwiese, C. D., (2007). Global change: enough water for all?

Lück, E., Gebbers, R., Ruehlmann, J., Spangenberg, U., (2009): Electrical conductivity mapping for precision farming. *Near Surf. Geophys* 7(1), 15-25.

Lun, F., Liu, J., Ciais, P., Nesme, T., Chang, J., Wang, R., Goll, D., Sardans, J., Peñuelas, J., Obersteiner, M., (2018): Global and regional phosphorus budgets in agricultural systems and their implications for phosphorus-use efficiency. *Earth System Science Data* 10(1), 1-18, doi:10.5194/essd-10-1-2018.

Machado, F. C., Montanari, R., Shiratsuchi, L. S., Lovera, L. H., Lima, E. d. S., (2015): Spatial dependence of electrical conductivity and chemical properties of the soil by electromagnetic induction. *Revista Brasileira de Ciência do Solo* 39(4), 1112-1120, doi:10.1590/01000683rbcs20140794.

McCown, R. L., Hammer, G. L., Hargreaves, J. N. G., Holzworth, D. P., Freebairn, D. M., (1996): APSIM: a novel software system for model development, model testing and simulation in agricultural systems research. *Agricultural systems* 50(3), 255-271.

McNeill, J. D., (1980). Electromagnetic terrain conductivity measurement at low induction numbers. Geonics Limited Ontario, Canada.

Mertens, F. M., Pätzold, S., Welp, G., (2008): Spatial heterogeneity of soil properties and its mapping with apparent electrical conductivity. *Journal of Plant Nutrition and Soil Science* 171(2), 146-154, doi:10.1002/jpln.200625130.

Mester, A., van der Kruk, J., Zimmermann, E., Vereecken, H., (2011): Quantitative two-layer conductivity inversion of multi-configuration electromagnetic induction measurements. *Vadose Zone Journal* 10(4), 1319-1330, doi:10.2136/vzj2011.0035.

Mester, A., Zimmermann, E., Van der Kruk, J., Vereecken, H., Van Waasen, S., (2014): Development and drift-analysis of a modular electromagnetic induction system for shallow ground conductivity measurements. *Measurement science and technology* 25(5), 055801, doi::10.1088/0957-0233/25/5/055801.

Minsley, B. J., Smith, B. D., Hammack, R., Sams, J. I., Veloski, G., (2012): Calibration and filtering strategies for frequency domain electromagnetic data. *Journal of Applied Geophysics* 80, 56-66, doi:10.1016/j.jappgeo.2012.01.008.

Monteiro Santos, F. A., Triantafilis, J., Bruzgulis, K. E., Roe, J. A. E., (2010): Inversion of multiconfiguration electromagnetic (DUALEM-421) profiling data using a one-dimensional laterally constrained algorithm. *Vadose Zone Journal*, doi:10.2136/vzj2009.0088.

Montzka, C., Jagdhuber, T., Horn, R., Bogena, H. R., Hajnsek, I., Reigber, A., Vereecken, H., (2016): Investigation of SMAP fusion algorithms with airborne active and passive L-band microwave remote sensing. *IEEE Transactions on Geoscience and Remote Sensing* 54(7), 3878-3889, doi:10.1109/TGRS.2016.2529659.

Nawar, S., Corstanje, R., Halcro, G., Mulla, D., Mouazen, A. M., (2017). Delineation of Soil Management Zones for Variable-Rate Fertilization: A Review, Advances in Agronomy. Elsevier, pp. 175-245.

NRW, (1960). Soil Taxation Map. 1960.Bödenschätrzungskarte: Bearbeitet nach den amtlichen Unterlagen der Bodenschätzung und des Geologichen Landesamts Nordrhein-Westfalen vom Regierungspräsident in Aachen und dem Geologischen Ladesamt Nordrhein-Westfalen 1960. Landesvermessungsamt Nordrhein-Westfalen.

NRW, (2017). Bezirksregierung Köln - The WebAtlasDE is an Internet computer service developed jointly by the federal (North Rhine-Westfphalia) and state governments and provided by the Federal Agency for Cartography and Geodesy.

NRW, (2018). Geologischer Dients NRW.

Oldoni, H., Bassoi, L. H., (2016): Delineation of irrigation management zones in a Quartzipsamment of the Brazilian semiarid region. *Pesquisa Agropecuária Brasileira* 51(9), 1283-1294, doi:10.1590/S0100-204X2016000900028.

Patzold, S., Mertens, F. M., Bornemann, L., Koleczek, B., Franke, J., Feilhauer, H., Welp, G., (2008): Soil heterogeneity at the field scale: a challenge for precision crop protection. *Precision Agriculture* 9(6), 367-390, doi:10.1007/s11119-008-9077-x.

Paz, J. O., (2000): Analysis of spatial yield variability and economics of prescriptions for precision agriculture: a crop modeling approach.

Paz, J. O., Batchelor, W. D., Colvin, T. S., Logsdon, S. D., Kaspar, T. C., Karlen, D. L., (1998): Analysis of water stress effects causing spatial yield variability in soybeans. *Transactions of the ASAE* 41(5), 1527.

Paz, J. O., Batchelor, W. D., Colvin, T. S., Logsdon, S. D., Kaspar, T. C., Karlen, D. L., Babcock, B. A., Pautsch, G. R., (1999): Model-based technique to determine variable rate nitrogen for corn. *Precision Agriculture* (precisionagric4b), 1279-1289.

Penning de Vries, J., teb Berge, Bakema, (1989). Simulation of ecophysiological processes of growth in several annual crops, 29. Int. Rice Res. Inst.

Post, H., Hendricks Franssen, H.-J., Han, X., Baatz, R., Montzka, C., Schmidt, M., Vereecken, H., (2018): Evaluation and uncertainty analysis of regional-scale CLM4. 5 net carbon flux estimates. *Biogeosciences* 15(1), 187-208, doi:10.5194/bg-15-187-2018.

Prasad, P. V. V., Staggenborg, S. A., Ristic, Z., (2008): Impacts of drought and/or heat stress on physiological, developmental, growth, and yield processes of crop plants. *Response of crops to limited water: Understanding and modeling water stress effects on plant growth processes* (responseofcrops), 301-355.

Quesada, B., Arneth, A., Robertson, E., de Noblet-Ducoudré, N., (2018): Potential strong contribution of future anthropogenic land-use and land-cover change to the terrestrial carbon cycle. *Environmental Research Letters* 13(6), 064023, doi:10.1088/1748-9326/aac4c3.

Rawls, W. J., Brakensiek, D. L., (1985). Prediction of soil water properties for hydrologic modeling, Watershed management in the eighties. ASCE, pp. 293-299.

Reichenau, T. G., Korres, W., Montzka, C., Fiener, P., Wilken, F., Stadler, A., Waldhoff, G., Schneider, K., (2016): Spatial heterogeneity of leaf area index (LAI) and its temporal course on arable land: combining field measurements, remote sensing and simulation in a

comprehensive data analysis approach (CDAA). *PloS one* 11(7), e0158451, doi:10.1371/journal.pone.0158451.

Richards, J. A., (1999). Remote sensing digital image analysis, 3. Springer.

Ritchie, J. T., (1985): Description and performance of CERES wheat: A user-oriented wheat yield model. *ARS wheat yield project*, 159-175.

Robert, P., (1993): Characterization of soil conditions at the field level for soil specific management. *Geoderma* 60(1-4), 57-72.

Robinet, J., von Hebel, C., Govers, G., van der Kruk, J., Minella, J. P. G., Schlesner, A., Ameijeiras-Mariño, Y., Vanderborght, J., (2018): Spatial variability of soil water content and soil electrical conductivity across scales derived from Electromagnetic Induction and Time Domain Reflectometry. *Geoderma* 314, 160-174, doi:10.1016/j.geoderma.2017.10.045.

Robinson, D. A., Abdu, H., Lebron, I., Jones, S. B., (2012): Imaging of hill-slope soil moisture wetting patterns in a semi-arid oak savanna catchment using time-lapse electromagnetic induction. *Journal of Hydrology* 416, 39-49, doi:10.1016/j.jhydrol.2011.11.034.

Robinson, D. A., Binley, A., Crook, N., Day-Lewis, F., Ferré, T. P. A., Grauch, V. J. S., Knight, R., Knoll, M., Lakshmi, V., Miller, R., (2008): Advancing process-based watershed hydrological research using near-surface geophysics: A vision for, and review of, electrical and magnetic geophysical methods. *Hydrological Processes* 22(18), 3604-3635, doi:10.1002/hyp.6963.

Röhrig, W., (1996): Bodenkarte 1:5000 zur landwirtschaftlichen Standorterkundung (BK5ÖL). *Geologischen Landesamt Nordrhein-Westfalien*.

Rosegrant, M. W., Ringler, C., Zhu, T., (2009): Water for agriculture: maintaining food security under growing scarcity. *Annual review of Environment and resources* 34, 205-222, doi:Water for agriculture: maintaining food security under growing scarcity.

Rosgen, D. L., (1994): A classification of natural rivers. *Catena* 22(3), 169-199.

Rubin, Y., Hubbard, S., (2005): Hydrogeophysics. *Springer, Netherlands* 50, 523.

Rudolph, S., Marchant, B. P., Weihermüller, L., Vereecken, H., (2018): Assessment of the position accuracy of a single-frequency GPS receiver designed for electromagnetic induction surveys. *Precision Agriculture*, 1-21, doi:10.1007/s11119-018-9578-1.

Rudolph, S., van der Kruk, J., Von Hebel, C., Ali, M., Herbst, M., Montzka, C., Pätzold, S., Robinson, D. A., Vereecken, H., Weihermüller, L., (2015): Linking satellite derived LAI patterns with subsoil heterogeneity using large-scale ground-based electromagnetic induction measurements. *Geoderma* 241, 262-271, doi:10.1016/j.geoderma.2014.11.015.

Rum, G., IAMSCHULA, D. E. B., PAUL, H. K., (1974): Prevalence and interrelationships of root. *Community dentistry and oral epidemiology* 2, 295-304.

Saey, T., Simpson, D., Vermeersch, H., Cockx, L., Van Meirvenne, M., (2009): Comparing the EM38DD and DUALEM-21S sensors for depth-to-clay mapping. *Soil Science Society of America Journal* 73(1), 7-12, doi:10.1016/j.geoderma.2009.02.024.

Sánchez, P. A., (2010): Tripling crop yields in tropical Africa. *Nature Geoscience* 3(5), 299.

Schmidt, M., Reichenau, T. G., Fiener, P., Schneider, K., (2012): The carbon budget of a winter wheat field: An eddy covariance analysis of seasonal and inter-annual variability. *Agricultural and Forest Meteorology* 165, 114-126, doi:10.1016/j.agrformet.2012.05.012.

Scilands-GmBH, (2013). Digital Elevation Model 1m mosaic data (Section 4), based on data from Bezirksregierung Köln, Göttingen, Rermany. CRC/TR32 Database (TR32DB). Accessed from http://www.tr32db.uni-koeln.de/data.php?dataID=440 at 2017-07-11.

Shanahan, P. W., Binley, A., Whalley, W. R., Watts, C. W., (2015): The use of electromagnetic induction to monitor changes in soil moisture profiles beneath different wheat genotypes. *Soil Science Society of America Journal* 79(2), 459-466, doi:10.2136/sssaj2014.09.0360.

Sheets, K. R., Hendrickx, J. M. H., (1995): Noninvasive soil water content measurement using electromagnetic induction. *Water Resources Research* 31(10), 2401-2409.

Shelia, V., Šimůnek, J., Boote, K., Hoogenbooom, G., (2018): Coupling DSSAT and HYDRUS-1D for simulations of soil water dynamics in the soil-plant-atmosphere system. *Journal of Hydrology and Hydromechanics* 66(2), 232-245, doi:10.1515/johh-2017-0055

Simmer, C., Thiele-Eich, I., Masbou, M., Amelung, W., Bogena, H., Crewell, S., Diekkrüger, B., Ewert, F., Hendricks Franssen, H.-J., Huisman, J. A., (2015): Monitoring and modeling the terrestrial system from pores to catchments: the transregional collaborative research center on

patterns in the soil–vegetation–atmosphere system. *Bulletin of the American Meteorological Society* 96(10), 1765-1787, doi:10.1175/BAMS-D-13-00134.1.

Šimůnek, J., Suarez, D. L., (1993): Modeling of carbon dioxide transport and production in soil: 1. Model development. *Water Resources Research* 29(2), 487-497.

Šimůnek, J., Suarez, D. L., Šejna, M., (1996): The UNSATCHEM software package for simulating one-dimensional variably saturated water flow, heat transport, carbon dioxide production and transport, and multicomponent solute transport with major ion equilibrium and kinetic chemistry. *Res. Rep* 141, 186.

Slingo, J. M., Challinor, A. J., Hoskins, B. J., Wheeler, T. R., (2005): Introduction: food crops in a changing climate. *Philosophical Transactions of the Royal Society B: Biological Sciences* 360(1463), 1983-1989, doi:10.1098/rstb.2005.1755.

Spitters, C., van Keulen, H., van Kraalingen, D., (1989): Simulation and systems management in crop production. A simple and univesral cro growth simulator: SUCROS87.

Spitters, C. J. T., Schapendonk, A. H. C. M., (1990). Evaluation of breeding strategies for drought tolerance in potato by means of crop growth simulation, Genetic aspects of plant mineral nutrition. Springer, pp. 151-161.

Sponagel, H., Grottenthaler, K. J., Hartmann, R., Hartwich, P., Janetzko, P., Joisten, H., Kühn, D., Sabel, K. J., Tradl, R., (2005). Bodenkundliche Kartieranleitung (German Manual of Soil Mapping, KA5) (fifth ed.), Bundesanstalt für Geowissenschaften und Rohstoffe, Hannover (2005). Schweizerbart.

Stadler, A., Rudolph, S., Kupisch, M., Langensiepen, M., van der Kruk, J., Ewert, F., (2015): Quantifying the effects of soil variability on crop growth using apparent soil electrical conductivity measurements. *European journal of agronomy* 64, 8-20, doi:/10.1016/j.eja.2014.12.004.

Steduto, P., Hsiao, T. C., Fereres, E., Raes, D., (2012): FAO Irrigation and drainage paper 66. *Crop yield response to water, Food and Agriculture Organization of the United Nations*.

Steduto, P., Hsiao, T. C., Raes, D., Fereres, E., (2009): AquaCrop—The FAO crop model to simulate yield response to water: I. Concepts and underlying principles. *Agronomy Journal* 101(3), 426-437, doi:10.2134/agronj2008.0139s.

Stockle, C. O., Martin, S. A., Campbell, G. S., (1994): CropSyst, a cropping systems simulation model: water/nitrogen budgets and crop yield. *Agricultural Systems* 46(3), 335-359.

Stockmann, U., Huang, J., Minasny, B., Triantafilis, J., (2017): Utilizing a DUALEM-421 and inversion modelling to map baseline soil salinity along toposequences in the Hunter Valley Wine district. *Soil Use and Management* 33(3), 413-424, doi:10.1111/sum.12352.

Sudduth, K. A., Drummond, S. T., Kitchen, N. R., (2001): Accuracy issues in electromagnetic induction sensing of soil electrical conductivity for precision agriculture. *Computers and electronics in agriculture* 31(3), 239-264.

Tan, X., Mester, A., von Hebel, C., Zimmermann, E., Vereecken, H., van Waasen, S., van der Kruk, J., (2019): Simultaneous calibration and inversion algorithm for multiconfiguration electromagnetic induction data acquired at multiple elevationsCalibration inversion for rigid-boom EMI. *Geophysics* 84(1), EN1-EN14, doi:10.1190/geo2018-0264.1.

Taylor, J. A., Short, M., McBratney, A. B., Wilson, J., (2010). Comparing the ability of multiple soil sensors to predict soil properties in a Scottish potato production system, Proximal soil sensing. Springer, pp. 387-396.

Taylor, J. C., Wood, G. A., Earl, R., Godwin, R. J., (2003): Soil factors and their influence on within-field crop variability, part II: spatial analysis and determination of management zones. *Biosystems engineering* 84(4), 441-453, doi:10.1016/S1537-5110(03)00005-9.

Thiesson, J., Kessouri, P., Schamper, C., Tabbagh, A., (2014): Calibration of frequency-domain electromagnetic devices used in near-surface surveying. *Near Surface Geophysics* 12(4), 481-491, doi:10.3997/1873-0604.2014012.

Topak, R., Süheri, S., Acar, B., (2011): Effect of different drip irrigation regimes on sugar beet (Beta vulgaris L.) yield, quality and water use efficiency in Middle Anatolian, Turkey. *Irrigation Science* 29(1), 79-89, doi:10.1007/s00271-010-0219-3.

Topp, G. C., Davis, J. L., Annan, A. P., (1980): Electromagnetic determination of soil water content: Measurements in coaxial transmission lines. *Water Resources Research* 16(3), 574-582.

Unger, P. W., Jones, O. R., (1998): Long-term tillage and cropping systems affect bulk density and penetration resistance of soil cropped to dryland wheat and grain sorghum. *Soil and Tillage Research* 45(1-2), 39-57.

USAAF, (1944). Picture ID: 2016, Mission ID: 33-0778. Luftbilddatenbank, Dr Carls GMBH.

USDA, (2019). USDA Soil Texture Calculator.

van Dam, R. L., (2012): Landform characterization using geophysics—Recent advances, applications, and emerging tools. *Geomorphology* 137(1), 57-73, doi:10.1016/j.geomorph.2010.09.005.

Van Diepen, C. A., Wolf, J., Van Keulen, H., Rappoldt, C., (1989): WOFOST: a simulation model of crop production. *Soil Use and Management* 5(1), 16-24.

Van Genuchten, M. T., (1980): A closed-form equation for predicting the hydraulic conductivity of unsaturated soils. *Soil Science Society of America journal* 44(5), 892-898.

Van Heemst, H. D. J., (1988). Plant data values required for simple crop growth simulation models: review and bibliography. CABO [etc.].

van Ittersum, M. K., Cassman, K. G., Grassini, P., Wolf, J., Tittonell, P., Hochman, Z., (2013): Yield gap analysis with local to global relevance—a review. *Field Crops Research* 143, 4-17, doi:10.1016/j.fcr.2012.09.009.

van Ittersum, M. K., Leffelaar, P. A., Van Keulen, H., Kropff, M. J., Bastiaans, L., Goudriaan, J., (2003): On approaches and applications of the Wageningen crop models. *European journal of agronomy* 18(3-4), 201-234.

van Keulen, H., (1975). Simulation of water use and herbage growth in arid regions. Pudoc.

Van Looy, K., Bouma, J., Herbst, M., Koestel, J., Minasny, B., Mishra, U., Montzka, C., Nemes, A., Pachepsky, Y. A., Padarian, J., (2017): Pedotransfer functions in Earth system science: challenges and perspectives. *Reviews of Geophysics* 55(4), 1199-1256, doi:10.1002/2017RG000581.

van Schilfgaarde, J., (1999): Is precision agriculture sustainable? *American Journal of Alternative Agriculture* 14(1), 43-46.

Vanclooster, M., (1995): WAVE, a mathematical model for simulating water and agrochemicals in the soil and the vadose environment. *Reference and user's manual, release 2.0*.

Vandenberghe, J., van Overmeeren, R. A., (1999): Ground penetrating radar images of selected fluvial deposits in the Netherlands. *Sedimentary Geology* 128(3), 245-270, doi:10.1016/S0037-0738(99)00072-X.

Vereecken, H., Schnepf, A., Hopmans, J. W., Javaux, M., Or, D., Roose, T., Vanderborght, J., Young, M., Amelung, W., Aitkenhead, M., (2016): Modeling soil processes: Review, key challenges, and new perspectives. *Vadose Zone Journal* 15(5), doi:10.2136/vzj2015.09.0131.

Vitharana, U. W., Van Meirvenne, M., Simpson, D., Cockx, L., De Baerdemaeker, J., (2008): Key soil and topographic properties to delineate potential management classes for precision agriculture in the European loess area. *Geoderma* 143(1-2), 206-215, doi:10.1016/j.geoderma.2007.11.003.

von Hebel, C., Matveeva, M., Verweij, E., Rademske, P., Kaufmann, M. S., Brogi, C., Vereecken, H., Rascher, U., van der Kruk, J., (2018): Understanding soil and plant interaction by combining ground-based quantitative electromagnetic induction and airborne hyperspectral data. *Geophysical Research Letters* 45(15), 7571-7579, doi:10.1029/2018GL078658.

von Hebel, C., Rudolph, S., Mester, A., Huisman, J. A., Kumbhar, P., Vereecken, H., van der Kruk, J., (2014): Three-dimensional imaging of subsurface structural patterns using quantitative large-scale multiconfiguration electromagnetic induction data. *Water Resources Research* 50(3), 2732-2748, doi:10.1002/2013WR014864.

Vos, C., Don, A., Prietz, R., Heidkamp, A., Freibauer, A., (2016): Field-based soil-texture estimates could replace laboratory analysis. *Geoderma* 267, 215-219, doi:10.1016/j.geoderma.2015.12.022.

Vries, P. d., (1989). Simulation of ecophysiological processes of growth in several annual crops, 29. Int. Rice Res. Inst.

Walter, R., (2010). Aachen und nördliche Umgebung: Mechernicher Voreifel, Aachen-Südlimburger Hügelland und westliche Niederrheinische Bucht.

Ward, S. H., Hohmann, G. W., (1988): Electromagnetic theory for geophysical applications. *Electromagnetic methods in applied geophysics* 1(3), 131-311.

West, T. O., Marland, G., King, A. W., Post, W. M., Jain, A. K., Andrasko, K., (2004): Carbon management response curves: estimates of temporal soil carbon dynamics. *Environmental Management* 33(4), 507-518, doi:10.1007/s00267-003-9108-3.

Wong, M. T. F., Asseng, S., (2006): Determining the causes of spatial and temporal variability of wheat yields at sub-field scale using a new method of upscaling a crop model. *Plant and Soil* 283(1-2), 203-215, doi: 10.1007/s11104-006-0012-5.

WRB, I. W. G., (2015). World Reference Base for Soil Resources 2014, update 2015. International soil classification system for naming soils and creating legends for soil maps. World Soil Resources Reports No. 106. FAO, Rome.

Xiao, J., Moody, A., (2005): A comparison of methods for estimating fractional green vegetation cover within a desert-to-upland transition zone in central New Mexico, USA. *Remote sensing of environment* 98(2-3), 237-250, doi:10.1016/j.rse.2005.07.011.

Yao, R., Yang, J., Wu, D., Xie, W., Gao, P., Jin, W., (2016): Digital mapping of soil salinity and crop yield across a coastal agricultural landscape using repeated electromagnetic induction (EMI) surveys. *PloS one* 11(5), e0153377, doi:10.1371/journal.pone.0153377.

Zare, E., Huang, J., Triantafilis, J., (2016): Identifying soil landscape units at the district scale by numerically clustering remote and proximal sensed data. *Computers and Electronics in Agriculture* 127, 510-520, doi:10.1016/j.compag.2016.07.001.

Zeng, X., Rao, P., DeFries, R. S., Hansen, M. C., (2003): Interannual variability and decadal trend of global fractional vegetation cover from 1982 to 2000. *Journal of Applied Meteorology* 42(10), 1525-1530.

Zhang, Y., Schaap, M. G., (2017): Weighted recalibration of the Rosetta pedotransfer model with improved estimates of hydraulic parameter distributions and summary statistics (Rosetta3). *Journal of Hydrology* 547, 39-53, doi:10.1016/j.jhydrol.2017.01.004.

Žydelis, R., Weihermüller, L., Herbst, M., Klosterhalfen, A., Lazauskas, S., (2018): A model study on the effect of water and cold stress on maize development under nemoral climate. *Agricultural and Forest Meteorology* 263, 169-179, doi:10.1016/j.agrformet.2018.08.011.

Supplementary material

This first supplementary material section shows the results of the statistical comparison between typical profiles of different soil units as well as the horizon description, depth, texture, and water content for each soil unit described in Chapter 3. The second section provides additional information regarding the parameterization of sugar beet, corn and winter wheat described in Chapter 4.

S1. Statistical comparison between soil profiles

S1.1 Sub-area A

The characteristics of the averaged profiles of the four classes of sub-area A are shown in Table S1. The results of the t-test conducted between matching horizons of the classes of sub-area A are shown in Table S2. The t-tests were conducted between the available values of paired classes: A1a vs A1b, A1b vs A1c, A1c vs A1d. The t-test was considered positive when the computed value fell in the 5 % level of significance (2.5 % in each tail).

Table S1. Texture of the averaged profiles of the four classes of sub-area A with maximum depth of the horizon, gravimetric water content, clay content, silt content, sand content, and gravel content (gravel content given in % of weight and relative to the total weight of the dry sample).

Class	Horizon	Depth (cm)	WC (%)	Clay (%)	Silt (%)	Sand (%)	Gravels (%)
A1a	**Ap-AB**	40.7	17.8	17.1	63.0	19.8	10.8
	Bw	86.0	14.8	21.3	58.0	20.6	14.0
	2C	ND	10.8	25.6	45.7	28.6	33.3
A1b	**Ap-AB**	39.9	16.2	13.0	66.6	20.4	16.7
	Bw	66.6	12,7	18.2	58.0	23.9	27.6
	2C	ND	8.2	19.2	29.9	50.9	24.6
A1c	**Ap-Ah**	37.6	18.7	14.4	67.0	18.8	29.8
	Bw	58.1	15.3	16.8	62.7	20.5	29.1
	2C	ND	10.0	21.9	37.0	41.1	43.7
A1d	**Ap-AB**	41.0	17.2	12.9	66.0	21.1	18.6
	Bw	49.6	14.4	17.3	69.7	13.0	18.2
	2C	ND	10.8	14.5	54.0	31.4	36.0

Table S2 - Results of the pairwise t-tests conducted in sub-area A. Bold font indicates significant differences.

Horizon	Classes	Depth	WC	Clay	Sand	Gravels
Ap-AB	**A1a vs A1b**	0.757	0.280	**0.003**	0.862	0.073
	A1b vs A1c	0.377	0.085	0.068	0.440	**0.031**
	A1c vs A1d	0.232	0.232	**0.034**	0.529	0.092
Bw	**A1a vs A1b**	**0.040**	**0.001**	0.127	0.406	**0.017**
	A1b vs A1c	0.197	0.071	0.303	0.431	0.868
	A1c vs A1d	0.558	ND	ND	ND	ND
2C	**A1a vs A1b**	ND	0.191	0.308	0.109	0.461
	A1b vs A1c	ND	0.440	0.284	0.415	0.170
	A1c vs A1d	ND	0.785	0.076	0.399	0.666

S1.2 Sub-area B

The characteristics of the averaged profiles of the four classes of sub-area B are shown in Table S3.

Table S3 - Texture of the averaged profiles of the four classes of sub-area B with maximum depth of the horizon, gravimetric water content, clay content, silt content, sand content, and gravel content (gravel content given in % of weight and relative to the total weight of the dry sample).

Class	Horizon	Depth (cm)	WC (%)	Clay (%)	Silt (%)	Sand (%)	Gravels (%)
B1a	**Ap-AB**	46.0	18.6	15.9	69.0	15.1	5.3
	Bw	126.3	15.1	17.3	65.3	17.3	3.1
	Bg	ND	16.9	22.5	64.6	12.8	12.8
B1b	**Ap-AB**	47.0	18.5	12.3	68.5	19.2	9.5
	Bw	121.3	14.2	16.4	66.4	17.3	6.9
	Bg	146.3	15.6	18.1	64.1	17.8	1.6
	2C	ND	13.4	15.7	62.4	21.9	ND
B2a	**Ap-AB**	38.0	18.5	15.1	65.2	19.7	9.7
	M	90.0	16.9	14.6	65.2	20.2	4.6
	Bw	119.7	15.5	22.6	58.6	18.9	3.7
	Bg	ND	16.5	20.1	64.6	15.2	0.8
B2b	**Ap-AB**	42.7	19.3	12.0	70.9	17.1	3.5
	M	68.7	15.5	15.1	69.3	15.7	6.5
	Bw	157.7	15.7	18.8	65.4	15.9	2.5
	Bg	ND	16.4	21.3	67.3	11.4	0.6
B2c	**Ap-AB**	45.3	16.3	14.9	63.4	21.7	24.3
	M	76.0	15.7	17.1	64.4	18.5	16.7
	Bw	ND	15.6	20.7	63.2	16.1	9.1

The results of the t-test conducted between matching horizons of classes of sub-area B are shown in Table S4 and Table S5. The t-tests were conducted between the available values of paired classes: B1a vs B1b (natural deposits shown in Table S4), and B2a vs B2b - B2b vs B2c (anthropogenic deposits shown in Table S5). The t-test was considered positive when the computed value fell in the 5 % level of significance (2.5 % in each tail).

Table S4 - Results of the pairwise t-tests conducted in sub-area B (natural deposits). Bold font indicates significant differences.

Horizon	Classes	Depth	WC	Clay	Sand	Gravels
Ap-AB	**B1a vs B1b**	0.852	0.925	**0.005**	**0.002**	0.402
Bw	**B1a vs B1b**	0.930	0.394	**0.006**	0.700	0.323
Bg	**B1a vs B1b**	ND	0.123	**0.002**	**0.012**	**0.014**

Table S5 - Results of the pairwise t-tests in sub-area B (anthropogenic deposits). Bold font indicates significant differences.

Horizon	Classes	Depth	WC	Clay	Sand	Gravels
Ap-AB	**B2a vs B2b**	0.268	0.612	**0.002**	0.065	0.149
	B2b vs B2c	0.386	**0.021**	**0.006**	**0.010**	**0.001**
M	**B2a vs B2b**	0.610	0.198	0.497	**0.020**	0.686
	B2b vs B2c	0.826	0.806	0.149	0.067	0.121
Bw	**B2a vs B2b**	0.231	0.700	0.166	0.075	0.456
	B2b vs B2c	ND	0.913	0.466	0.931	0.052
Bg	**B2a vs B2b**	ND	0.962	0.782	0.190	0.861

S1.3 Sub-area C

The characteristics of the averaged profiles of the four classes of sub-area C are shown in Table S6. The results of the t-test conducted between matching horizons of classes of sub-area C are shown in Table S7 and Table S8. The t-tests were conducted between the available values of paired classes: C1a vs C1b (natural deposits shown in Table S7), and C2a vs C2b (anthropogenic deposits shown in Table S8). The t-test was considered positive when the computed value fell in the 5 % level of significance (2.5 % in each tail).

Table S6 - Texture of the averaged profiles of the four classes of sub-area C with maximum depth of the horizon, gravimetric water content, clay content, silt content, sand content, and gravel content (gravel content given in % of weight and relative to the total weight of the dry sample).

Class	Horizon	Depth (cm)	WC (%)	Clay (%)	Silt (%)	Sand (%)	Gravels (%)
C1a	**Ap-AB**	45.0	18.9	17.4	69.0	13.6	0.4
	Bw	109.3	15.5	20.9	66.5	12.7	0.1
	Bg	ND	16.0	20.8	64.0	15.1	0.3
C1b	**Ap-AB**	42.0	18.5	16.4	69.8	13.8	0.6
	Bw	129.3	16.1	20.1	66.5	13.3	0.4
	Bg	ND	14.1	21.5	63.6	14.8	1.3
C2a	**Ap-AB**	41.0	18.4	16.3	71.2	12.4	0.0
	M	51.0	17.0	18.2	69.2	12.6	0.0
	Bw	86.0	17.6	18.4	70.3	11.4	0.2
	Bg	ND	15.9	19.5	59.5	20.9	5.1
C2b	**Ap-AB**	43.0	19.5	14.6	65.8	19.5	0.6
	M	112.5	16.3	17.1	65.8	17.0	1.1
	Bw	129.0	15.5	16.4	73.6	9.9	0.0
	Bg	ND	15.4	23.2	56.1	20.7	0.0

Table S7 - Results of the pairwise t-tests in sub-area C (natural deposits). Bold font indicates significant differences.

Horizon	Classes	Depth	WC	Clay	Sand	Gravels
Ap-AB	**C1a vs C1b**	0.429	0.522	0.113	0.675	0.669
Bw	**C1a vs C1b**	0.419	0.277	0.562	0.457	0.326
Bg	**C1a vs C1b**	ND	**0.021**	0.346	0.993	0.203

Table S8 - Results of the pairwise t-tests in sub-area C (anthropogenic deposits). Bold font indicates significant differences.

Horizon	Classes	Depth	WC	Clay	Sand	Gravels
Ap-AB	**C2a vs C2b**	0.294	0.425	0.238	0.119	0.214
M	**C2a vs C2b**	**0.036**	ND	ND	ND	ND
Bw	**C2a vs C2b**	**0.034**	0.412	0.420	0.271	0.423
Bg	**C2a vs C2b**	ND	0.767	0.097	0.053	0.294

S1.4 Sub-area D

The characteristics of the averaged profiles of the four classes of sub-area D are shown in Table S9. The results of the t-test conducted between matching horizons of classes of sub-area D are shown in Table S10. The t-tests were conducted between the available values of paired classes: D1a vs D1b, D1b vs D1c, and D1c vs D1d. The t-test was considered positive when the computed value fell in the 10 % level of significance (5 % in each tail).

Table S9 - Texture of the averaged profiles of the four classes of sub-area D with maximum depth of the horizon, gravimetric water content, clay content, silt content, sand content, and gravel content (gravel content given in % of weight and relative to the total weight of the dry sample).

Class	Horiz.	Depth (cm)	WC (%)	Clay (%)	Silt3 (%)	Sand (%)	Gravels (%)
D1a	**Ap-AB**	52.3	19.6	18.1	66.6	15.3	0.9
	Bw	79.0	17.6	22.8	62.7	14.5	0.7
	Bg	134.0	16.1	21.7	57.6	20.7	3.9
	2C	ND	9.2	11.8	30.5	57.7	50.3
D1b	**Ap-AB**	41.3	20.8	17.7	66.3	15.9	4.3
	Bw	69.5	17.8	22.6	59.6	17.8	3.5
	Bg	122.7	15.5	22.6	56.9	20.6	1.7
	2C	ND	11.6	16.5	36.8	46.8	26.2
D1c	**Ap-AB**	38.3	21.2	17.2	66.5	16.3	2.3
	Bw	60.7	15.3	19.1	60	20.9	1.4
	Bg	83.3	15.6	17.5	60.6	21.9	8.5
	2C	ND	8.9	16.0	40.1	43.9	37.7
D1d	**Ap-AB**	32.5	22.4	15.0	68.5	16.5	6
	Bw	41.7	15.6	16.9	64.7	18.4	37.8
	Bg	46.7	16.1	18.1	64.3	17.7	2.6
	2C	ND	10.2	15.6	41.3	43	51
D2	**Ap-AB**	41.0	26.3	23.7	61.4	14.9	2.6
	M	92.5	24.9	25.4	56.2	18.4	6.2
	Riv.Gr.	ND	16.1	16.4	35.8	47.8	41.1

Table S10 - Results of the pairwise t-tests in sub-area D. Bold font indicates significant differences.

Horizon	Classes	Depth	WC	Clay	Sand	Gravels
Ap-AB	**D1a vs D1b**	0.278	0.174	0.775	0.309	**0.044**
	D1b vs D1c	0.299	0.596	0.548	0.631	0.243
	D1c vs D1d	0.221	0.102	**0.030**	0.843	0.548
Bw	**D1a vs D1b**	0.553	0.727	0.915	**0.030**	0.150
	D1b vs D1c	0.621	0.286	**0.016**	0.466	0.275
	D1c vs D1d	0.320	0.907	0.513	0.623	0.343
Bg	**D1a vs D1b**	0.338	0.661	0.664	0.983	0.345
	D1b vs D1c	**0.034**	0.977	**0.004**	0.888	0.304
	D1c vs D1d	0.082	ND	ND	ND	ND
2C	**D1a vs D1b**	ND	ND	ND	ND	ND
	D1b vs D1c	ND	0.083	0.816	0.865	0.411
	D1c vs D1d	ND	0.498	0.960	0.994	0.421

S2. Additional information on the parameterization of corn, sugar beet, and winter wheat

In this section, additional information regarding the parameterization of sugar beet, corn and winter wheat is provided. In sugar beet, a strong reduction of LAI_{NDVI} in soil units A1a-d and in D1a-d was observed in August and September 2016 (Figure 21). At this stage, the AgroC simulations for LAI already reached their highest possible value which was similar in all soil units. Here, the water stress simulated in May was not able to influence simulated LAI since temperature is the main driver of LAI accumulation in the juvenile stage. At the same time, there was no possibility to reduce LAI in August and September by water stress because the simulated water stress does not feed back to the simulation of the death rate of leaves or senescence in the current AgroC model. However, the observed LAIs indicated the existence of this feedback mechanism. Therefore, it was decided to reproduce the LAI reduction in the late growing season by using three specific death rates of leaves (m^2 leaf m^{-2} soil °C day^{-1}). The adopted death rate of leaves was higher in soil units A1a-d, intermediate in D1a-d, and lowest in D1a-d (Table S11). This calibration influenced the simulated LAI in a way that it improved the simulation of the differences in observed LAI between sub-areas A, BC, and D. Since all other plant parameters and boundary conditions were identical in all simulations, the differences in simulated LAI within each sub-area are solely due to the magnitude and timing of simulated water stress.

Table S11: Values of death rates of leaves used in the three groups of sugar beet simulations as a function of the temperature sum.

	Death rate of leaves (m^2 m^{-1} °C day^{-1})		
Temperature sum (°C)	**A1a-d**	**BC**	**D1a-d**
0	0.000	0.000	0.000
300	0.000	0.000	0.000
600	0.006	0.005	0.005
900	0.011	0.006	0.008
1200	0.022	0.007	0.008
1500	0.036	0.017	0.015
2000	0.060	0.036	0.045
2500	0.005	0.005	0.005
3000	0.001	0.001	0.001

In corn, the abrupt decrease in LAI that occurred in soil units A1a-d in September is due to the start of the senescence stage. Since senescence stage can be affected by water stress (Baret

et al., 2007), we assumed that crops that are subject to stronger water stress showed earlier senescence. This assumption was corroborated by field observations. In the AgroC model, senescence of corn is generally started when a DVS value of 1.4 is reached. To implement variable senescence consistent with stress intensity, this DVS value was set to 1.38, 1.35, 1.33, and 1.30 for soil units A1a-d, respectively.

Table S12: Partitioning of mass allocated to the stem and the leaves in the three groups of winter wheat simulations as function of DVS.

	A1a-d		**BC**		**D1a-d and D2a**	
DVS	**leaf**	**stem**	**leaf**	**stem**	**leaf**	**Stem**
0.00	0.55	0.45	0.60	0.40	0.70	0.30
0.10	0.50	0.50	0.60	0.40	0.70	0.30
0.25	0.45	0.65	0.55	0.45	0.70	0.30
0.50	0.29	0.71	0.44	0.56	0.33	0.77
0.70	0.25	0.75	0.28	0.72	0.15	0.85
0.95	0.05	0.95	0.10	0.90	0.05	0.95
1.05	0.05	0.00	0.05	0.00	0.05	0.00
2.00	0.00	0.00	0.00	0.00	0.00	0.00

In winter wheat, the three groups of soil units A1a-d, BC, and D1a-d showed differences in LAI_{NDVI}, especially in April. In this case, the partitioning of mass allocated to the stem and to the leaves was calibrated and one specific partitioning was used for each group of soil units (see Table S12). Since one parameterization was used within each group of soil units, the variability in simulated LAI in each group is the results of different soil parameterizations which affect water stress.